Novel Electromagnetic Radiation in Left-Handed Materials

by

Jie Lu

Bachelor of Science, Department of Physics,
Tsinghua University, China, June 1998
Master of Science, Department of Physics,
Tsinghua University, China, June 2001

Submitted to the Department of Physics
in partial fulfillment of the requirements for the degree of

Doctor of Philosophy

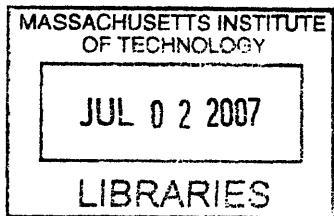at the

MASSACHUSETTS INSTITUTE OF TECHNOLOGY

September 2006

Author . . . .
Department of Physics
June 12, 2006

Certified by. . . . .
Jin Au Kong
Professor of Electrical Engineering
Thesis Supervisor

Certified by. . . . .
Min Chen
Professor of Physics
Thesis Supervisor

Accepted by . . . .
Thomas J. Greytak
Professor of Physics
Chairman, Department Committee on Graduate Students

Novel Electromagnetic Radiation in Left-Handed Materials

by

Jie Lu

Abstract

In this thesis, Čerenkov radiation of a moving charged particle inside a Left-Handed material (LHM) is studied through both theory and numerical simulations.

A LHM is a material whose permittivity and permeability have negative real parts. In the analysis of this thesis, the general theory of Čerenkov radiation was first studied for the unbounded regions filled with LHM. The physical meanings of different Green's functions are discussed, and finally the second kind of Hankel function is determined to represent the special properties of Čerenkov radiation: forward incoming phase and backward outgoing power, which satisfies both momentum and energy conservation. The effects of the dispersion and dissipation of both permittivity and permeability are also investigated. The results show that both forward and backward radiated waves can co-exist at different frequencies. When the dissipation is reduced, the directions of forward and backward radiation are close to 90° with respect to the particle's moving direction.

When the LHM is bounded, a waveguide can be formed. Depending upon the configuration and the relative dielectric constants of the surrounding normal material (we call them RHM in comparison with LHM), a surface wave can be formed. When a LHM is used as the filling material of a metallic waveguide, the radiation at some frequencies can be enhanced when a surface wave is excited. This enhancement can make the total radiated power in the waveguide larger than the radiation when the LHM is unbounded. Furthermore, using the same surface wave property, the decay of the radiation by a free space channel can be compensated when the channel is surrounded by a LHM.

The wave of Čerenkov radiation is a TM wave. In order to have a homogeneous response, the LHM structure should have at least two dimensional isotropic negative permittivity and one dimensional negative permeability. A new LHM design was proposed in this thesis. We have demonstrated that this design shows several advantages in comparison with present published designs through reflection and transmission simulations, and TM (TE) prism simulations. For the unit cell's dimension of 5mm, a LHM band is observed between 6GHz and 7GHz for TM wave incidence. We use an antenna array to model a traveling current source, which can represent a single

frequency component of a particle motion. The simulations show that our design can bend the radiation inside the structure. In order to observe the signal in the far field, we propose to use prism shaped LHM structures around the antenna array, by which, the difference between the angles of the forward radiation and backward radiation can be further amplified. These results can be a basis for a future experimental verification of backward radiation of the antenna arrays in a LHM.

Besides, two effects of the surface wave for the effective LHM slab are also investigated. The results show that the surface wave actually determines the focusing ability of a LHM slab. When the mismatch between the slab and the surrounding area becomes small, those evanescent waves, whose wave number is less than that of the surface wave, can be amplified by the slab, and contribute to the focusing at the image plane. This property can help us easily estimate the resolution of a LHM slab when it is used as a flat lens. A unique guided wave can also exist when a LHM slab is surrounded by two RHMs, where the two RHMs can be different or the same. This guided wave has a linear function for the transverse profile of the field inside the LHM slab, which can never exist in either a RHM or a plasma dielectric waveguide.

Thesis Supervisor: Jin Au Kong
Title: Professor of Electrical Engineering

Thesis Supervisor: Min Chen
Title: Professor of Physics

Acknowledgments

I would like to express my sincere thanks to my thesis advisor Prof. Jin Au Kong, who gave me the opportunity to join his group. Prof. Kong led me into the area of electromagnetic waves, especially this newly emerged exciting area of left-handed materials. I appreciate his consistent support on my research. Not only his enthusiasm of electromagnetics, but also his kindness and great characteristics will influence my whole life.

My sincere thanks also go to Prof. Min Chen, my co-advisor. His vision and consistent advices directed me to finish this thesis. Without Prof. Chen, my thesis could not be so consistent, and the topic may not be investigated in such a depth. His clarity and strictness of the physics concept impressed me from the beginning, and these benefit me to finish my thesis in a very rigorous way, and will influence my attitude to the work of my future career.

Special thanks to my thesis readers Prof. John D. Joannopoulos and Prof. Mildred S. Dresselhaus for their precious time on reviewing my thesis work and helpful suggestions.

I am grateful to the friendships and discussions from the CETA group members: Dr. Yan Zhang, Dr. Bae-Ian Wu, Dr. Joe Pacheco, Dr. Christopher D. Moss, Miss May Lai, Miss Zhen Wu. I would like to special thank Dr. Bae-Ian Wu for accompanying me on my research in my whole period in MIT. Dr. Wu has been giving me consistent help and advice on all my research projects, including all works in this thesis. Special thanks also go to Dr. Yan Zhang. Although I only worked with him for less than a year, his advice is always memorable and appreciated.

I want to thank my parents and my brother for everything they have done for me. To Chunrong Liu, my wife, and our daughter, Cynthia, thank you for your patience and love. Without your selfless support, I cannot finish this thesis. Finally, I would like to dedicate this thesis to my family.

Contents

List of Figures

17

List of Tables

Chapter 1

Introduction

In electromagnetic theory, materials are characterized by their constitutive matrices. Once we know these matrices, the behavior of the electromagnetic waves can be predicted by solving the Maxwell's equations with proper boundary conditions.

Among all constitutive matrices, permittivity and permeability are the two most important parameters, since most materials can be described by these two parameters. Previously, most phenomena were investigated in materials with both permittivity and permeability being positive for a normal material, or either one of them being negative, such as a plasma (when only the permittivity is negative), or a ferrite (when only the permeability is negative), until a paper was published in 1968 by Vesalago [1]. In this paper, Vesalago introduced a medium with a negative permittivity and a negative permeability simultaneously and summarized several electromagnetic wave phenomena. Because the wave vector, the electric field vector, and the magnetic field vector form a left-handed system, this medium was called left-handed medium (LHM). In contrast, we will call a normal medium with simultaneously positive permittivity and permeability as a right-handed medium (RHM). Vesalago also pointed out that there is no natural LHM, hence, there were not a lot of theoretical studies on LHMs until recently.

An experiment [2] in 2001 demonstrated that LHM can be realized by periodic structures composed of split-ring resonators and metallic rods, which was proposed by Pendry in [3] and [4]. From then on, most phenomena in [1] were thoroughly

investigated, whereas Čerenkov radiation in LHM is not yet fully explored.

Luo published a paper in 2003 [5] about the backward Čerenkov radiation in photonic crystals. But the mechanism is different which is actually due to the negative refraction in photonic crystals, and the effect is also combined with the transition radiation. The main difference between the photonic crystal and LHM is that in most cases, the effective dielectric constants and refractive index cannot be defined in photonic crystals, whereas for LHM they can. This thesis is devoted to investigate some basic properties of Čerenkov radiation in LHM due to the negative permittivity and permeability through both theory and numerical simulations. We are interested in whether there is any new physics phenomenon, and whether there is a material or structure can realize those properties and phenomenon. The content of the thesis is organized accordingly as follows.

First, the basic theory for Čerenkov radiation in unbounded LHM is investigated in Chapter 2 [6]. This is the most fundamental case through which we can find the exact solution for the electric and magnetic field inside the LHM when there is Čerenkov radiation. The proper Green's function is determined to correctly describe the radiation by a relativistic charged particle. The dispersion and dissipation of the LHM is then considered. Different Green's functions should be applied to different frequency bands at which the medium behaves as a LHM and as a RHM. The effect of the increasing loss of LHM is also discussed, and the radiation angle will be changed to close to the normal direction as the loss is reduced.

However, we know that there is no material can be really unbounded, especially LHM. Currently, LHMs are only manmade structures in GHz frequency range, and they are normally put into a waveguide for various experiments in order to reduce the noise and to ensure the behavior of LHM. Therefore we investigated Čerenkov radiation in bounded LHM (a waveguide) in Chapter 3, by which we hope to identify if there is any new physics phenomenon. Besides the obvious results that the radiated power will propagate backward in LHM instead of forward in RHM, we found that a surface plasmon can be excited at the boundary between RHM and LHM, even when the Čerenkov radiation condition is not satisfied in both media. This surface plasmon

22

enables LHM to have the one extra mechanism for the charged particles to radiate. The radiation of a charged particle passing a metallic waveguide filled with LHM is also studied. In this case, the condition at which a guided wave could be excited is investigated. Per an interest of potential application, we also discussed the possibility of using a LHM as an amplifying layer to compensate the decay of the radiation when an vacuum channel is present.

Two phenomena related to the surface plasmon between the boundary of a RHM and a LHM are discussed in Chapter 4. When the LHM slab is used as a flat lens, the surface wave indicated by the singularity of the transmission coefficient determines the resolution ability of the LHM slab [7]. Besides, a new type of guided wave is found to be supported by a LHM only, which serves as a transition mode between the surface plasmon modes and the propagating modes [8].

Finally, for the interests on what materials can be used to realize those phenomena, we introduce a new LH design in Chapter 5. This new design is specially for Čerenkov radiation. Various numerical simulations were performed to confirm the LH properties of the design. In order to test the response of the design to different frequency components of a charged particle motion, an antenna array is designed to model the traveling wave current. Then, the antenna is put in between the new LH structures, and the simulations were performed to investigate the radiation in the new LH structures.

Chapter 2

Čerenkov Radiation in an Unbounded Homogeneous LHM

2.1 Introduction

In his pioneering 1968 paper, Vesalago [1] mentioned, in addition to many other unique properties of LH media, the fact that Čerenkov radiation will be reversed, but no mathematical considerations were given. Normally, Čerenkov radiation occurs when a charged particle moves in a material with a speed faster than that of light in that material. Čerenkov radiation in normal media was first experimentally obsevered by P. A. Čerenkov in 1934 [9], and later theoretically explained by I. M. Frank and I. G. Tamm [10].

While many researchers have referred to Vesalago's statement about the reversal of Čerenkov radiation, none have addressed the physical importance of this phenomenon in detail. It is the purpose of the first part of this chapter to derive the mathematical solution for Čerenkov radiation in LH media in order to demonstrate the existence of backward radiation.

The remainder of this chapter is organized as follows. In Section 2, we derive the solution for Čerenkov radiation in isotropic LH media. Section 3 considers the effects of dispersion, which are inherent to all LH media. Section 4 discusses the effect of the existence of loss.

2.2 Mathematical formulation of Čerenkov radiation inside isotropic LH media

2.2.1 Formulation of the problem

As stated above, Čerenkov radiation occurs when a charged particle travels through a material at a velocity higher than that of light in that material. The principle of Čerenkov radiation is depicted in Fig. 2-1[12]:
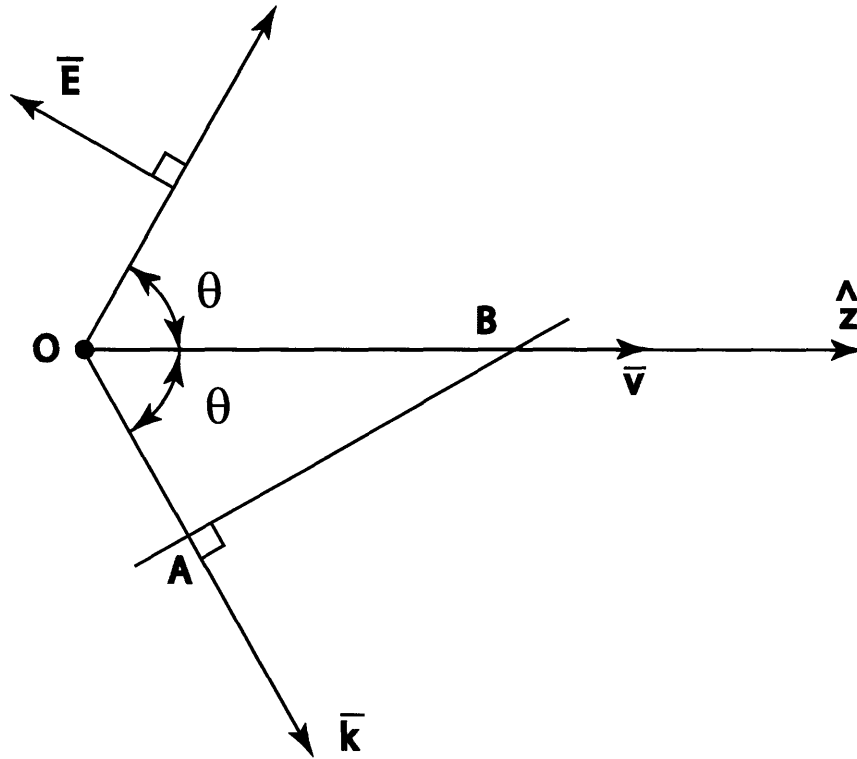
Figure 2-1: Čerenkov radiation in a normal material (RH media).

We consider a charged particle located at point O that is moving along $\hat{z}$ with a velocity $\bar{v}$. A coherent electromagnetic wave will be radiated when the condition in Eq. 2.1 is satisfied,

$$|\bar{v}| > \frac{c}{|n|} ,$$

(2.1)

where n is the refractive index of the medium, and $c \approx 3 \times 10^8 m/s$ is the speed of light in free space. This is well-known Čerenkov radiation. The line connecting points A to B forms the phase front of the radiation, which is propagating with the wave vector $\overline{k} = \hat{\rho}k_\rho + \hat{z}\frac{\omega}{v}$, where $\omega = 2\pi f$ is the angular frequency of the radiation, and k_ρ is the transverse component of the wave vector $\overline{k}$. The emitted radiation has an electric field vector polarized parallel to the plane determined by the direction of the particle speed and the direction of the radiation. Note that in real situations, many charged particles form a beam, so that the radiation has cylindrical symmetry and forms the well-known Čerenkov cone. The angle of the cone is given by θ (see Fig. 2-1) and is determined by

$$\cos\theta = \frac{1}{\beta n} \ , \tag{2.2}$$

where $\beta = \frac{v}{c} < 1$.

These characteristics have been well predicted in RH media by I. M. Frank and I. G. Tamm [10] by using classical electromagnetic theory. Following the formulation in [10], we shall rederive the mathematics for Čerenkov radiation in LH media.

2.2.2 Mathematical solution

The flow of charged particles can be described as a current of speed $\overline{v} = \hat{z}v$, written as

$$\overline{J}(\overline{r}, t) = \hat{z}qv\delta(z - vt)\delta(x)\delta(y) \ , \tag{2.3}$$

where q is the electric charge of the particle, and δ is the standard Dirac function. Under the Lorenz gauge condition, the wave equation for vector potential $\overline{A}$ is given as

$$\nabla^2\overline{A} + \frac{\omega^2}{c^2}n^2\overline{A} = -\mu\overline{J} \ . \tag{2.4}$$

In the frequency domain, and upon performing a cylindrical coordinate transfor-

27

mation, Eq. (2.4) can be reduced to a standard Poisson equation of the following form

$$\left[\frac{1}{\rho} \frac{\partial}{\partial \rho} \left(\rho \frac{\partial}{\partial \rho} \right) + k_\rho^2 \right] g(\rho) = -\frac{\delta(\rho)}{2\pi\rho} , \qquad (2.5)$$

where $k_\rho = \frac{\omega}{v} \sqrt{\beta^2 n^2 - 1}$, and $g(\rho)$ is the two dimensional scalar Green's function.

It can be seen that Eq. (2.5) has two independent solutions,

- case 1: $g(\rho) = \frac{i}{4} H_0^{(1)}(k_\rho \rho)$ which corresponds to an outgoing wave, for which $\overline{k} = k_\rho \hat{\rho} + k_z \hat{z}$,

- case 2: $g(\rho) = -\frac{i}{4} H_0^{(2)}(k_\rho \rho)$ which corresponds to an ingoing wave, for which $\overline{k} = -k_\rho \hat{\rho} + k_z \hat{z}$,

where $k_z = \frac{\omega}{v} > 0$.

Before choosing any solution, we calculate the electric and magnetic fields for both cases, from which the total energy radiated out in $\hat{\rho}$ and $\hat{z}$ directions in far field is obtained [11]:

- Case 1:

$$W_z = \int_{-\infty}^{\infty} S_z \, dt = \frac{q^2}{8\pi^2 \rho v} \int_0^\infty \frac{k_\rho}{\epsilon} \, d\omega \qquad (2.6a)$$

$$W_\rho = \int_{-\infty}^{\infty} S_\rho \, dt = \frac{q^2}{8\pi^2 \rho} \int_0^\infty \frac{k_\rho^2}{\omega \epsilon} \, d\omega \qquad (2.6b)$$

- Case 2:

$$W_z = \int_{-\infty}^{\infty} S_z \, dt = \frac{q^2}{8\pi^2 \rho v} \int_0^\infty \frac{k_\rho}{\epsilon} \, d\omega \qquad (2.7a)$$

$$W_\rho = \int_{-\infty}^{\infty} S_\rho \, dt = -\frac{q^2}{8\pi^2 \rho} \int_0^\infty \frac{k_\rho^2}{\omega \epsilon} \, d\omega \qquad (2.7b)$$

Even though the integration limits are from 0 to ∞, the above results are only valid for those frequencies that satisfy Eq. (2.1).

For the sake of illustration, we first consider a normal material, with $\epsilon > 0$ and $\mu > 0$. From Eqs. (2.6a) to (2.7b), we see that $W_z > 0$ for both cases, but $W_\rho > 0$ for case 1 and $W_\rho < 0$ for case 2. These two cases correspond to forward (same direction as the velocity of the particle) outgoing energy, and forward ingoing energy, respectively. From Sommerfeld's radiation condition, (no energy can come from infinity, since radiation must be emitted from a source), we choose that case 1 as the correct solution for Čerenkov radiation in normal materials with both ϵ and μ positive [13].

However, for LH media where $\epsilon < 0$ and $\mu < 0$, the results are reversed. From Eqs. (2.6a) and (2.6b), we isolate the following two cases:

- case 1: $W_z < 0$, $W_\rho < 0$ which corresponds to a backward and ingoing radiated energy.

- case 2: $W_z < 0$, $W_\rho > 0$ which corresponds to a backward and outgoing radiated energy.

The different cases are illustrated in Figs. 2-2 and 2-3, where the energy flow in LH media is shown for both cases.
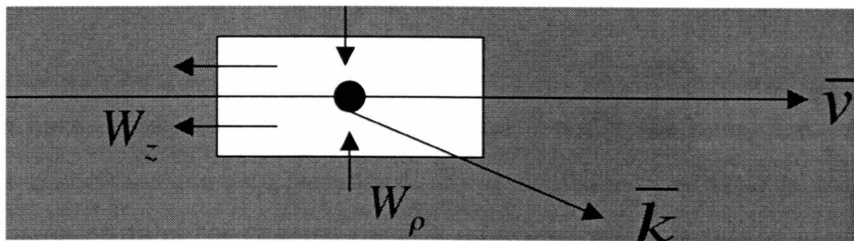
Figure 2-2: Directions of energy flow and wave vector for a charged particle moving in a LH medium for case 1 [$g(\rho) = \frac{i}{4} H_0^{(1)}(k_\rho \rho)$].

If we again suppose that there are no sources at infinity, the solution that needs to be chosen is the one corresponding to case 2. In addition, both the permittivity and
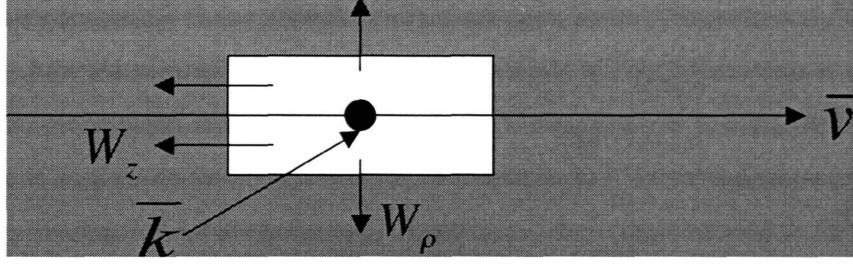
Figure 2-3: Directions of energy flow and wave vector for a charged particle moving in a LH medium for case 2 [$g(\rho) = -\frac{i}{4} H_0^{(2)}(k_\rho \rho)$].

the permeability need be negative to assure a real k that can support propagating waves. Finally, in the far field for isotropic lossless materials (so that the directions of the Poynting vector $\overline{S}$ is opposite to that of the wave vector $\overline{k}$), the angle between the direction of the Poynting vector and that of the velocity of the charged particle is again given by Eq. (2.2), but with the refractive index n being negative. We have therefore demonstrated that the energy is propagating backward as predicted in [1].

Yet, we still need to consider how the momentum is conserved, which relates to the definition of momentum in LH media. The standard definition of the momentum of an electromagnetic wave is $\overline{D} \times \overline{B} = \epsilon\mu\overline{S}$ [12]. Upon using this definition, we see that the momentum is

$$\overline{D} \times \overline{B} = \epsilon\mu\overline{E} \times \overline{H} = \epsilon\mu\overline{S} . \tag{2.8}$$

When both ϵ and μ are negative, $\overline{D} \times \overline{B}$ and $\overline{S}$ are in the same direction, which implies a momentum pointing backward. By momentum conservation, this implies that the momentum of the charged particle increases, which results in an energy increase. This is in contradiction with the third fundamental law of thermodynamics, which stipulates that charged particles radiate energy out and therefore lose energy.

The solution to this paradox is to be found in the quantum theory of Čerenkov radiation [13], in which the momentum of a photon is defined as $\overline{p} = \hbar\overline{k}$, where $\overline{p}$ is

30

the momentum, and $\hbar$ is the Planck constant divided by 2π. For case 2, $k_z > 0$ which implies a forward propagation, while the component in the $\hat{\rho}$ direction is cancelled. Therefore, momentum and energy are conserved. Inside a LH media, energy flow of the wave is in the opposite direction of its momentum. When the wave crosses the boundary from a LH medium into a RH medium, the component of wave vector k_z (thus also the momentum direction) will change sign (from $+\hat{z}$ to $-\hat{z}$ direction in our case), but the Poynting vector $\overline{E} \times \overline{H}$, which defines the energy flow, remains backward ($-\hat{z}$ direction). Therefore once inside the RH media, both energy flow and momentum of the wave will again be in the same (backward) direction.

2.3 Čerenkov radiation in dispersive LH media

It is already known from [1] that LH media must be frequency dispersive in order to satisfy positive energy constraints.

A common model to represent the permittivity $\epsilon(\omega)$ and permeability $\mu(\omega)$ has been given in [2], which we shall use here. For the sake of simplicity, we shall first consider a lossless case, for which the model becomes:

$$\mu_r = 1 - \frac{\omega_{mp}^2 - \omega_{mo}^2}{\omega^2 - \omega_{mo}^2} \ , \tag{2.9a}$$

$$\epsilon_r = 1 - \frac{\omega_{ep}^2 - \omega_{eo}^2}{\omega^2 - \omega_{eo}^2} \ , \tag{2.9b}$$

where ω_{mp} (ω_{ep}) is the magnetic (electric) plasma frequency of the model, and ω_{mo} ($omega_{eo}$) is the magnetic (electric) resonant frequency. And μ_r (ϵ_r) is the relative permeability (permittivity) of the material with respect to that of the free space.

The following critical points can be identified

$$\omega_{mc} = \sqrt{\frac{\omega_{mp}^2 + \omega_{mo}^2}{2}} \qquad \text{for which } \mu_r(\omega_{mc}) = -1 \qquad (2.10a)$$

$$\omega_{ec} = \sqrt{\frac{\omega_{ep}^2 + \omega_{eo}^2}{2}} \qquad \text{for which } \epsilon_r(\omega_{ec}) = -1 \qquad (2.10b)$$

$$\omega_c = \sqrt{\frac{\omega_{ep}^2\omega_{mp}^2 - \omega_{eo}^2\omega_{mo}^2}{\omega_{ep}^2 + \omega_{mp}^2 - \omega_{eo}^2 - \omega_{mo}^2}} \qquad \text{for which } \mu_r(\omega_c)\epsilon_r(\omega_c) = 1 \qquad (2.10c)$$

A summary of the various frequency bands generated and their properties is shown in Fig. 2-4. The lower dark region corresponds to $n^2 > 1$, for which Čerenkov radiation can happen (supposing that $\beta = 1$).
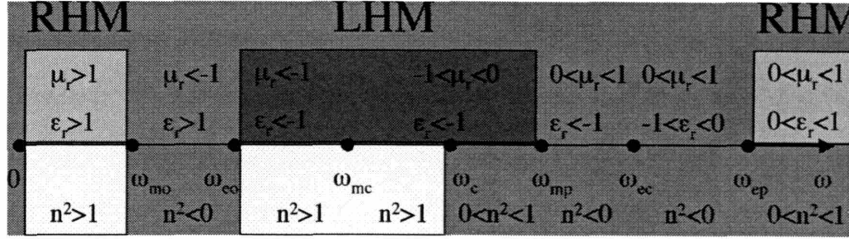
Figure 2-4: Frequency bands for RH and LH media obtained from the model of Eqs. (2.9a) and (2.9b).

The solution to Čerenkov radiation depends on frequency, as already shown in Eqs. (2.6a) to (2.7b). The band in which the region of $n^2 > 1$ overlaps with the RH media region, $\omega \in [0, \omega_{mo}]$, corresponds to positive ϵ_r and positive μ_r, and $n^2 = \epsilon_r\mu_r > 1$. From the conclusion of the previous section, the solution in this frequency band is the one of case 1. Similarly, for the LH media band and with $n^2 > 1$, $\omega \in [\omega_{eo}, \omega_c]$, the solution is the one of case 2. The nonvanishing field components produced by the propagating waves (in far field) are:

$$E_z(\overline{r}, t) = \frac{q}{4\pi} \sqrt{\frac{2}{\pi\rho}} \left[\int_0^{\omega_{mo}} (-)k_\rho \frac{\sqrt{k_\rho}}{\omega\epsilon(\omega)} \cos(\phi_+) \; d\omega + \int_{\omega_{eo}}^{\omega_c} k_\rho \frac{\sqrt{k_\rho}}{\omega\epsilon(\omega)} \cos(\phi_-) \; d\omega \right] \quad (2.11)$$

$$E_\rho(\overline{r}, t) = \frac{q}{4\pi v} \sqrt{\frac{2}{\pi\rho}} \left[\int_0^{\omega_{mo}} \frac{\sqrt{k_\rho}}{\epsilon(\omega)} \cos(\phi_+) \; d\omega + \int_{\omega_{eo}}^{\omega_c} \frac{\sqrt{k_\rho}}{\epsilon(\omega)} \cos(\phi_-) \; d\omega \right] \quad (2.12)$$

$$H_\phi(\overline{r}, t) = \frac{q}{4\pi} \sqrt{\frac{2}{\pi\rho}} \left[\int_0^{\omega_{mo}} \sqrt{k_\rho} \cos(\phi_+) \; d\omega + \int_{\omega_{eo}}^{\omega_c} \sqrt{k_\rho} \cos(\phi_-) \; d\omega \right] , \quad (2.13)$$

where $\phi_\pm = \omega t \mp k_\rho\rho - \frac{\omega z}{v} \pm \frac{\pi}{4}$, with the upper sign corresponding to case 1, and the lower sign corresponding to case 2. The Poynting vector $\overline{S}(\overline{r}, t) = \hat{z}S_z(\overline{r}, t) + \hat{\rho}S_\rho(\overline{r}, t) = \overline{E}(\overline{r}, t) \times \overline{H}(\overline{r}, t)$ is given by

$$S_z(\overline{r}, t) = E_\rho(\overline{r}, t)H_\phi(\overline{r}, t) = \frac{q^2}{8\pi^3\rho v}$$

$$\times \left[\int_0^{\omega_{mo}} d\omega \int_0^{\omega_{mo}} d\omega' \frac{\sqrt{k_\rho k_\rho'}}{\epsilon(\omega)} \cos(\phi_+) \cos(\phi_+') \right.$$

$$+ \int_{\omega_{eo}}^{\omega_c} d\omega \int_{\omega_{eo}}^{\omega_c} d\omega' \frac{\sqrt{k_\rho k_\rho'}}{\epsilon(\omega)} \cos(\phi_-) \cos(\phi_-')$$

$$+ \int_0^{\omega_{mo}} d\omega \int_{\omega_{eo}}^{\omega_c} d\omega' \frac{\sqrt{k_\rho k_\rho'}}{\epsilon(\omega)} \cos(\phi_+) \cos(\phi_-')$$

$$\left. + \int_{\omega_{eo}}^{\omega_c} d\omega \int_0^{\omega_{mo}} d\omega' \frac{\sqrt{k_\rho k_\rho'}}{\epsilon(\omega)} \cos(\phi_-) \cos(\phi_+') \right] , \quad (2.14)$$

33

$$S_\rho(\overline{r}, t) = -E_z(\overline{r}, t)H_\phi(\overline{r}, t) = \frac{q^2}{8\pi^3 \rho}$$

$$\times \left[\int_0^{\omega_{mo}} d\omega \int_0^{\omega_{mo}} d\omega' \frac{k_\rho \sqrt{k_\rho k'_\rho}}{\omega \epsilon(\omega)} \cos(\phi_+) \cos(\phi'_+) \right.$$

$$- \int_{\omega_{eo}}^{\omega_c} d\omega \int_{\omega_{eo}}^{\omega_c} d\omega' \frac{k_\rho \sqrt{k_\rho k'_\rho}}{\omega \epsilon(\omega)} \cos(\phi_-) \cos(\phi'_-)$$

$$+ \int_0^{\omega_{mo}} d\omega \int_{\omega_{eo}}^{\omega_c} d\omega' \frac{k_\rho \sqrt{k_\rho k'_\rho}}{\omega \epsilon(\omega)} \cos(\phi_+) \cos(\phi'_-)$$

$$\left. - \int_{\omega_{eo}}^{\omega_c} d\omega \int_0^{\omega_{mo}} d\omega' \frac{k_\rho \sqrt{k_\rho k'_\rho}}{\omega \epsilon(\omega)} \cos(\phi_-) \cos(\phi'_+) \right] . \qquad (2.15)$$

By using the identity [12]

$$\int_{-\infty}^{\infty} \cos(\omega t + \alpha) \cos(\omega' t + \alpha') dt = \pi \delta(\omega - \omega') \cos(\alpha - \alpha') , \qquad (2.16)$$

we can get the total energy radiated out in the $\hat{z}$ direction, W_z, and in the $\hat{\rho}$ direction, W_ρ:

$$W_z = \int_{-\infty}^{\infty} S_z dt = \frac{q^2}{8\pi^2 \rho v} \left[\int_0^{\omega_{mo}} d\omega \frac{k_\rho}{\epsilon(\omega)} + \int_{\omega_{eo}}^{\omega_c} d\omega \frac{k_\rho}{\epsilon(\omega)} \right] \qquad (2.17)$$

$$W_\rho = \int_{-\infty}^{\infty} S_\rho dt = \frac{q^2}{8\pi^2 \rho} \left[\int_0^{\omega_{mo}} d\omega \frac{k_\rho^2}{\omega \epsilon(\omega)} - \int_{\omega_{eo}}^{\omega_c} d\omega \frac{k_\rho^2}{\omega \epsilon(\omega)} \right] \qquad (2.18)$$

Because the speed of the high energy charged particle is very close to c, we can take the limit $\beta \to 1$. The interference between the components of the RH medium band and the LH medium band vanish due to time averaging.

- In the $\hat{z}$ direction:

  From Eq. (2.17), we see that the first integral is in a RH medium band ($\epsilon(\omega) > 0$ and $\mu(\omega) > 0$), and the energy flows along the positive $\hat{z}$ direction, which is the same as the direction of the particle motion. However, the second integral

is in a LH medium band ($\epsilon(\omega) < 0$ and $\mu(\omega) < 0$), the energy flows along the negative $\hat{z}$ direction, which corresponds to backward power flow. The total energy crossing the $x - y$ plane is determined by two frequency bands, and the net result will depend on which one is stronger. If we look at a single frequency, the energy will go in different directions.

- In the $\hat{\rho}$ direction:

  From Eq. (2.18), the first integral is in a RH medium band, so that the energy flows out of the $\hat{\rho}$ direction. The second integral is in a LH medium band, in which $\epsilon(\omega) < 0$, but there is a negative sign before the integral, which makes the whole second term to be positive. Therefore the energy in this LH medium band also goes out in the $\hat{\rho}$ direction.

2.4   Čerenkov radiation in lossy LH meda

From the Kramers-Krönig's relations, we know that $\epsilon(\omega)$ and $\mu(\omega)$ have to be complex to satisfy causality. Therefore, in order to predict the behavior of Čerenkov radiation in real LH media, we have to consider the situation when both the permittivity and the permeability are complex.

The complex permittivity $\epsilon(\omega)$ and permeability $\mu(\omega)$ must satisfy

$$\epsilon(-\omega) = \epsilon(\omega)^* \quad \text{with} \quad \epsilon_I(\omega) > 0 \tag{2.19a}$$

$$\mu(-\omega) = \mu(\omega)^* \quad \text{with} \quad \mu_I(\omega) > 0 \ . \tag{2.19b}$$

For lossy media, the condition for Čerenkov radiation is [14]

$$\Re\{n^2\} > \frac{1}{\beta^2} , \tag{2.20}$$

where $\Re\{.\}$ is the real part of the operator. The argument of the Hankel functions is now complex. However, the solutions of Eq. 2.5 are unchanged. In order to ensure finite electric and magnetic fields at $\rho \rightarrow +\infty$, we write

- For RH media: $g(\rho) = \frac{i}{4} H_0^{(1)}(k_\rho \rho)$,
  $k_\rho = \sqrt{\frac{\omega^2}{c^2} \mu_r \epsilon_r - \frac{\omega^2}{v^2}} = k_R + i k_I$, where $k_I > 0$, $k_R > 0$.

- For LH media: $g(\rho) = -\frac{i}{4} H_0^{(2)}(k_\rho \rho)$,
  $k_\rho = \sqrt{\frac{\omega^2}{c^2} \mu_r \epsilon_r - \frac{\omega^2}{v^2}} = k_R + i k_I$, where $k_I < 0$, $k_R > 0$.

For a RH medium band, we obtain a result identical to [14]. However, for a LH medium band, the nonvanishing fields are

$$E_\rho(\overline{r}, t) = \frac{q}{4\pi v} \sqrt{\frac{2}{\pi \rho}} \int_{LH} \frac{|k_\rho|^{1/2}}{|\epsilon(\omega)|} \cos(\omega t + k_R \rho - \frac{\omega}{v} z - \frac{\pi}{4} + \frac{\theta}{2} - \theta_\epsilon) e^{k_I \rho} \, d\omega \quad (2.21a)$$

$$E_z(\overline{r}, t) = \frac{q}{4\pi} \sqrt{\frac{2}{\pi \rho}} \int_{LH} \frac{|k_\rho|^{3/2}}{\omega |\epsilon(\omega)|} \cos(\omega t + k_R \rho - \frac{\omega}{v} z - \frac{\pi}{4} + \frac{3\theta}{2} - \theta_\epsilon) e^{k_I \rho} \, d\omega \quad (2.21b)$$

$$H_\phi(\overline{r}, t) = \frac{q}{4\pi} \sqrt{\frac{2}{\pi \rho}} \int_{LH} |k_\rho|^{1/2} \cos(\omega t + k_R \rho - \frac{\omega}{v} z - \frac{\pi}{4} + \frac{\theta}{2}) e^{k_I \rho} \, d\omega \quad (2.21c)$$

where θ is the angle of k_ρ by letting $k_\rho = \frac{\omega}{v} \eta e^{i\theta}$, and θ_ϵ is the angle of $\epsilon(\omega)$ in the complex plane by letting $\epsilon(\omega) = |\epsilon(\omega)| e^{i\theta_\epsilon}$. By using Eqs. (2.21a) to (2.21c), we can calculate the energy radiated out in the $\hat{\rho}$ and $\hat{z}$ directions for LH media and compare those with the corresponding components in RH media as obtained in [14]

- For RH media:

$$W_\rho = \int_{-\infty}^{\infty} S_\rho \, dt = \frac{q^2}{8\pi^2 \rho} \int_{RH} \frac{|k_\rho|^2}{\omega |\epsilon(\omega)|} e^{-2k_I \rho} \cos(\theta - \theta_\epsilon) \, d\omega \quad (2.22a)$$

$$W_z = \int_{-\infty}^{\infty} S_z \, dt = \frac{q^2}{8\pi^2 \rho v} \int_{RH} \frac{|k_\rho|}{|\epsilon(\omega)|} e^{-2k_I \rho} \cos(\theta_\epsilon) \, d\omega \quad (2.22b)$$

36

- For LH medium:

$$W_\rho = \int_{-\infty}^{\infty} S_\rho \, dt = \frac{q^2}{8\pi^2 \rho} \int_{LH} \frac{-|k_\rho|^2}{\omega|\epsilon(\omega)|} e^{2k_I \rho} \cos(\theta - \theta_\epsilon) \, d\omega \tag{2.23a}$$

$$W_z = \int_{-\infty}^{\infty} S_z \, dt = \frac{q^2}{8\pi^2 \rho v} \int_{LH} \frac{|k_\rho|}{|\epsilon(\omega)|} e^{2k_I \rho} \cos(\theta_\epsilon) \, d\omega \tag{2.23b}$$

We can see that the direction of power radiation is determined by the angles of $\epsilon(\omega)$ and k_ρ.

For a real physical model of permittivity and permeability, we should add an imaginary part to Eqs. (2.9a) and (2.9b), which now become

$$\mu_r = 1 - \frac{\omega_{mp}^2 - \omega_{mo}^2}{\omega^2 - \omega_{mo}^2 + i\gamma_m \omega} \tag{2.24a}$$

$$\epsilon_r = 1 - \frac{\omega_{ep}^2 - \omega_{eo}^2}{\omega^2 - \omega_{eo}^2 + i\gamma_e \omega} \tag{2.24b}$$
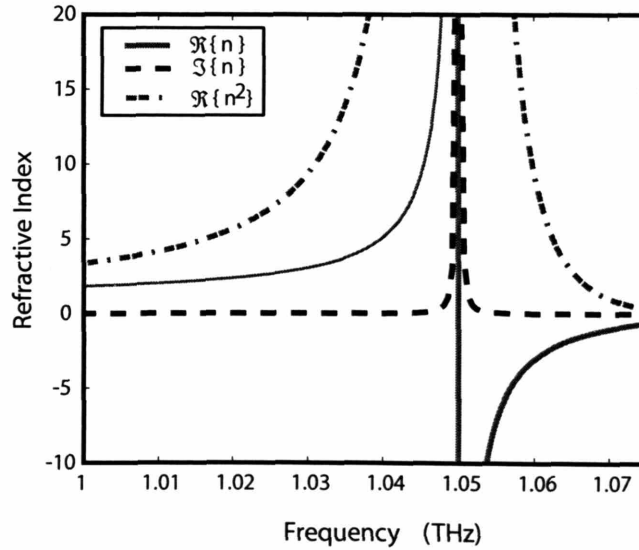
Figure 2-5: The red (solid) curve is for the real part of the refractive index, the black (dashed) curve is for the imaginary part, and the blue (dash-dotted) curve is for the real part of the square of the refractive index.

37

The real and imaginary parts of the complex refractive index n as well as the real part of n^2 are plotted in Fig. 2-5 as a function of frequency. Note that for such a model, we always have $\Im\{\epsilon(\omega)\} > 0$ and $\Im\{\mu(\omega)\} > 0$, where $\Im\{.\}$ indicates the imaginary part of the operator. These considerations are summarized in table 2.1, where θ_ϵ denotes the angle of $\epsilon(\omega)$ and θ the angle of k_ρ

Table 2.1: The range of angles for ϵ-θ_ϵ-and k_ρ-θ.

Properties	RH medium band	LH medium band
$\Re\{\epsilon(\omega)\}$	> 0	< 0
θ_ϵ	$[0, \frac{\pi}{2}]$	$[\frac{\pi}{2}, \pi]$
k_I	> 0	< 0
θ	$[0, \frac{\pi}{2}]$	$[\frac{3\pi}{2}, 2\pi]$

We see that we still have backward power flow in LH media, and the angles θ_ϵ and θ determine the direction of the power. The lossless limit implies that $\theta = 0$ for both LH and RH media, whereas $\theta_\epsilon = 0$ for RH media but $\theta_\epsilon = \pi$ for LH media. The expressions for the energy will reduce to Eqs. (2.17) and (2.18).

When losses exist, the directions of power propagation $\hat{S}$ (denoted by the angle θ_s)

$$\hat{S} = \frac{\hat{\rho}\eta\cos(\theta - \theta_\epsilon) + \hat{z}\cos(\theta_\epsilon)}{\sqrt{\eta^2\cos(\theta - \theta_\epsilon)^2 + \cos(\theta_\epsilon)^2}} \quad \text{for RH media} \quad (2.25)$$

$$\hat{S} = \frac{-\hat{\rho}\eta\cos(\theta - \theta_\epsilon) + \hat{z}\cos(\theta_\epsilon)}{\sqrt{\eta^2\cos(\theta - \theta_\epsilon)^2 + \cos(\theta_\epsilon)^2}} \quad \text{for LH media} \quad (2.26)$$

are different from that of phase propagation $\hat{k}$ (denoted by the angle θ_c)

$$\hat{k} = \frac{\hat{\rho}\eta\cos(\theta) + \hat{z}}{\sqrt{\eta^2\cos(\theta)^2 + 1}} \quad \text{for RH media} \quad (2.27)$$

$$\hat{k} = \frac{-\hat{\rho}\eta\cos(\theta) + \hat{z}}{\sqrt{\eta^2\cos(\theta)^2 + 1}} \quad \text{for LH media} \quad (2.28)$$

For the purpose of illustration, we plot the energy distribution as computed from Eqs.(2.22a) to (2.23b) by taking the model of Eqs. (2.24a) and (2.24b), and taking

38

the values $\omega_{mp} = \omega_{ep} = 2\pi \times 1.09 \times 10^{12}$ rad/s, $\omega_{mo} = \omega_{eo} = 2\pi \times 1.05 \times 10^{12}$ rad/s, and $\gamma_m = \gamma_e = \gamma$. All values are calculated at the same distance ρ for all frequencies.
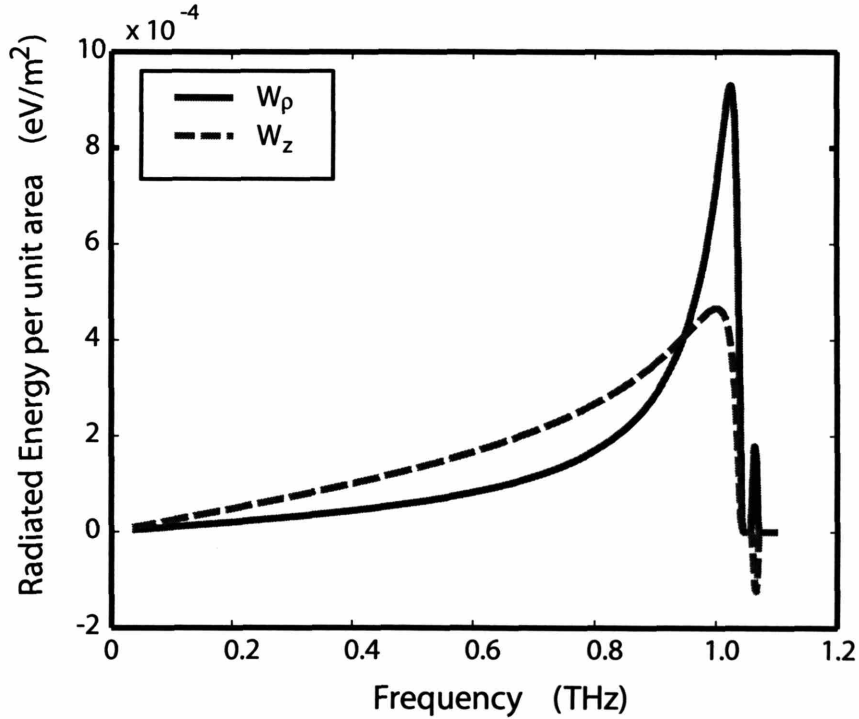
Figure 2-6: Energy distribution over frequency at $\gamma = 1 \times 10^8 Hz$. The blue (solid) line is the radiated energy density in the $\hat{\rho}$ direction, and the red (dashed) line is the radiated energy density in the $\hat{z}$ direction.

Fig. 2-6 shows the energy distributions W_z and W_ρ over frequency at $\gamma = 1 \times 10^8 Hz$. The high peak is in the RH medium regime for which $W_z > 0$, corresponding to a forward outgoing power. The small peak at $f \approx 1.06 \times 10^{12}$ rad/s corresponds to $W_\rho > 0$ and $W_z < 0$.

Figs. 2-7(a) to 2-7(d) show the radiation patterns of Čerenkov radiation at different γ. We can see from Fig. 2-7(a) that, when the losses are high, there is mainly forward power from the low frequencies far from the resonance. The radiations near the resonance are negligible since the radiation decays very fast due to high loss. As the losses decrease, we can find from Figs. 2-7(b) that the backward lobe appears.
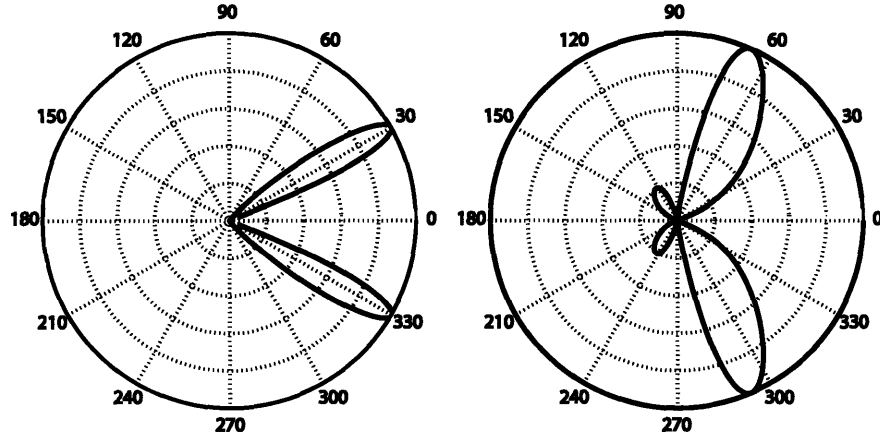
(a) $\gamma = 1 \times 10^{10} Hz$, normalizing constant 1.8×10^{-4}.

(b) $\gamma = 1 \times 10^{8} Hz$, normalizing constant 0.001.
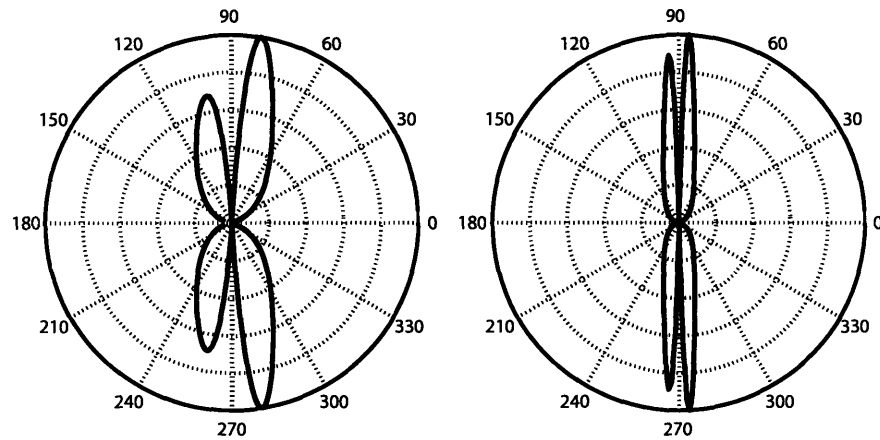
(c) $\gamma = 1 \times 10^{7} Hz$, normalizing constant 0.0026.

(d) $\gamma = 1 \times 10^{6} Hz$, normalizing constant 0.0074.

Figure 2-7: Radiation pattern of Čerenkov radiation for a material characterized by Eqs.(2.24a) and (2.24b).

40

This is because the initial radiation near the resonance is actually much higher than those in Fig. 2-7(a). When the loss continues decreasing, as shown in Figs. 2-7(c) and 2-7(d), the backward lobe becomes comparable with the forward lobe, and both approach to 90° because the large refractive index near resonance. The radiation is dominated by the frequency in the region near the resonant frequency, where lossess are so small and the decay term is not strong enough to suppress the amplitude. If the distance ρ increases, the decay term will become dominant, therefore the lobe for backward power will be suppressed, and the pattern will become like the one of Fig. 2-7(a).
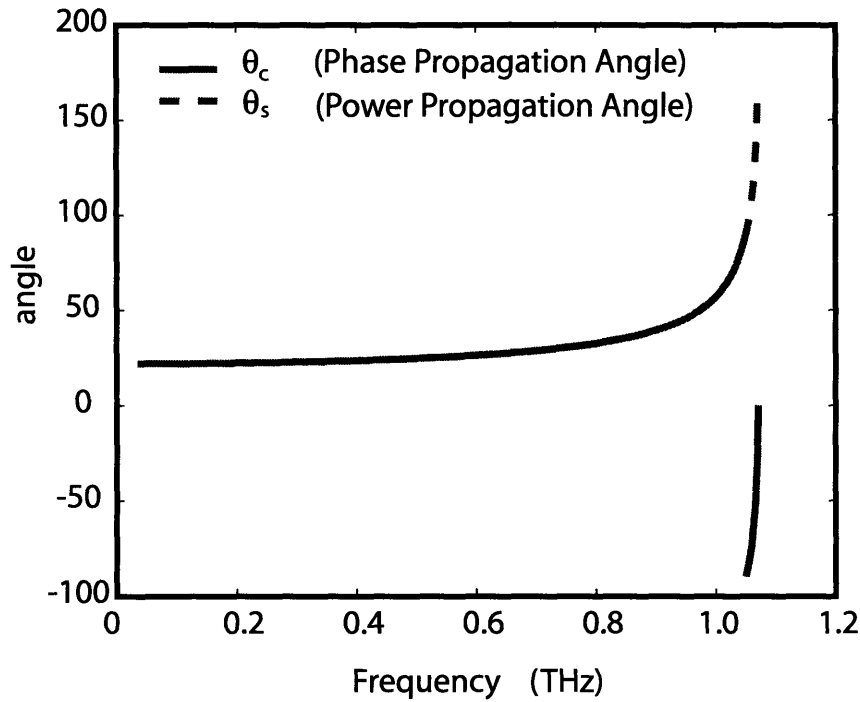
Figure 2-8: The distributions of angle over frequency at $\gamma = 1 \times 10^8$Hz. The blue (solid) curve is the power propagation angle, and the red (dashed) curve is the phase propagation angle.

Another noticeable phenomenon is that the angles of forward and backward power are both close to 90° as the losses decrease. This is due to the value of the refractive index which becomes extremely large, see Eq. (2.2).

In addition we see that the direction of phase propagating is different from that of power propagating. This difference is due to the losses. We find from Fig. 2-8, that for a RH medium band, there is almost no difference between these two angles, which is due to the imaginary part being very small at this frequency band, and therefore the angles θ and θ_ϵ are very small. For a LH medium band however, the direction of phase propagation is almost opposite to that of the power.

2.5   Conclusion

In this chapter, we have given the mathematical solution for Čerenkov radiation in a left-handed material, for both lossless and lossy situations. We have found, consistently with the prediction in [1], that Čerenkov radiation in LH media exhibits a backward power, yet maintaining a forward $\bar{k}$ vector.

With a simple model for the permittivity and the permeability, we have observed that the radiation pattern of the Čerenkov radiation presents lobes at very large angles, close to 90° with respect to the particle motion, which is in contrast with the angle obtained in a classical gas environment. With such a large angle, we expect more photons to be generated, implying the fundamental idea of improved Čerenkov detectors based on the use of LH media.

Chapter 3

Čerenkov Radiation in a Cylindrical Wave Guide Filled with Left-Handed Materials

3.1   Introduction

Since no material except vacuum can be strictly regarded as unbounded, we will discuss a more realistic case here. In Chapter 2, we have shown [6] that the radiated energy will go forward and backward at different frequency bands when the dispersion exists. It was known that the intensity of the radiation is inversely proportional to the wavelength, and therefore, normally only the radiation at optical frequencies are detectable. This is probably a major reason for preventing researchers from experimentally confirming the reversed Čerenkov radiation, since the LHMs at optical frequencies are still under investigation. Knowing the fact that the studies and technique are quite mature in the microwave frequency range, we propose a possible experimental design which could be used to detect reversed Čerenkov radiation in LHM at frequencies near GHz. The idea is borrowed from the well studied Čerenkov free electron maser, where high intensity charged particles travel along the axis of a cylindrical waveguide, in which the dielectric is filled. Due to the effect of the metallic

wall outside the core medium, Čerenkov radiation only happens at frequencies where the guidance condition for the waveguide is satisfied.

In this chapter, we first summarized the Green's function for different cases, which can serve as a theory basis for our following analysis.

We then studied a classic case, a two layer problem for which a RHM core is covered by a LHM layer. We call it "classic" because this was actually a topic proposed by a committee member when Čerenkov made his defense, and was extensively studied by the following researchers. Here we just change the out layer to be an LHM instead of a RHM. Interestingly, besides the obvious results that the power will propagate backward in LHM, we do find that an LHM has more mechanism than a RHM for particles to lose energy, as summarized in Table 3.1. In row 2, it shows that there will be surface plasmon between the boundary of the RHM core, and the LHM outer layer, whereas there is no radiation when both layers are RHMs.

Table 3.1: Radiation Mechanism for Different Conditions

	Outer layer is a RHM	Out layer is a LHM
$n_1^2\beta^2 < 1$ and $n_2^2\beta^2 > 1$	Forward propagating wave in the outer layer Forward evanescent wave in the core	Backward propagating wave in the out layer Forward evanescent wave in the core
$n_1^2\beta^2 < 1$ and $n_2^2\beta^2 < 1$	no radiation	Backward surface plasmon in the outer layer Forward surface plasmon in the core
$n_1^2\beta^2 > 1$ and $n_2^2\beta^2 > 1$	Forward propagating wave in both layers	Backward propagating wave in the outer layer Forward Propagating wave in the core
$n_1^2\beta^2 > 1$ and $n_2^2\beta^2 < 1$	Guided forward propagating wave in the core Forward evanescent wave in the outer layer	Guided forward propagating wave in the core Backward evanescent wave in the outer layer

Thirdly, Čerenkov radiation for a metallic wave guide completely and partly filled with LHM is discussed and demonstrated with numerical results with realistic models

44

of the permittivity and permeability; finally, we calculated a 3 layer problem, where the core is a vacuum channel, and the middle layer is a LHM. Here the ability of compensating the decay of the radiation by the channel is shown as a result of the excited surface plasmon between the boundaries of a LHM and RHMs.

3.2 Green's function for different cases

3.2.1 Approach

The approach is the same as in chapter 2, from Eq. (2.3) to Eq. (2.5).

The task is reduced to finding the scalar Green's function, with which the fields can be expressed as follows

$$E_z(\overline{r}, \omega) = \frac{iq}{2\pi\omega\epsilon} e^{i\omega z/v} \left(\omega^2\epsilon\mu - \frac{\omega^2}{v^2} \right) g(\rho) \, , \tag{3.1a}$$

$$E_\rho(\overline{r}, \omega) = -\frac{q}{2\pi\epsilon v} e^{i\omega z/v} \frac{\partial}{\partial\rho} g(\rho) \, , \tag{3.1b}$$

$$H_\phi(\overline{r}, \omega) = -\hat{\phi} \frac{q}{2\pi} e^{i\omega z/v} \frac{\partial}{\partial\rho} g(\rho) \, . \tag{3.1c}$$

3.2.2 Green's functions for different conditions.

The Green's function for the unbounded region including the source and infinity were already discussed in Chapter 2 [6]. Here we only consider two geometric regions.

Table 3.2: The Green's functions are summarized according to different regions, and whether the Čerenkov radiation condition is satisfied or not, i.e. $n^2\beta^2 > 1$ or $n^2\beta^2 < 1$. We limited ourselves here with the permittivity and permeability being real.

	$n^2\beta^2 > 1$	$n^2\beta^2 < 1$
Wave Vector	$k_\rho = \sqrt{\omega\mu\epsilon - \frac{\omega^2}{v^2}} > 0$	$s = \sqrt{\frac{\omega^2}{v^2} - \omega\mu\epsilon} > 0$
$0 \leq \rho < a$	$-\frac{1}{4} N_0(k_\rho\rho) + \alpha J_0(k_\rho\rho)$	$\frac{1}{2\pi} K_0(s\rho) + \alpha I_0(s\rho)$
$a < \rho < b$	$\xi N_0(k_\rho\rho) + \zeta J_0(k_\rho\rho)$	$\xi K_0(s\rho) + \zeta I_0(s\rho)$
$b < \rho < \infty$	$\eta H_0^{(1)}(k_\rho\rho) + \gamma H_0^{(2)}(k_\rho\rho)$	$\eta K_0(s\rho)$

The coefficient $\gamma = 0$ if the media is a RHM, and $\eta = 0$ if it is a LHM to ensure an out flowing energy.

The coefficients are found by matching the boundary conditions, which are reduced to match $\left(\omega^2 \mu_i \epsilon_i - \frac{\omega^2}{v^2}\right) \frac{1}{\epsilon_i} g_i(\rho)$, and $\frac{\partial}{\partial \rho} g_i(\rho)$.

3.3   A Two layer problem

Since a LHM is a composite metamaterial, it is more realistic to consider a two layered configuration, where the core is a RHM with a finite radius. When a charged relativistic particle passes through the axis, the phenomenon of the radiation in the outer layer being a LHM are different from that of the RHM. We assume that the medium in the region $0 \le \rho < a$ has permittivity ϵ_1 and permeability μ_1, the medium in the outer region 2 has ϵ_2 and μ_2, and we limit ourselves in the case that all media are lossless. We assume that the medium 1 is always a RHM without loss of generality. In order to make a comparison, we list the result of region 2 being a RHM [15] also. $n_i^2 = \epsilon_{ir}\mu_{ir}$ is used throughout the paper.
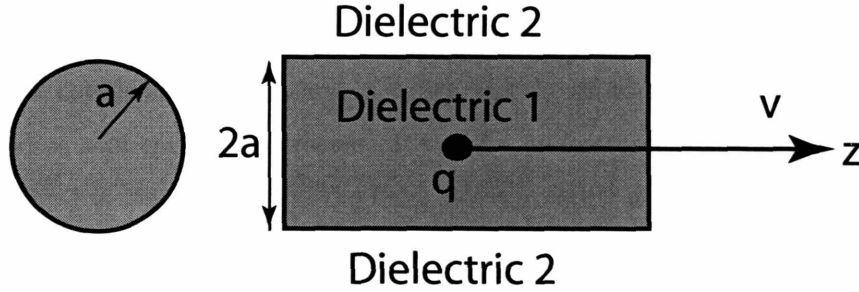
Figure 3-1: A charged particle with the velocity $\bar{v}$ travels along the axis of the cylinders in $\hat{z}$ direction. a RHM is located at the core with a radius of a, and the outer layer is another dielectric material which could be either a RHM or a LHM.

3.3.1 Case 1: $n_1^2\beta^2 < 1$, and $n_2^2\beta^2 > 1$

The Green's functions should be chosen from Table 3.2 accordingly.

When the medium 2 is a RHM, the radiated wave is evanescent in region 1, but propagating in region 2. The power is flowing forward. The coefficients are found as

$$\alpha_{RHM} = \frac{1}{2\pi}\frac{p_{12}K_1(s_1a)H_0^{(1)}(k_{2\rho}a) + K_0(s_1a)H_1^{(1)}(k_{2\rho}a)}{p_{12}I_1(s_1a)H_0^{(1)}(k_{2\rho}a) - I_0(s_1a)H_1^{(1)}(k_{2\rho}a)} , \qquad (3.2a)$$

$$\eta_{RHM} = \frac{-1}{2\pi a k_{2\rho}}\frac{1}{p_{12}I_1(s_1a)H_0^{(1)}(k_{2\rho}a) - I_0(s_1a)H_1^{(1)}(k_{2\rho}a)} . \qquad (3.2b)$$

where $p_{12} = \epsilon_1 k_{2\rho}/\epsilon_2 s_1$.

The energy loss per unit path is

$$\frac{dW}{dz} = 2\pi\rho\int_{-\infty}^{\infty} S_\rho(\overline{r}, t)\, dt = \frac{4q^2}{\pi}\int_0^{\infty} d\omega\, \mu_2\left(1 - \frac{1}{\mu_2\epsilon_2 v^2}\right)|\eta(\omega)|^2\omega , \qquad (3.3)$$

where $S_\rho(\overline{r}, t) = -E_z(\overline{r}, t)H_\phi(\overline{r}, t)$ is the ρ component of the Poynting vector. The effect of the core is in the coefficient η, which was shown to be decaying exponentially as the radius a of the core increases. It can be understood that the radiated wave inside region 1 is evanescent, and the fields decay roughly as $e^{-s_1\rho}$. The radiation will decay much faster as the radius a increases.

When region 2 is a LHM with $\epsilon_2 < 0, \mu_2 < 0$, the only difference between the RHM is that for the RHM the Green's function in region 2 should be $H_0^{(2)}(k_{2\rho}\rho)$, as discussed in [6]. The corresponding coefficients are just the complex conjugate of that in Case 1, and can be written as

$$\alpha_{LHM} = \frac{1}{2\pi}\frac{p_{12}K_1(s_1a)H_0^{(2)}(k_{2\rho}a) + K_0(s_1a)H_1^{(2)}(k_{2\rho}a)}{p_{12}I_1(s_1a)H_0^{(2)}(k_{2\rho}a) - I_0(s_1a)H_1^{(2)}(k_{2\rho}a)}$$

$$= \alpha_{RHM}^* , \qquad (3.4a)$$

$$\gamma_{LHM} = \frac{-1}{2\pi a k_{2\rho}}\frac{1}{p_{12}I_1(s_1a)H_0^{(2)}(k_{2\rho}a) - I_0(s_1a)H_1^{(2)}(k_{2\rho}a)}$$

$$= \eta_{RHM}^* , \qquad (3.4b)$$

where p_{12} is the same as defined for the RHM.

Since the energy loss only depends on $|\gamma(\omega)|^2 = |\eta(\omega)|^2$, the dependence on the radius for the center cylinder should be same. In the outer layer, the power will flow backward for a LHM [6].

3.3.2 Case 2: $n_1^2\beta^2 < 1$, and $n_2^2\beta^2 < 1$

For this case, the waves in both regions are evanescent. Limited by the boundary condition at infinity, where the field has to vanish, the $K_0(s_2\rho)$ will be the Green's function for the medium in region 2 being either a RHM or a LHM.

The coefficients α and η are now written as

$$\alpha = \frac{1}{2\pi}\frac{p_{12}K_1(s_1a)K_0(s_2a) - K_0(s_1a)K_1(s_2a)}{p_{12}I_1(s_1a)K_0(s_2a) + I_0(s_1a)K_1(s_2a)} \ , \tag{3.5a}$$

$$\eta = \frac{1}{2\pi a s_2}\frac{1}{p_{12}I_1(s_1a)K_0(s_2a) + I_0(s_1a)K_1(s_2a)} \ . \tag{3.5b}$$

where $p_{12} = \epsilon_1 s_2/\epsilon_2 s_1$.

The energy loss can be calculated as follows [15]

$$\frac{dW}{dz} = \lim_{\rho\to 0, z\to vt} qE_z = \frac{q^2}{2\pi}2\Re\int_0^\infty d\omega \ i\omega\mu_1\left(1 - \frac{1}{\mu_1\epsilon_1 v^2}\right)\alpha \ . \tag{3.6}$$

When region 2 is a RHM, the integral is purely imaginary, the particle will not lose energy in this case. However, the situation is different when region 2 is a LHM, because a pole can exist in α when the denominator is zero,

$$p_{12}I_1(s_1a)K_0(s_2a) + I_0(s_1a)K_1(s_2a) = 0 \ , \tag{3.7}$$

where the modified Bessel functions are always positive, and $p_{12} < 0$ for a LHM, and $p_{12} > 0$ for a RHM. When Eq. (3.7) is satisfied, the residue should be calculated as $2\pi i a_{-1}$, and the energy loss is proportional to a summation of the residues at discrete frequencies. These frequencies correspond to the excited surface plasmons. Therefore, the particle will lose energy, and excite the surface plasmons on the interface between

the RHM core and the LHM outer layer.

3.3.3 Case 3: $n_1^2\beta^2 > 1$, and $n_2^2\beta^2 > 1$

In this case, the radiations are propagating waves in both regions. There will be a positive refraction when the medium in region 2 is a RHM, and a negative refraction when the medium in region 2 is a LHM.

The coefficients for a RHM are solved as

$$\alpha_{RHM} = \frac{1}{4}\frac{p_{12}N_1(k_{1\rho}a)H_0^{(1)}(k_{2\rho}a) - N_0(k_{1\rho}a)H_1^{(1)}(k_{2\rho}a)}{p_{12}J_1(k_{1\rho}a)H_0^{(1)}(k_{2\rho}a) - J_0(k_{1\rho}a)H_1^{(1)}(k_{2\rho}a)} , \tag{3.8a}$$

$$\eta_{RHM} = \frac{-1}{2\pi a k_{2\rho}}\frac{1}{p_{12}J_1(k_{1\rho}a)H_0^{(1)}(k_{2\rho}a) - J_0(k_{1\rho}a)H_1^{(1)}(k_{2\rho}a)} . \tag{3.8b}$$

where $p_{12} = \epsilon_1 k_{2\rho}/\epsilon_2 k_{1\rho}$.

Similarly, the coefficients for a LHM are solved as

$$\alpha_{LHM} = \frac{1}{4}\frac{p_{12}N_1(k_{1\rho}a)H_0^{(2)}(k_{2\rho}a) - N_0(k_{1\rho}a)H_1^{(2)}(k_{2\rho}a)}{p_{12}J_1(k_{1\rho}a)H_0^{(2)}(k_{2\rho}a) - J_0(k_{1\rho}a)H_1^{(2)}(k_{2\rho}a)} , \tag{3.9a}$$

$$\gamma_{LHM} = \frac{-1}{2\pi a k_{2\rho}}\frac{1}{p_{12}J_1(k_{1\rho}a)H_0^{(2)}(k_{2\rho}a) - J_0(k_{1\rho}a)H_1^{(2)}(k_{2\rho}a)} . \tag{3.9b}$$

3.3.4 Case 4: $n_1^2\beta^2 > 1$, and $n_2^2\beta^2 < 1$

In this case, the wave is propagating inside region 1, and is total reflected at the boundary, and an evanescent decaying wave is formed in region 2.

The coefficients are solved as

$$\alpha = \frac{1}{4}\frac{p_{12}N_1(k_{1\rho}a)K_0(s_2a) + N_0(k_{1\rho}a)K_1(s_2a)}{p_{12}J_1(k_{1\rho}a)K_0(s_2a) + J_0(k_{1\rho}a)K_1(s_2a)} , \tag{3.10a}$$

$$\eta = \frac{1}{2\pi a s_2}\frac{1}{p_{12}J_1(k_{1\rho}a)K_0(s_2a) + J_0(k_{1\rho}a)K_1(s_2a)} . \tag{3.10b}$$

where $p_{12} = \epsilon_1 s_2/\epsilon_2 k_{1\rho} > 0$.

49

The energy lost is determined by

$$\frac{dW}{dz} = \frac{q^2}{2\pi} 2\Re \lim_{\rho \to 0} \int_0^\infty d\omega \ i\omega\mu_1 \left(1 - \frac{1}{\mu_1\epsilon_1 v^2}\right) \alpha \ , \tag{3.11}$$

The radiation only happens at the poles of α, for which the following condition is satisfied,

$$p_{12} J_1(k_{1\rho}a) K_0(s_2 a) + J_0(k_{1\rho}a) K_1(s_2 a) = 0 \ . \tag{3.12}$$

The energy lost becomes the summation of the residue of the discrete frequencies when the guidance condition is satisfied.

When the outer layer is a LHM, the formulations are still the same. The poles are determined by the same equation, but they occur at different positions since $p_{12} < 0$ now.

3.4 Čerenkov radiation in a metallic wave guide filled with a LHM

3.4.1 Metallic wave guide fully filled with a LHM

For this case, the configuration is the same as in Fig. 3-1, except that the dielectric 2 is changed into a perfect electric conductor (PEC), which is a very good approximation for a metal in GHz frequency band.

When the Čerenkov radiation condition is satisfied, the Green's function for this problem is

$$g(\rho) = -\frac{1}{4} N_0(k_\rho \rho) + \alpha J_0(k_\rho \rho) \ . \tag{3.13}$$

At $\rho = a$, the boundary condition requires $E_z(\rho = a) = 0$, the α is then determined,

$$\alpha = \frac{N_0(k_\rho a)}{4 J_0(k_\rho a)} \ . \tag{3.14}$$

The energy lost by the moving charge due to the Čerenkov radiation is calculated

as the electric field acting on the charge itself [15],

$$\frac{dW}{dz} = \frac{q^2}{\pi} Re \lim_{\rho \to 0} \int_0^\infty d\omega \, \frac{i\omega}{\epsilon} \left(\mu\epsilon - \frac{1}{v^2} \right)$$
$$\times \left[-\frac{1}{4} N_0(k_\rho \rho) + \frac{N_0(k_\rho a)}{4 J_0(k_\rho a)} J_0(k_\rho \rho) \right] . \tag{3.15}$$

When the material is lossless, the energy loss becomes a summation of the residues of the discrete frequencies, which are actually the guided modes by the same reason as for case 4.

When there is no dispersion, the energy loss is [15]

$$\frac{dW}{dz} = \frac{2q^2}{4\pi a^2 \epsilon} \sum_{m=1}^{\infty} \frac{1}{[J_0'(u_m)]^2} \tag{3.16}$$

where u_m is the mth zero of $J_0(x)$, and $\omega_m = u_m / (a\sqrt{\mu_r \epsilon_r - \frac{1}{v^2}})$.

Required by the causality, a LHM is always dispersive, and therefore we studied the energy loss when the dispersion exists. In the microwave frequency range, the LHM is realized by SRRs, and metallic rods, which can be approximated using the known dispersion models, Lorentz and Drude models, respectively [16]. We use the same model as in [16], since the parameters were chosen according to the experimental results.

$$\epsilon_r(\omega) = 1 - \frac{\omega_p^2}{\omega^2 + i\gamma_e \omega} , \tag{3.17a}$$

$$\mu_r(\omega) = 1 - \frac{F\omega^2}{\omega^2 - \omega_0^2 + i\gamma_m \omega} . \tag{3.17b}$$

where $\omega_p = 2\pi \times 10$ GHz is the effective plasma frequency for the metallic rods, $\omega_0 = 2\pi \times 4$ GHz is the resonant frequency for SRRs, $F = 0.56$, γ_e are γ_m are the collision frequencies which account for the loss of the material. The real parts of $\epsilon_r(\omega)$ and $\mu_r(\omega)$ are plotted in Fig. 3-2.
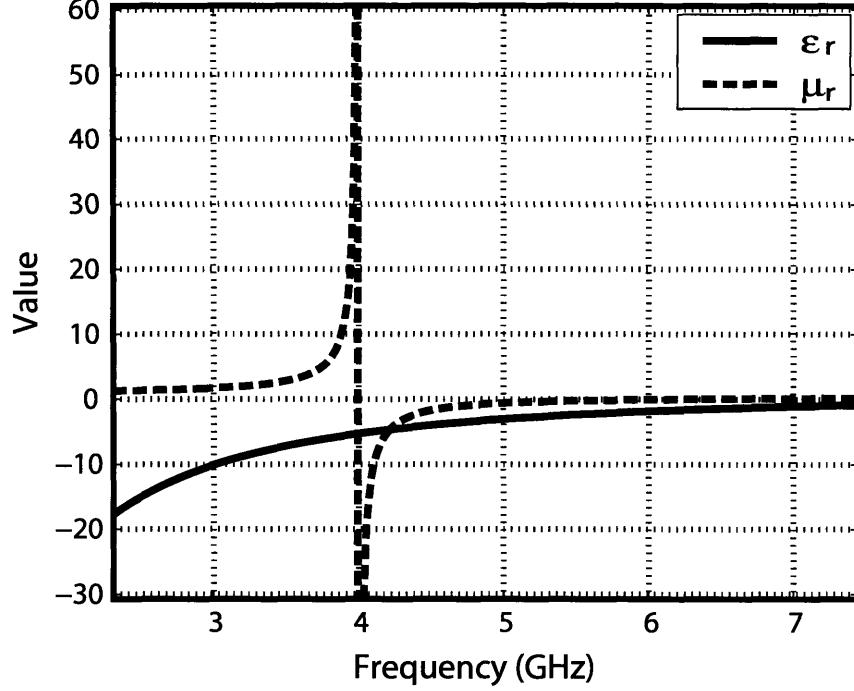
Figure 3-2: The permittivity and permeability from the model in Eqs. (3.17a) and (3.17b). The loss is assumed to be zero. Both permittivity and permeabilty are negative in the frequency range [4, 6] GHz.

When the collision frequencies are zero, the permittivity and permeability are both real, for which the derivative with respect to the frequency should be considered. The energy loss is then represented as [15]

$$\frac{dW}{dz} = \frac{q^2}{2\pi a^2} \sum_m \frac{u_m}{\epsilon(\omega_m)\omega_m J_1(u_m)^2 a \frac{\partial}{\partial \omega}\frac{\omega}{v}\sqrt{\mu_r \epsilon_r \beta^2 - 1}} \qquad (3.18)$$

where ω_m can be easily solved by plugging the models of Eq. (3.17a) for permittvity $\epsilon_r(\omega)$ and Eq. (3.17b) for permeability $\mu_r(\omega)$ into

$$\frac{\omega_m}{v} a \sqrt{\mu_r(\omega_m)\epsilon_r(\omega_m)\beta^2 - 1} = u_m . \qquad (3.19)$$

52
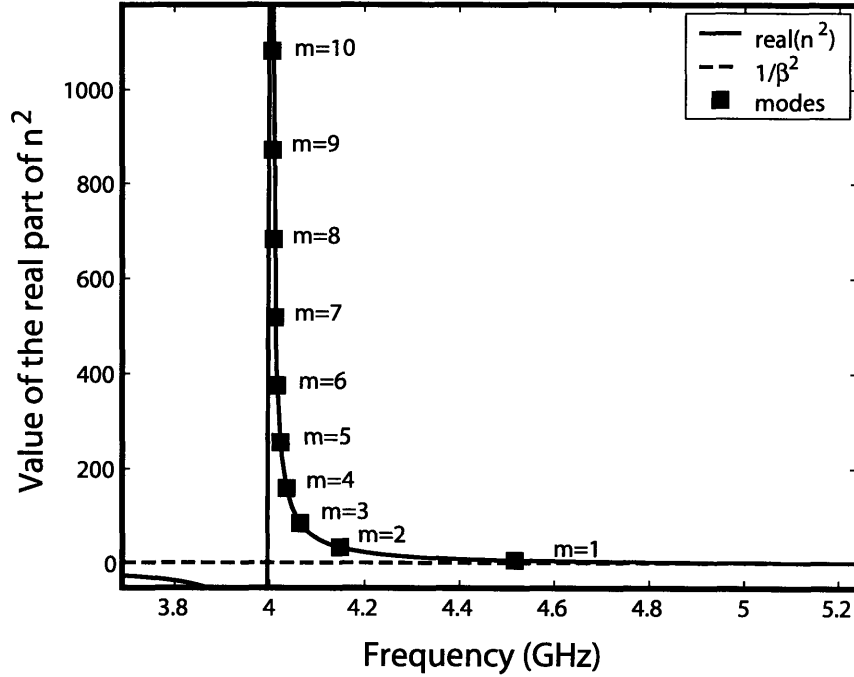
Figure 3-3: The discrete modes for the lossless dispersive LHM where the Čerenkov radiation is satisfied. The velocity of the charged particle is $\beta = 0.9$, and the radius of the waveguide is $a = 1cm$. The continuous curve is $\Re\{n^2\} = \Re\{\epsilon_r \mu_r\}$, the dashed line indicates the value of $\frac{1}{\beta^2}$, above which the condition $\Re\{n^2\beta^2\} > 1$ is satisfied, and Čerenkov radiation can happen. The discrete modes determined by Eq. (3.19) are depicted by the filled squares.

The positions of the modes are depicted in Fig. 3-3. We can find that as the order of the modes m increases, the frequency decreases, which is contrary to that of a non-dispersion material, where the frequency increases as m increases. This result is due to the strong dispersion of the permeability near the resonant frequency.

When the loss is considered, the singularities disappear. The energy loss can be directly calculated from Eq. (3.15). In order for comparison, we also calculated the energy loss when the LHM is not bounded by the metallic wall. The results are shown in Fig. 3-4.

53
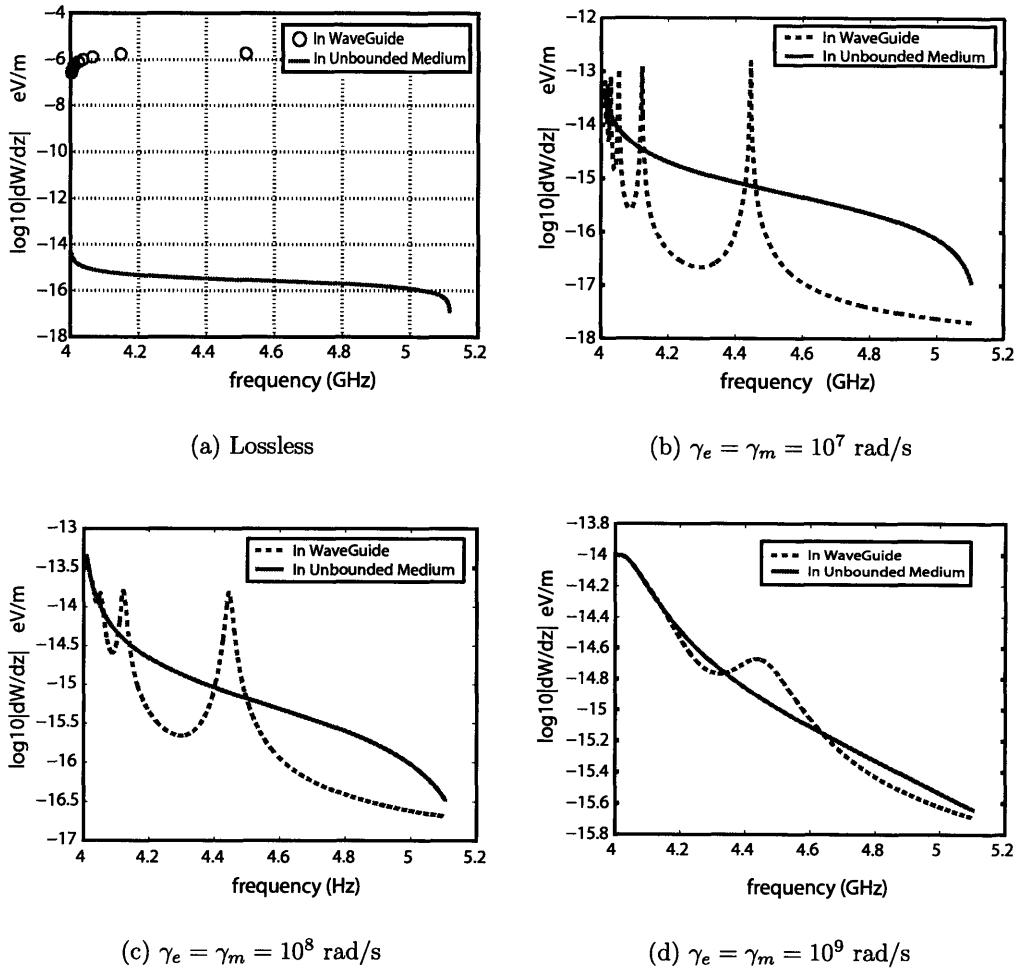
Figure 3-4: The energy loss for different values of collision frequencies γ_e, and γ_m. (a) lossless case where $\gamma_e = \gamma_m = 0$; (b) $\gamma_e = \gamma_m = 10^7$ rad/s; (c) $\gamma_e = \gamma_m = 10^8$ rad/s; (d) $\gamma_e = \gamma_m = 10^9$ rad/s. The energy loss for both waveguide and unbounded case are calculated.

Fig. 3-4(a) indicates the discrete frequencies, marked as hollow circles, at which particles radiate energy. These modes are corresponding to those marked in Fig. 3-3. As the frequency goes to the resonant frequency, the modes become denser. It is worth noting that the radiated energy at discrete frequencies in the waveguide is much higher than that of the unbounded case, depicted as red (continuous) curve. At those particular frequencies, the radiation is greatly enhanced by almost 9 orders. However, if we compare the total radiated energy in the frequency band [4.002,5.117] GHz in

which the Čerenkov radiation condition is satisfied, i.e. we compare the summation of energy loss per unit length at the discrete frequencies with $m = 1, 2, ..., 15$ which are marked as hollow circle in Fig. 3-3, and the integration of the continuous spectrum for an unbounded case which is plotted as the solid curve in Fig. 3-3. For the example we used, the total radiated energy per unit length in a waveguide is $dW_{waveguide}/dz = 1.07 \times 10^{-5}$eV/m while the total energy loss per unit length, when the metallic bound is removed, is $dW_{unbounded}/dz = 2.4653 \times 10^{-6}$eV/m. It is seen that the charged particle will radiate four times more energy in a waveguide. The main effect of the waveguide is to make the radiated energy concentrate at those frequencies which could resonant in the waveguide, i.e. the guidance condition is satisfied. The frequency range where we made the comparison is a little bit off from the resonant frequency 4 GHz. The reason is that the number of modes will go to infinity because of the singularity of μ when the losses are ignored. Meanwhile, the radiated energy of the unbounded case will also blow up since μ goes to infinity. Therefore there is of no physical meaning to include the frequencies which are too close to the resonant frequency, since all the singular behaviors will be canceled once the loss is considered. However, the previous comparison is still valid, which will be demonstrated when we explore the results where the loss is included.

When we consider the loss by increasing the collision frequencies γ_e and γ_m, the radiation spectrum becomes continuous. From Figs. 3-4(b) to 3-4(d), we can find that the radiated energy per unit length has peaks at the frequencies which correspond to those guided modes in the lossless case as in Fig. 3-3. The amplitude of the radiated energy is much higher at the frequencies of the guided modes than others. As the loss increases, the peaks become wider, and the peaks near the resonant frequency are less and less separated, since the loss is very high near the resonant frequency which make the arguments of the Bessel function being further from the zeros. Also the difference between the radiated energy at the frequencies of guided modes and other frequencies becomes smaller. The radiated spectrum is getting closer to that of the unbounded case for larger losses. This could be understood as the waves decay very fast after they are radiated from the particle in high loss materials. Therefore

the wave reflected by the PEC is very weak and cannot form a strongly constructive resonance inside the waveguide. It is also limited by the PEC waveguide that there is no guided evanescent wave to be supported.
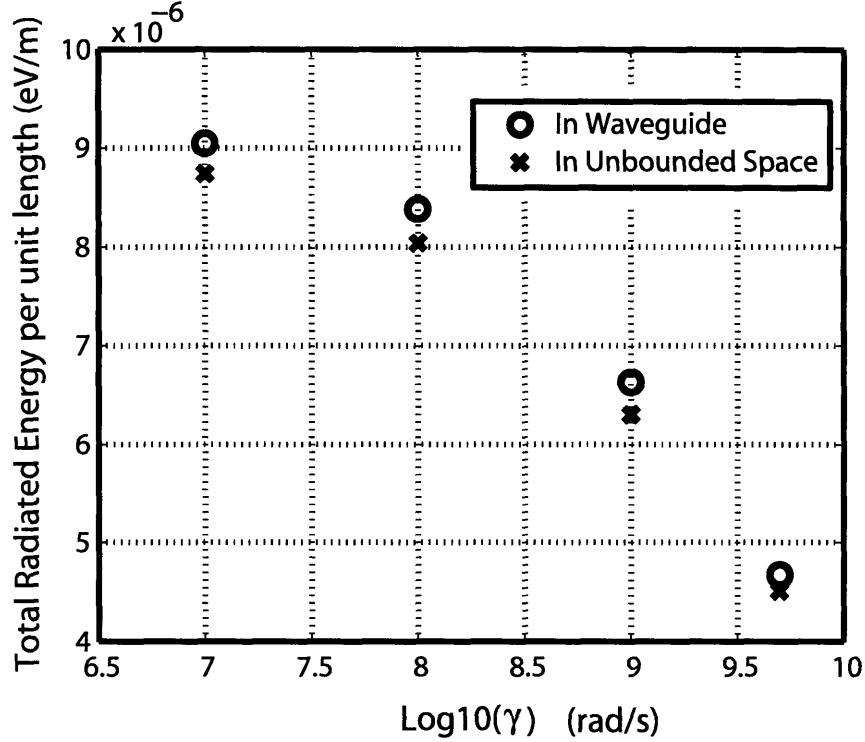
Figure 3-5: The total radiated energy per unit length for different losses, where the loss is indicated by the collision frequency $\gamma = \gamma_e = \gamma_m$. For simplicity, we assume that the permittivity and permeability have the same collision frequencies. The circles indicate the total radiated energy per unit length in a waveguide, while the cross indicates that of the unbounded case.

To study the effect of the loss on the total radiated energy, the numerical integration is performed to calculate the total radiated energy per unit path for the cases shown in Figs. 3-4(b) to 3-4(d). The results are shown in Fig. 3-5. It is seen that the total radiated energy increases as the loss decreases for both cases, which will finally converge to the lossless cases, respectively. Even when the loss exists, the charged particle always loses more energy when it travels inside the waveguide than that in the unbounded LHM. This result is consistent with the analysis for the lossless case. As the loss increases, the differences between the two cases are getting smaller, which

is a direct result of the fact that the radiated energy distributions tend to overlap when the loss increases.

The direction of the energy is along the cylinder axis which is determined by the sign of the permittivity ϵ, and the energy will flow in the same direction as the particle motion $\hat{z}$ when $\Re\{\epsilon\} > 0$, and in the opposite direction $-\hat{z}$ when $\Re\{\epsilon\} < 0$, which is the case in Figs. 3-4.

3.4.2 The effect of the radiation of a vacuum channel in the center of the waveguide

Currently, the LHMs are composite structures with different materials, such as the metallic strips for the split ring resonators (SRRs) and rods and dielectric materials for holding the strips. Complicated interactions could happen when the relativistic charged particles go through these materials, such as transition radiation, ionization loss, all of which could add lots of noise for the possible experimental detection of the above discussed Čerenkov radiation. Therefore it might be better to leave a vacuum channel as a channel in the center to allow the particle to pass. The noise due to the interaction between the particle and the materials used for construction can be avoided. Therefore, the effect of the hollow hole is studied in this section with a configuration shown in Fig. 3-6.
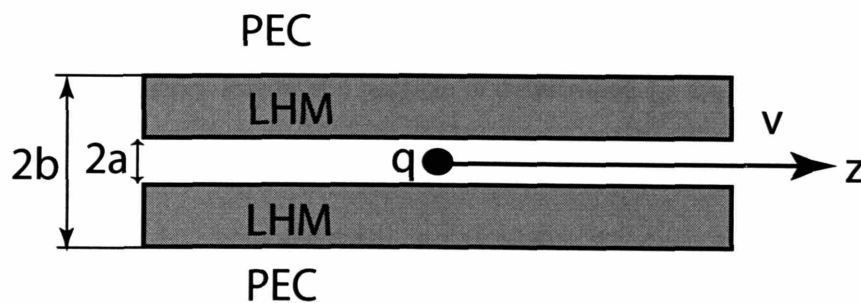
Figure 3-6: Region 1 is free space with $\epsilon_{1r} = 1$ and $\mu_{r1} = 1$, and is located in the center with a radius of a, where the particle can pass through. The LHM is in region 2 with $a < \rho < b$. The permittivity ϵ_{2r} and permeability μ_{2r} are given in Eqs. (3.17a) and (3.17b) respectively.

Since the strong frequency dispersion of LHM, two cases should be studied $n_2^2\beta^2 > 1$ and $n_2^2\beta^2 < 1$.

When $n_2^2\beta^2 > 1$, the radial component of the wave number is real, and the wave inside the LHM layer is propagating. The Green's functions are

$$g_1(\rho) = \frac{1}{2\pi}K_0(s_1\rho) + \alpha I_0(s_1\rho) \ \ \text{for} \ \ 0 \le \rho < a \ , \tag{3.20a}$$

$$g_2(\rho) = \xi N_0(k_{2\rho}\rho) + \zeta J_0(k_{2\rho}\rho) \ \ \text{for} \ \ a \le \rho < b \ . \tag{3.20b}$$

The coefficients are solved by matching the boundary condition at $\rho = a$ and $\rho = b$,

$$\alpha = \frac{1}{2\pi}\frac{p_{12}K_1(s_1a)p_0 - K_0(s_1a)q_0}{p_{12}I_1(s_1a)p_0 + I_0(s_1a)q_0} \tag{3.21a}$$

$$\xi = -\frac{1}{2\pi ak_{2\rho}}\frac{J_0(k_{2\rho}b)}{p_{12}I_1(s_1a)p_0 + I_0(s_1a)q_0} \tag{3.21b}$$

$$\zeta = \frac{1}{2\pi ak_{2\rho}}\frac{N_0(k_{2\rho}b)}{p_{12}I_1(s_1a)p_0 + I_0(s_1a)q_0} \tag{3.21c}$$

where $p_{12} = \frac{\epsilon_1 k_{2\rho}}{\epsilon_2 s_1}$, and

$$p_0 = J_0(k_{2\rho}b)N_0(k_{2\rho}a) - J_0(k_{2\rho}a)N_0(k_{2\rho}b) \ , \tag{3.22a}$$

$$q_0 = J_1(k_{2\rho}a)N_0(k_{2\rho}b) - J_0(k_{2\rho}b)N_1(k_{2\rho}a) \ . \tag{3.22b}$$

Similarly, the energy loss of the particle is determined by Eq. (3.6), and there is radiation only at the poles of α,

$$p_{12}I_1(s_1a)p_0 + I_0(s_1a)q_0 = 0 \ . \tag{3.23}$$

When $n_2^2\beta^2 < 1$, there are evanescent waves inside the LHM layer. The Green's functions for the LHM layer should be

$$g_2(\rho) = \xi K_0(s_2\rho) + \zeta I_0(s_2\rho) \ \ \text{for} \ \ a \le \rho < b \ . \tag{3.24}$$

58

The coefficients are solved as

$$\alpha = \frac{1}{2\pi} \frac{p_{12}K_1(s_1a)p_0 + K_0(s_1a)q_0}{p_{12}I_1(s_1a)p_0 - I_0(s_1a)q_0} \tag{3.25a}$$

$$\xi = -\frac{1}{2\pi a s_2} \frac{I_0(s_2b)}{p_{12}I_1(s_1a)p_0 - I_0(s_1a)q_0} \tag{3.25b}$$

$$\zeta = \frac{1}{2\pi a s_2} \frac{K_0(s_2b)}{p_{12}I_1(s_1a)p_0 - I_0(s_1a)q_0} \tag{3.25c}$$

where $p_{12} = \frac{\epsilon_1 s_2}{\epsilon_2 s_1}$, and

$$p_0 = I_0(s_2a)K_0(s_2b) - I_0(s_2b)K_0(s_2a) , \tag{3.26a}$$

$$q_0 = I_1(s_2a)K_0(s_2b) + I_0(s_2b)K_1(s_2a) . \tag{3.26b}$$

The pole is now determined by

$$p_{12}I_1(s_1a)p_0 - I_0(s_1a)q_0 = 0 . \tag{3.27}$$

In this case, there is no cutoff on the particle's velocity. No matter how slow the particle moves, there could be a surface plasmon excited. The existence of the surface plasmon is not only determined by the particle's velocity, but also by the radii a and b, as well as the dispersion of the LHM.

Again, when the loss is considered, Eqs. (3.23) and (3.27) can be used to find the approximate frequencies for the peaks of the radiation spectrum.

We applied the models in Eqs. (3.17a) and (3.17b) with the collision frequency $\gamma_e = \gamma_m = 10^9$ rad/s. The distribution of the radiated energy at different frequencies is plotted in Fig. 3-7.

The peak at 4.5 GHz is due to the LH behavior of the material, at which both the permittivity and permeability of LHM have negative real parts, and the wave is propagating dominantly inside the LHM layer with $\Re\{n_2^2\beta^2\} > 1$. When the collision frequencies is reduced, we have observed similar phenomenon as in Fig. 3-4, which is that the peaks are getting narrower, and more peaks are separated near the resonant frequency.

59
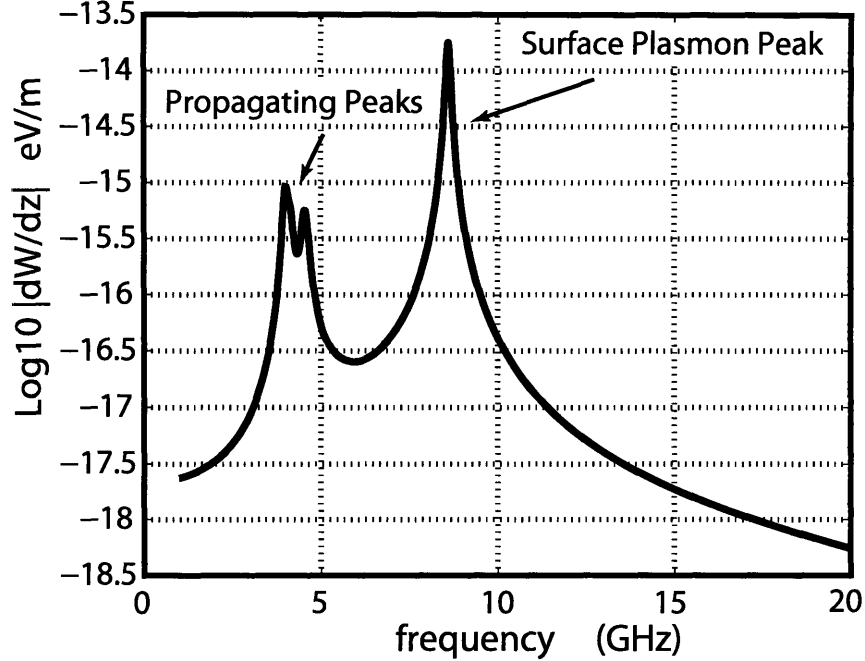
Figure 3-7: The energy loss distribution at different frequencies for a hole in the center of a waveguide filled with LHM. The collision frequency is $\gamma_e = \gamma_m = 10^9$ rad/s. The radii are $a = 0.5$cm, and $b = 1.5$cm. The thickness of LHM is kept as 1cm. These parameters were chosen according to a setup of an experiment for some RHM dielectrics [17].

The peak near 8.6 GHz, which is not present in Fig. 3-4, is due to the excitation of the surface plasmon at the boundary between the LHM and the vacuum, since the permittivity of the LHM has a negative real part while its permeability has a positive real part already. This surface plasmon peak is much stronger than those propagating peaks. The reason is that the imaginary parts of the permittivity and permeability are much smaller at the frequencies far from the resonant frequency, the argument is closer to the pole in Eq. (3.27) for the lossless case. This surface plasmon peak should be carefully distinguished from the expected propagating peaks, since this peak can be realized by a plasma, which is already a known phenomenon.

3.5   3-Layer problem

Although the channel in the center can allow the particle to pass without interacting with the dielectric material for clean Čerenkov radiation, the amplitude of the radiation is reduced due to the hole. It has been investigated that a plasma with a negative real part of the permittivity can amplify the radiation by the excitation of a surface plasmon. However, the plasma behavior of the natural material is mostly common in the optical frequency range. As will be shown here, this limitation can be overcome by an LHM, for which the properties are conserved by scaling the structure.

A three-layer problem shown in Fig. 3-8 is discussed here to investigate the ability of compensating the effect of the channel by a LHM.

We only consider an interesting case where

- Layer 1: $0 < \rho < a$, $\epsilon_{1r} = 1$, and $\mu_{1r} = 1$ $n_1^2\beta^2 < 1$;

- Layer 2: $a < \rho < b$, LHM;

- Layer 3: $b < \rho < \infty$, $\epsilon_{3r} > 0$, $\mu_{3r} > 0$, $n_3^2\beta^2 > 1$.
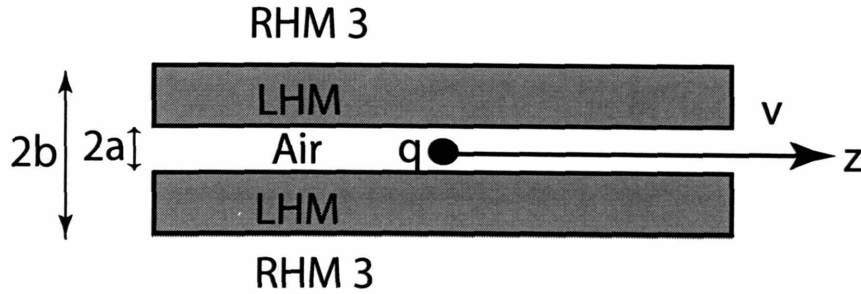
Figure 3-8: Similar to Fig. 3-6, with the PEC in the region $\rho > b$ replaced with a RHM.

The cases for both the propagating and evanescent waves should be considered. When $\Re(n_2^2\beta^2) > 1$, there is a propagating wave in layer 2. The Green's functions in

61

the 3 layers are written as

$$g_1(\rho) = \frac{1}{2\pi} K_0(s_1\rho) + \alpha I_0(s_1\rho) \qquad \text{for } 0 \le \rho < a , \qquad (3.28\text{a})$$

$$g_2(\rho) = \xi N_0(k_{2\rho}\rho) + \zeta J_0(k_{2\rho}\rho) \qquad \text{for } a \le \rho < b , \qquad (3.28\text{b})$$

$$g_3(\rho) = \eta H_0^{(1)}(k_{3\rho}\rho) \qquad \text{for } b \le \rho < \infty . \qquad (3.28\text{c})$$

The coefficient η is solved as

$$\eta = \frac{-1}{(\pi^2 k_{2\rho} k_{3\rho} ab)} \frac{1}{f_1 f_2 + f_3 f_4} , \qquad (3.29)$$

where

$$f_1 = p_{12} I_1(x_1) N_0(x_2) - I_0(x_1) N_1(x_2) , \qquad (3.30\text{a})$$

$$f_2 = p_{23} J_1(y_2) H_0^{(1)}(y_3) - J_0(y_2) H_1^1(y_3) , \qquad (3.30\text{b})$$

$$f_3 = p_{12} I_1(x_1) J_0(x_2) - I_0(x_1) J_1(x_2) , \qquad (3.30\text{c})$$

$$f_4 = -p_{23} N_1(y_2) H_0^{(1)}(y_3) + N_0(y_2) H_1^1(y_3) . \qquad (3.30\text{d})$$

The other coefficients can be obtained from η as follows

$$\xi = \frac{\pi}{2} k_{3\rho} b \left[p_{23} J_1(y_2) H_0^{(1)}(y_3) - J_0(y_2) H_1^{(1)}(y_3) \right] \eta , \qquad (3.31\text{a})$$

$$\zeta = \frac{\pi}{2} k_{3\rho} b \left[-p_{23} N_1(y_2) H_0^{(1)}(y_3) + N_0(y_2) H_1^{(1)}(y_3) \right] \eta , \qquad (3.31\text{b})$$

$$\alpha = \frac{1}{2\pi} \frac{K_1(x_1)}{I_1(x_1)} - \frac{k_{2\rho}}{s_1 I_1(x_1)} [\xi N_1(x_2) + \zeta J_1(x_2)] , \qquad (3.31\text{c})$$

where $s_1 = \sqrt{\frac{\omega^2}{v^2} - \omega^2 \mu_1 \epsilon_1}$, $k_{2\rho} = \sqrt{\frac{\omega^2 \mu_2 \epsilon_2 - \omega^2}{v^2}}$, $k_{3\rho} = \sqrt{\omega^2 \mu_3 \epsilon_3 - \frac{\omega^2}{v^2}}$, $x_1 = s_1 a$, $x_2 = k_{2\rho} a$, $y_2 = k_{2\rho} b$, $y_3 = k_{3\rho} b$, $p_{12} = \frac{k_{2\rho} \epsilon_1}{s_1 \epsilon_2}$, and $p_{23} = \frac{k_{3\rho} \epsilon_2}{k_{2\rho} \epsilon_3}$.

When $\Re(n_2^2 \beta^2) < 1$, the wave is evanescent inside the LHM layer, and the Green's function inside this region is

$$g_2(\rho) = \xi K_0(s_2\rho) + \zeta I_0(s_2\rho) \text{ for } a \le \rho < b . \qquad (3.32)$$

62

The energy Loss is given by Eq. (3.3) with the subscripts of the permittivity and permeability replaced with 3.

The coefficients are found as

$$\eta = \frac{-1}{2\pi s_2 k_{3\rho} ab} \frac{1}{f_1 f_2 + f_3 f_4} \, , \tag{3.33}$$

where

$$f_1 = p_{12} I_1(x_1) K_0(x_2) + I_0(x_1) K_1(x_2) \, , \tag{3.34a}$$

$$f_2 = p_{23} I_1(y_2) H_0^1(y_3) - I_0(y_2) H_1^{(1)}(y_3) \, , \tag{3.34b}$$

$$f_3 = p_{12} I_1(x_1) I_0(x_2) - I_0(x_1) I_1(x_2) \, , \tag{3.34c}$$

$$f_4 = p_{23} K_1(y_2) H_0^1(y_3) + K_0(y_2) H_1^{(1)}(y_3) \, . \tag{3.34d}$$

Similarly, other coefficients are found as follows

$$\xi = -k_{3\rho} b \left[p_{23} I_1(y_2) H_0^{(1)}(y_3) - I_0(y_2) H_1^{(1)}(y_3) \right] \eta \, , \tag{3.35a}$$

$$\zeta = -k_{3\rho} b \left[p_{23} K_1(y_2) H_0^{(1)}(y_3) + K_0(y_2) H_1^{(1)}(y_3) \right] \eta \, , \tag{3.35b}$$

$$\alpha = \frac{1}{2\pi} \frac{K_1(x_1)}{I_1(x_1)} + \frac{s_2}{s_1 I_1(x_1)} \left[-\xi K_1(x_2) + \zeta I_1(x_2) \right] \, , \tag{3.35c}$$

where $s_1 = \sqrt{\frac{\omega^2}{v^2} - \omega^2 \mu_1 \epsilon_1}$, $s_2 = \sqrt{\frac{\omega^2}{v^2} - \omega^2 \mu_2 \epsilon_2}$, $k_{3\rho} = \sqrt{\omega^2 \mu_3 \epsilon_3 - \frac{\omega^2}{v^2}}$, $x_1 = s_1 a$, $x_2 = s_2 a$, $y_2 = s_2 b$, $y_3 = k_{3\rho} b$, $p_{12} = \frac{\epsilon_1 s_2}{\epsilon_2 s_1}$, and $p_{23} = \frac{\epsilon_2 k_{3\rho}}{\epsilon_3 s_2}$.

The behavior of the terms in the denominator of η can be easily understood by using the asymptotic behavior of the modified Bessel function for large arguments. When a and b are large enough such that $s_1 a \gg 1$, $s_2 a \gg 1$, the denominator of η is dominated by f_2 which is approximately $e^{s_2 b}$. Combined with f_1, then the amplitude of η is proportional to $e^{-s_1 a - s_2(b-a)}$, which represents the wave decays in both layer 1 and 2, and therefore the radiation in the third layer is decreased as the radii a and b are increased even much more than for the first case in the two layer problems. However, we note that f_1 is the same as the denominator in Eqs. (3.5b), which means that when $f_1 = 0$, a surface plasmon is excited on the boundary between layers 1

and 2. The dominant term f_2 is canceled by f_1, and therefore when $f_1 = 0$, the second term of the denominator of η becomes dominant, whose asymptotic behavior is $f_3 f_4 \propto e^{s_1 a + s_2 a - s_2 b}$. η is then approximately proportional to $e^{-s_1 a + s_2(b-a)}$, which means that the surface plasmon compensates for the decaying of the wave in layer 1. Note that $\Re\{\epsilon_{2r}\} < 0$ is required for the existence of the surface plasmon.

In comparison with the case where $\Re\{n_2^2\beta\} > 1$, η decays approximately as $e^{-s_1 a}$ because there is no surface plasmon when the wave is propagating in layer 2. When there is no surface plasmon, the radiation is dominated by those frequencies where the wave is propagating inside the LHM layer, whereas the modes corresponding to the surface plasmon will dominate when the guidance condition is satisfied.

The above discussion is illustrated by the numerical examples. For simplicity, we first assume a non-dispersive LHM with $\epsilon_{2r} < 0$ and $\mu_{2r} < 0$ and being constants.
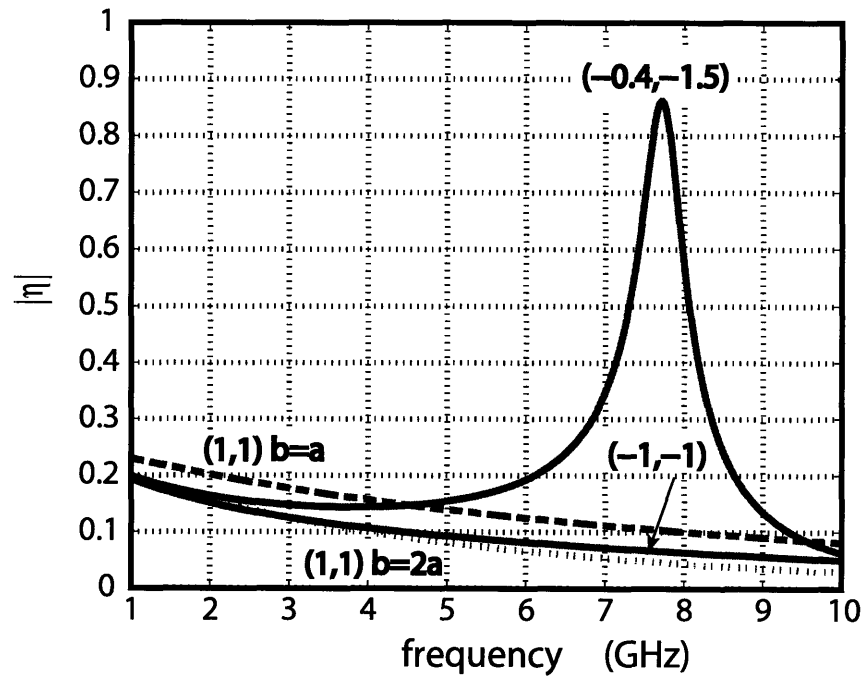
Figure 3-9: The amplitude of η when changing the constitutive parameters of the layer 2. The numbers inside the figure indicate the permittivity and permeability $(\epsilon_{2r}, \mu_{2r})$. The radii are $a = 1$cm $b = 2$cm. The velocity of the particle is $\beta = 0.9$.

Fig. 3-9 shows the distribution of the energy loss per unit length for different

combinations of permittivity and permeability satisfying $\epsilon_{2r}\mu_{2r}\beta^2 < 1$, which means the wave is evanescent inside layer 2. The radii are set to $a = 1$cm and $b = 2$cm, and the velocity of the particle is $\beta = 0.9$. In order for comparison, we first plot the case where layer 2 is free space also as the dotted line, which is equivalent to a larger channel with radius b. For the commonly discussed matched case where $(\epsilon_{2r}, \mu_{2r}) = (-1, -1)$, it is shown that the energy loss when the layer is a LHM is higher than that for a free space layer. This is because p_{12} is negative when layer 2 is a LHM and positive when layer 2 is a RHM, which means f_1 is in general smaller for a LHM than for a RHM, and will result in a higher value of the energy loss for a LHM. However, the amplitude is still less than the case where layer 2 is removed, and there is no amplification of the evanescent wave.
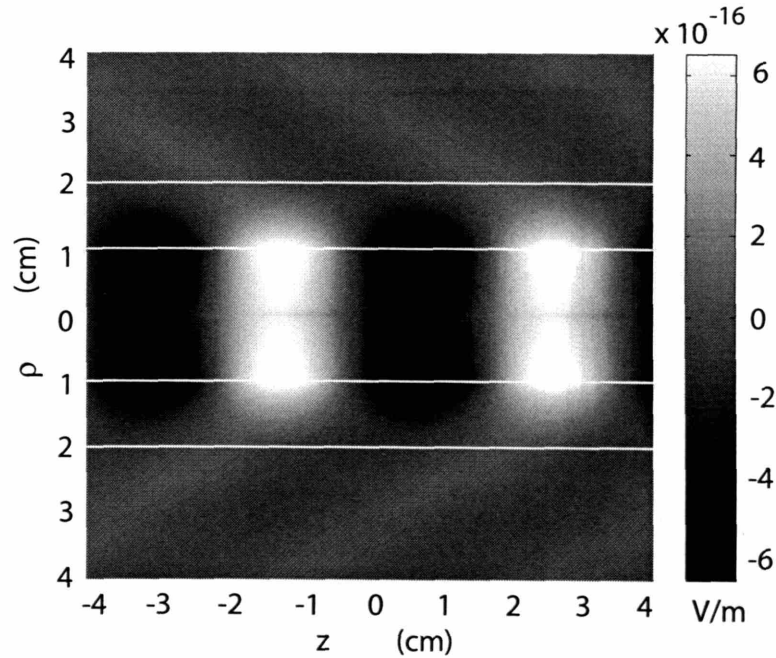
Figure 3-10: The real part of the longitudinal electric field E_z is plotted at 7GHz with $(\epsilon_{2r}, \mu_{2r} = (-0.4, -1.5))$. The radii are $a = 1$cm $b = 2$cm. The velocity of the particle is $\beta = 0.9$. The white lines at $\rho = 1$cm indicate the boundary between layers 1 and 2, and those at $\rho = 2$cm indicate the boundary between layers 2 and 3.

When $(\epsilon_{2r}, \mu_{2r}) = (-0.4, -1.5)$, a strong peak clearly appears in Fig. 3-9 at 7.7GHz, which indicates that a surface plasmon is excited, as illustrated in Fig. 3-

10. We have observed that $f_1 = 0$ at 7GHz corresponding to the surface plasmon, however the maximum of η is at 7.7GHz. The reason is that the second term of the denominator of η continues to decay after 7GHz, and the total denominator reaches a minimum at 7.7GHz.

Although the frequency of the surface plasmon is determined by the inner radius a, the maximum of η is affected by the outer radius b. For different b, the growth rate of f_2 is different, the larger the radius b, the faster f_2 grows, therefore, the less impact of the surface plasmon. As shown in Fig. 3-11, as the radius b increases, the frequency of the maximal η is closer to 7GHz, the frequency for the surface plasmon. The narrower bandwidth as b increases is due to the faster growth rate of f_2, and the radiation of those frequencies only in the very vicinity of 7GHz is amplified.
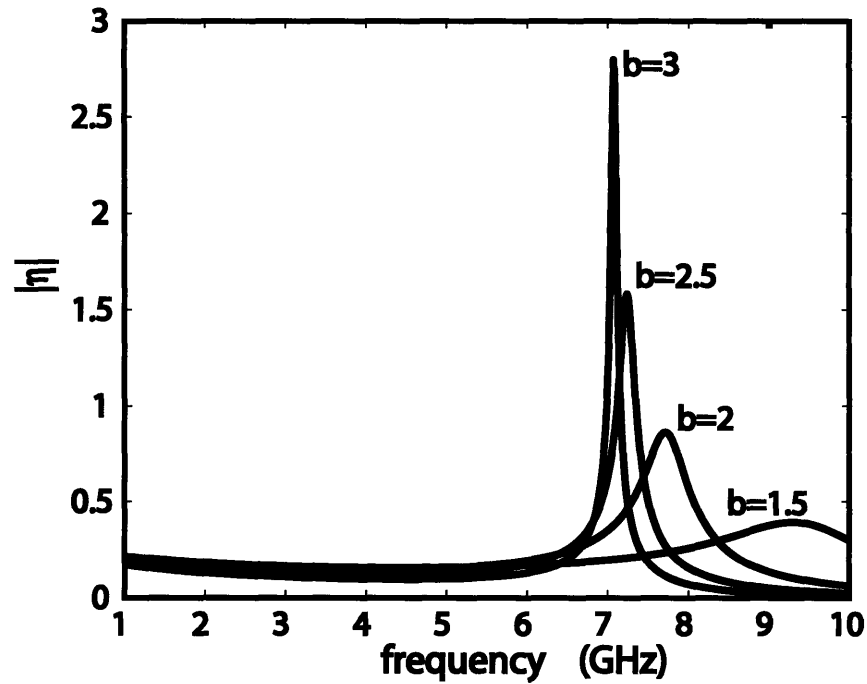
Figure 3-11: The amplitude of η when changing the radius b, which is indicated in the figure in units of cm. The permittivity and permeability are $\epsilon_{2r} = -0.4$, and $\mu_{2r} = -1.5$. The inner radius is $a = 1$cm.

66

When the dispersion and the loss of the LHM are considered, both the propagating and evanescent waves at different frequencies should be considered, and calculated with the formulations shown previously. The distribution of $|\eta|$ is plotted in Fig. 3-12. It is seen that η has both propagating peaks (ϵ_{2r} and μ_{2r} have negative real parts), and a surface plasmon peak (only the real part of ϵ_{2r} is negative). For different effective electron plasma frequencies, the position and the amplitude of the plasma peaks are different, which allows for more flexible applications. In Fig. 3-12(a), the surface plasmon peak is at around 8GHz, only when $\Re\{\epsilon_{2r}\} < 0$. The transverse wave number s_2 determines the amplitude and bandwidth of the peak, and the larger the s_2, the larger the amplitude, and the narrower the bandwidth. The surface plasmon peak in Fig. 3-12(a) is at a frequency higher than the zeros of the real part of the permeability around 6GHz, and therefore, $0 < \Re\{\mu_{2r}\} < 1$. When the effective electron plasma frequency is shifted lower than 6GHz, the plasma peak can be moved to frequencies lower than the resonant frequency of the permeability, as shown in Fig. 3-12(b).

In this case, the transverse wave number s_2 is much larger than that in Fig. 3-12(a), since the permeability has a large positive real part at this frequency. As a result, the surface plasmon peak has a higher amplitude in Fig. 3-12(b) than that in Fig. 3-12(a). This implies that in order to realize the same amplification effect, the case in Fig. 3-12(b) just needs a thinner layer of the material, a smaller $b - a$. The reason that the amplitude of the propagating peak is lower than that of the surface plasmon peak, is that the traverse wave number in the LHM frequency region is smaller than that of the plasma frequency region.
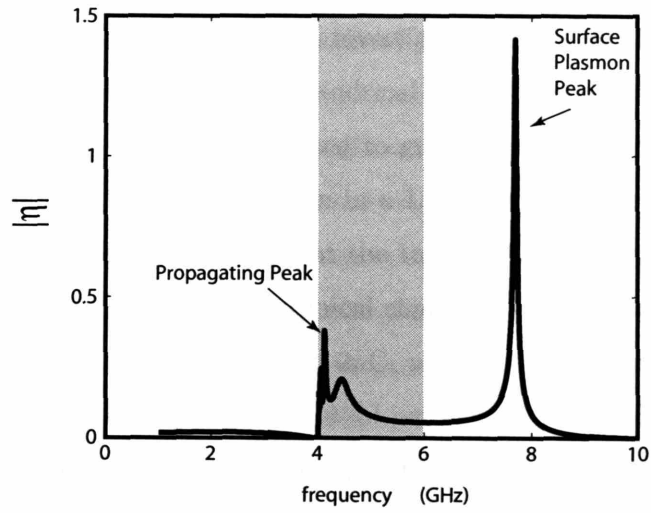
(a) $\omega_p = 2\pi \times 10^{10}$ rad/s
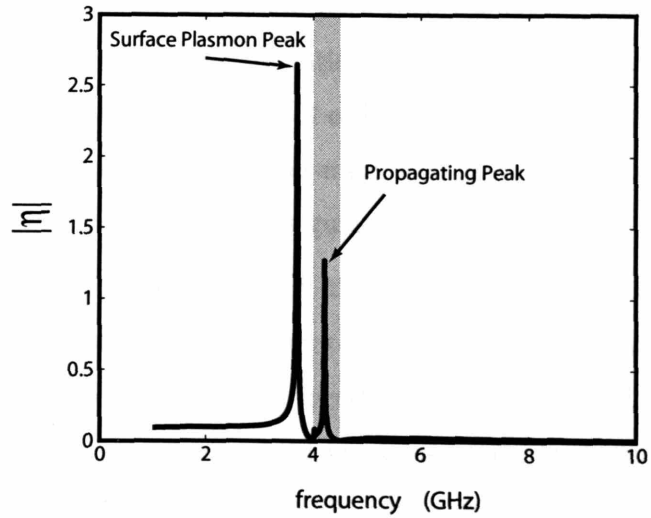
(b) $\omega_p = 2\pi \times 4.5 \times 10^9$ rad/s

Figure 3-12: The amplitude of η for different effective electron plasma frequencies of the model for the permittivity in Eq. (3.17a). The collision frequency is assumed to be $\gamma_e = \gamma_m = 10^7$rad/s in all the cases. The radii are $a = 1$cm and $b = 2$cm. The velocity of the particle is assumed to be $\beta = 0.9$. The shaded region indicates the frequency band for both ϵ_{2r} and μ_{2r} having negative real parts.

3.6 Conclusion

The behavior of the Čerenkov radiation is investigated thoroughly for a particle traveling along the axis of the multi layer cylindrical media involving a LHM. The cases with the metallic wave guided can be used to guide a possible experimental observation of the reversed Čerenkov radiation in a LHM. When there is no channel for the particle in the center, it is shown that the total radiated energy by one particle per unit length is about 10^{-6}eV. The typical charge for an electron bunch that can be realized by experiments [17] is about 2nC, which is equivalent to roughly 10^{10} electrons. The radiated energy is about 10^{-5}J per electron bunch for a waveguide of 1m length. The radiated power is on the order of 10μW if we only consider one bunch per second, and the total power should be higher if the multi bunches are considered, typically 10^{3} to 10^{6} bunches per second. For the LHM experiments at the microwave frequency range, a standard waveguide port with the corresponding wavelength is normally used as a receiver. The resolution can be -50dBm, which corresponds to 10nW. The radiated energy is at least 3 orders higher than the resolution. This is actually not surprising, since high power microwave beam can be generated through Čerenkov radiation in this kind of wave guide.

However, we should note that in all the above estimations, we assume all the particles in a bunch simultaneously generate the coherent radiation. In a real electron bunch, the electrons are not moving all together, instead, they will interact with each other, and the individual electron could be accelerated. Furthermore, if there is a focusing mechanism to confine the electron bunch, combined with the interactions, the electrons will oscillate. The non-uniform motion of electrons will result in large background radiation. Also, the electromagnetic field, which is used to confine the electron bunch, could be an important source of the noise which may be mixed with the signal.

According to the main purpose of this chapter, we just want to identify the new physics phenomena theoretically. In future studies along this topic, all of the above effects should be considered and compared with the amplitude of the real signal.

When the central channel is considered, the radiated energy is reduced by about an order of magnitude in the frequency range of [4.002,5.117]GHz. However, more importantly, a strong plasma peak will be present, which should be carefully distinguished in the experiment studies.

Finally, the 3-layer problem shows a possible application for our study. The central channel is good for avoiding the noise from the interactions between the charged particles and the atoms of the materials; however, the radiated energy is also decreased exponentially. This effect is much worse at higher frequencies, since the radius cannot be very small, and it could be already many wavelengths for the radiations in the optical frequencies, where the most detection was made. Adding a LHM layer can compensate and even amplify the radiation at the frequencies where the surface plasmon is excited. The narrow band of the amplification can be used to overcome the dispersion effect of the Čerenkov detection in the high energy application. To detect the velocity of the high energy charged unknown particles, the Čerenkov radiation is commonly used where the velocity can be determined from the angle of the radiation. However, the dispersion of the detector material, although small, can smear out the angle, which makes the detection less precise. The LHM layer can be used as a frequency selector with a very narrow band, which could be reduced by increasing the thickness of the LHM layer. Therefore, in the third medium, the detector material (some RHM with $n_3^2 \beta^2 > 1$) has a radiation peak only at the selected frequency, therefore overcoming the dispersion effect in the third medium.

It should be noted that only a negative real part of the permittivity is required for the existence of the surface plasmon, and therefore the electron plasma is enough, which has been theoretically and experimentally investigated. However, the combination with the dispersion of the permeability can offer more flexibility for the design of the instruments when a thinner or thicker thickness of the LHM layer can be chosen. Also the behavior of the permittivity and permeability of the LHM are scalable with the dimensions of the structure of the LHM, currently SRRs and rods. This scaling ability can allow the detection and application of the amplification effect at frequencies ranging almost from GHz to THz.

70

Chapter 4

Effect of the poles for a LHM slab

In this chapter, we will discuss two phenomena related to the singularities of electro-magnetic fields when a LHM slab is present.

4.1 Effect of Poles on the Sub-Wavelength Focusing by a LHM Slab

4.1.1 Introduction

Among all the phenomena in Vesalago's original paper [1], a LHM slab lens is probably the most popular topic. Pendry firstly raised the concept of a "Perfect Lens" in [18]: by using a LHM slab, for which the evanescent waves can be amplified and the sub-wavelength focusing can be realized, i.e. the field distribution at the source can be perfectly reproduced at the image point. A transfer function has been used to analyze the resolution abilities of LHM slabs for lossless [19] and lossy [20] cases. The results showed that the resolution is determined by the deviations from the real value of -1 in the relative permeability and permittivity, as well as the thickness of the slab.

Here we discuss this problem by directly calculating the electric and magnetic fields inside a slab of a LHM. We first show that there is an infinite number of poles in the complex k_z plane (the $\hat{z}$ component of wave vector k), and that a specific pole is located on the integral path of the field in all regions. We analyze the importance
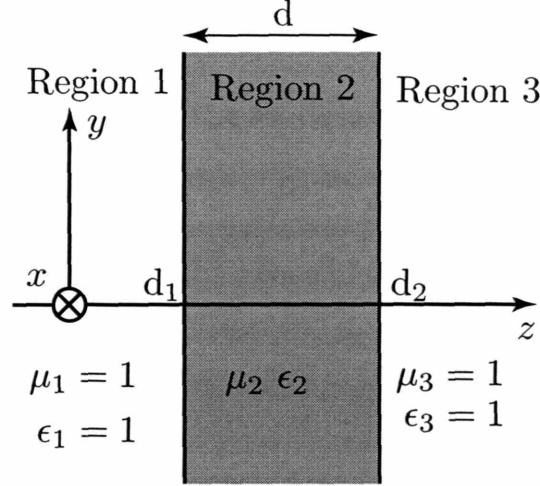
Figure 4-1: a LHM slab of thickness $d_2 - d_1 = d$ is located between $z = d_1$ and $z = d_2$.

of this specific pole, and its physical meaning.

4.1.2 Configurations of the problem

In this section we are considering the standard LHM lensing configuration as shown in Fig. 4-1. The permittivity ϵ_i and permeability μ_i for $i \in \{1, 2, 3\}$ shown here represent relative values. Region 1 and region 3 are free-space, with $\mu_1 = \mu_3 = 1$, and $\epsilon_1 = \epsilon_3 = 1$. a LHM slab is located in region 2 between $z = d_1$ and $z = d_2$, and is infinite in both $\hat{x}$ and $\hat{y}$ directions. In the examples discussed in this letter, $d_1 = \lambda/2$ and $d = d_2 - d_1 = \lambda$. The relative permeability and permittivity of the slab, μ_2 and ϵ_2, have real parts that may take negative values. The current and electric field are expressed in frequency domain, $\overline{\Theta}(\overline{r})$, which are related to the time domain quantities by $\overline{\Theta}(\overline{r}, t) = \Re\{\overline{\Theta}(\overline{r})e^{-i\omega t}\}$, where Θ represents current J or electric field E.

A line source is located at the origin, whose current can be expressed as:

$$\overline{J}(\overline{r}) = \hat{x}I\delta(y)\delta(z) . \tag{4.1}$$

Expressing the field in terms of a spectrum of TE waves, the electric field in each

region can be written as [12, 21]

$$E_{1+x} = \int_{-\infty}^{\infty} \left(e^{ik_{1z}z} + Re^{-ik_{1z}z} \right) E_{lin} \, e^{ik_y y} \, dk_y \ , \tag{4.2a}$$

$$E_{2x} = \int_{-\infty}^{\infty} \left(Ae^{ik_{2z}z} + Be^{-ik_{2z}z} \right) E_{lin} \, e^{ik_y y} \, dk_y \ , \tag{4.2b}$$

$$E_{3x} = \int_{-\infty}^{\infty} \left(Te^{ik_{3z}z} \right) E_{lin} \, e^{ik_y y} \, dk_y \ , \tag{4.2c}$$

where $E_{lin} = -\frac{\omega\mu_0\mu_1 I}{4\pi k_{1z}}$, k_{iz} is the $\hat{z}$ component of the wave vector, and 1^+ denotes the region $0 < z < d_1$. In Eqs. (4.2), R is the reflection coefficient, T is the transmission coefficient, and A, B are the coefficients of the forward and backward waves inside the slab. The magnetic field can be directly obtained from Maxwell's equations.

By matching the boundary conditions at $z = d_1$ and $z = d_2$, the coefficients can be obtained as in [12, 21],

$$T = \frac{4e^{ik_{1z}d_1} e^{ik_{2z}(d_2-d_1)} e^{-ik_{3z}d_2}}{(1+p_{12})(1+p_{23})(1+R_{12}R_{23}e^{i2k_{2z}(d_2-d_1)})} \ , \tag{4.3a}$$

$$A = \frac{2e^{-i(k_{2z}-k_{1z})d_1}}{(1+p_{12})(1+R_{12}R_{23}e^{i2k_{2z}(d_2-d_1)})} \ , \tag{4.3b}$$

$$B = \frac{2R_{23}e^{-i(k_{2z}-k_{1z})d_1} e^{i2k_{2z}d_2}}{(1+p_{12})(1+R_{12}R_{23}e^{i2k_{2z}(d_2-d_1)})} \ , \tag{4.3c}$$

$$R = e^{i2k_{1z}d_1} \frac{R_{12} + R_{23}e^{i2k_{2z}(d_2-d_1)}}{(1+R_{12}R_{23}e^{i2k_{2z}(d_2-d_1)})} \ . \tag{4.3d}$$

where

$$p_{12} = \frac{\mu_1 k_{2z}}{\mu_2 k_{1z}} \ , \tag{4.4a}$$

$$p_{23} = \frac{\mu_2 k_{3z}}{\mu_3 k_{2z}} \ , \tag{4.4b}$$

$$R_{12} = \frac{\mu_2 k_{1z} - \mu_1 k_{2z}}{\mu_2 k_{1z} + \mu_1 k_{2z}} \ , \tag{4.4c}$$

$$R_{23} = \frac{\mu_3 k_{2z} - \mu_2 k_{3z}}{\mu_3 k_{2z} + \mu_2 k_{3z}} \ . \tag{4.4d}$$

4.1.3 Analysis of the pole

An important property is that all the coefficients (R, A, B, and T) have a common denominator

$$1 + R_{12}R_{23}e^{i2k_{2z}(d_2-d_1)} \, , \tag{4.5}$$

which can be zero for some specific values of k_{2z}.

Due to the complexity of expression (4.5), it is not possible to find its roots analytically in most cases. However, we can analytically find the pole locations for a special case, in which the physical meaning of the pole is best illustrated. The special case starts by taking the following expressions of ϵ_2 and μ_2:

$$\mu_2 = -(1+\delta) \, , \quad \epsilon_2 = -\frac{1}{1+\delta} \, , \tag{4.6}$$

where δ is real and $0 < \delta \ll 1$. We choose this configuration in order to keep $k_1^2 = k_2^2 = k_3^2$.

Phase matching implies that $k_{1y} = k_{2y} = k_{3y} = k_y$ so that $k_z = k_{1z} = k_{3z} = \pm k_{2z}$.

It can be proven that the solutions of the electric field and magnetic field are identical whether we choose $+k_z$ or $-k_z$. According to the convention in [18], we shall choose $k_{2z} = -k_z$ in this section, which allows the local reflection coefficients to be simplified as,

$$R_{12} = \tfrac{\delta}{2+\delta} \quad \text{and} \quad R_{23} = -\tfrac{\delta}{2+\delta} \, .$$

We are interested in the behavior of an electromagnetic wave in region 3 where the focusing can be observed. Thus, we express the electric field in region 3 as

$$
\begin{aligned}
E_{3x} &= -\frac{\omega\mu_0\mu_1 I}{4\pi}\frac{8(1+\delta)}{(2+\delta)^2} \\
&\quad \times \int_0^{\infty} \frac{1}{k_z}\frac{e^{ik_z z}}{e^{ik_z 2d}-(\frac{\delta}{2+\delta})^2} \cos k_y y \; \mathrm{d}k_y \, .
\end{aligned}
\tag{4.7}
$$

The reason, that the integration range is from 0 to $+\infty$, is that we choose the origin at the source, therefore the integration is symmetric.

For this situation, the poles of the integrand are determined by

$$e^{ik_z 2d} - \left(\frac{\delta}{2+\delta}\right)^2 = 0 \ , \tag{4.8}$$

and in terms of k_z $k_z = \frac{m\pi}{d} + \frac{i}{d}\ln\left(\frac{2+\delta}{\delta}\right) \ , \tag{4.9}$

where m is an integer.

For the sake of comparison, we can calculate the poles associated with a material where both permittivity and permeability are positive (we call this material a Right Handed Material, RHM). To do this, we use $\mu_2 = 1 + \delta$, and $\epsilon_2 = \frac{1}{1+\delta}$, and follow the same procedure, as outlined before. We obtain,

$$e^{ik_z 2d} - \left(\frac{2+\delta}{\delta}\right)^2 = 0 \tag{4.10}$$

same as before $k_z = \frac{m\pi}{d} - \frac{i}{d}\ln\left(\frac{2+\delta}{\delta}\right) \ . \tag{4.11}$

We can directly see from Eqs. (4.9) and (4.11) that the poles of the LHM have a positive imaginary part, while those of the RHM have a negative imaginary part. This property is clearly visible in Fig. 4-2 in the k_z plane.
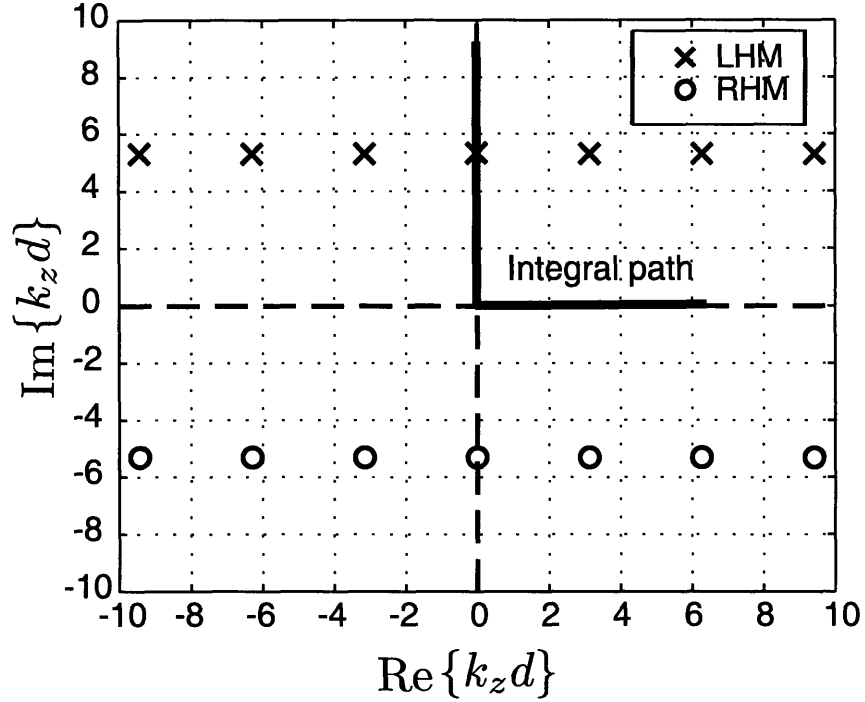
Figure 4-2: Poles for a LHM and a RHM in the k_z plane with $\delta = 0.01$.

The poles for the LHM are in the upper Riemann sheet in the k_z plane, whereas those for the RHM are in the lower Riemann sheet. The square root of the upper Riemann sheet satisfies the requirement that the evanescent waves should vanish at infinity, therefore the part of the integral path corresponding to $k_y > k$ in the k_y plane maps onto the imaginary axis $0i$ to $+\infty i$ in the k_z plane. In addition, the pole of the LHM with $m = 0$ lies exactly on the integration path of Eq. (4.7), and therefore its contribution to the total electric and magnetic fields must be accounted for.

From Eq. (4.9), we can define:

$$k_z^{max} = \frac{i}{d} \ln\left(\frac{2+\delta}{\delta}\right) , \tag{4.12}$$

where "max" means the maximum evanescent component that has a non-vanishing amplitude at the image point, which will be discussed later. The pole corresponds to a surface plasmon wave [18] on the two boundaries of the LHM slab, which is the

76

same as the guided mode with an imaginary transverse wave number in the LHM slab, which was indicated in [22].

Fig. 4-2 clearly shows that the integration path of Eqs. (4.2) passes through a LHM pole but not through an RHM pole (for which the imaginary part is negative). Therefore this proves that a LHM slab can support a surface plasmon wave while an RHM slab cannot. In addition, when $\delta \to 0$, the pole goes to infinity along the imaginary axis of k_z, which is consistent with Fig. 5 in [22], making the numerical evaluation of the integral increasingly difficult.
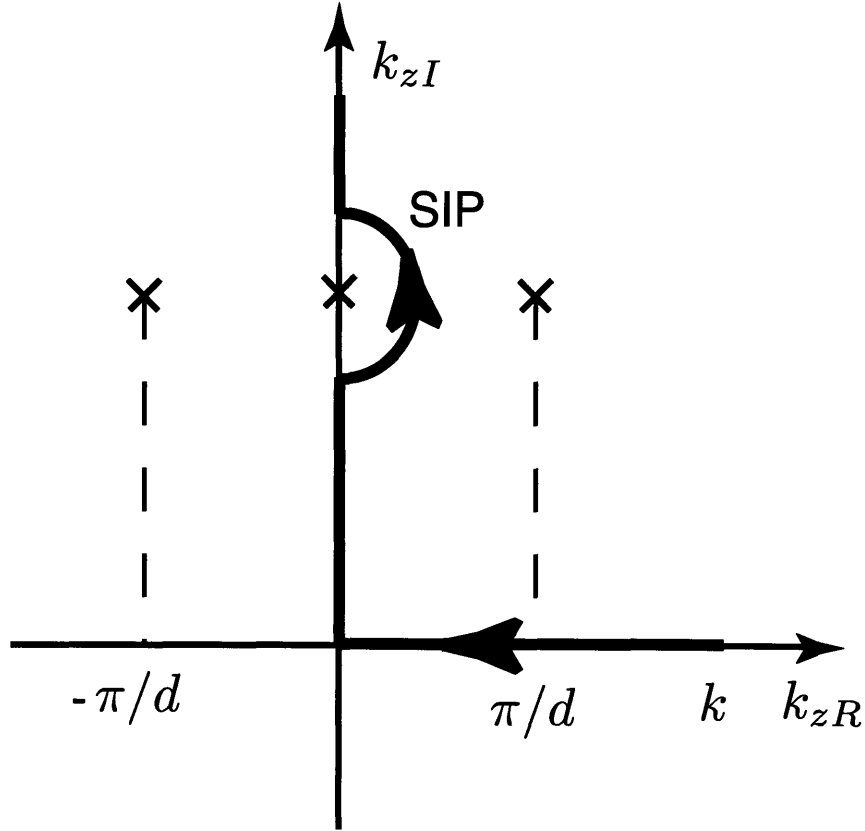
Figure 4-3: Definition of the Sommerfelt integral path (SIP) in the k_z plane.

In order to calculate the fields of Eqs. (4.2), we need to redefine the integration path into the Sommerfeld Integration Path (SIP), which is conveniently defined in the k_z plane, as shown in Fig. 4-3. The path passes the pole on its right-hand side because the pole would move to left if μ_2 and ϵ_2 had positive imaginary parts, i.e. if

the material was lossy. The fields can then be calculated by performing the numerical integration along the above defined SIP for any non-zero δ.

4.1.4 Effect of the pole on the focusing of a LHM slab

For the sake of illustration, we consider a line source located at the origin with a frequency $f = 1$ GHz. We choose $\delta = 10^{-3}$ so that the amplitude of the surface wave is not too high and dense compared to the regions other than the boundaries, and so that we can observe the periodicity of the surface plasmon at the boundary of the LHM slab and its effect on focusing at the image point [18] at $z = 0.6$ m, $y = 0$ m. If δ is smaller, the amplitude of the surface plasmon wave increases as the dielectric constants (μ_2, ϵ_2) approaches $(-1, -1)$, which will eventually make the field pattern not observable in those regions except for the boundaries.

The amplitude of E_x is shown in Fig. 4-4 for the three regions. As predicted, one can observe the surface wave at the two boundaries. The spatial period in $\hat{y}$ is found to be approximately 0.18 m, which is smaller than $\lambda = 0.3$ m.

If we consider the pole with $k_z = k_z^{max}$ of Eq. (4.12), the corresponding k_y is given by $k_y = \sqrt{k_2^2 - (k_z^{max})^2}$, and a spatial period in the $\hat{y}$ direction can be defined as

$$\lambda_y = \frac{2\pi}{\sqrt{k^2 + \frac{1}{d^2} \ln^2 \left(\frac{2+\delta}{\delta} \right)}} \ . \tag{4.13}$$

By plugging the numerical values given above into Eq. (4.13), we obtain $\lambda_y = 0.19$ m, which is very close to what we have empirically observed in Fig. 4-4. Therefore it confirms that the pole determines the surface mode at the boundaries between the RHM and the LHM.
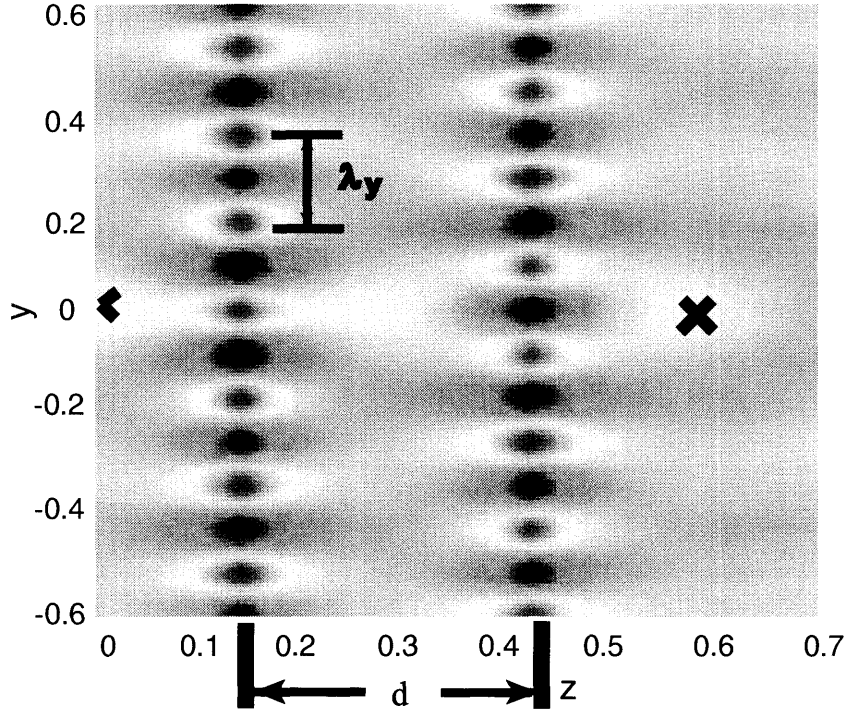
Figure 4-4: Amplitude of E_x with $\delta = 1 \times 10^{-3}$. The LHM slab is located between $d_1 = 0.15$ m and $d_2 = 0.45$ m. The Source is at $z = 0$, and the image is at $z = 0.6$ m.

Next, it is interesting to study the distribution of the amplitude of the fields inside the slab. Fig. 4-5 shows the amplitude of E_x in the three regions. We can see that the evanescent wave under k_y^{max} can be amplified inside the slab, and keeps a non-vanishing amplitude at the image plane, while the evanescent waves with $k_y > k_y^{max}$ cannot be amplified. Therefore only those evanescent waves with $k_y < k_y^{max}$ can contribute to the focusing at the image plane, hence limiting the resolution ability of the slab.
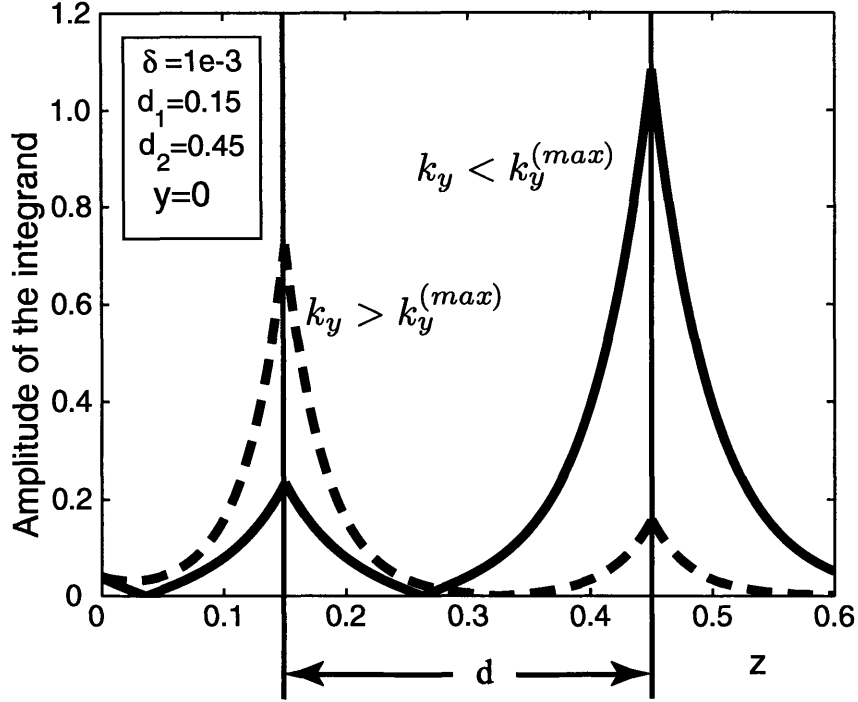
Figure 4-5: Amplitude of E_x for different plane wave components. The source is located at $z = 0$, and the image is at $z = 0.6$ m.

4.1.5 Effect of the pole on the resolution ability of the LHM slab

In order to further investigate the resolution ability of the LHM slab, we consider a screen with two slits located at $z = 0$, which, upon a plane wave incidence, can be modeled as two line sources. The separation between the two slits is δ_y, and we use the SIP defined in Fig. 4-3 to calculate the electric field E_x, magnetic field H_y, and the $\hat{z}$ component of the Poynting vector $S_z = E_x H_y^*$.

An interesting property of the LHM slab is its ability to resolve images with a separation smaller than the diffraction limit $\lambda/4$. To address this question, we purposely choose $\delta = 1 \times 10^{-13}$, such that $\lambda_y = 0.2\lambda < \lambda/4$ according to Eq. (4.13).

Of course, we can also tune the thickness of the slab d to achieve such a fine resolution, with a larger δ [19]. The concern here is that once the slab becomes

80

much thinner, the source has been put much closer to the first boundary accordingly, otherwise, the image at the other side of the slab cannot be achieved. However, technically, there is a limit of the distance between the source and the slab, which should be at least larger than the size of an atom. On the other hand, we can always tune the parameters of the LHM material, currently split ring resonators and metallic rods [2], to get the desired the dielectric constants (μ_2, ϵ_2).

When $\delta_y = \lambda_y = 0.2\lambda$, the amplitude of S_z is shown in Fig. 4-6(a). The solid curve shows $S_z = (E_x^{(1)} + E_x^{(2)})(H_y^{(1)} + H_y^{(2)})^*$ if we regard the two sources in coherent superposition, and the dashed curve shows $S_z = S_z^{(1)} + S_z^{(2)} = E_x^{(1)} H_y^{(1)*} + E_x^{(2)} H_y^{(2)*}$ if we regard the two sources in incoherent superposition. For this value of δ_y, the two peaks can be well resolved in both cases.

If we reduce the separation of the two slits to $\delta_y = 0.15\lambda < \lambda_y$, one can see from Fig. 4-6(b) that the two peaks of the incoherent case can be well resolved, while those for the coherent case are reaching a resolution limit, corroborating the conclusion that the resolution ability of the LHM slab is closely related to λ_y, which in turn is determined by the pole.

This phenomenon can be further explained by using the uncertainty principle of quantum theory. The uncertainty principle says that for a photon, the uncertainty of position Δy and uncertainty of momentum in that direction Δp_y satisfy

$$\Delta y \Delta p_y \leq h, \text{ from which we can get } \Delta y \leq \frac{2\pi}{\Delta k_y} \tag{4.14}$$

where $p_y = \hbar k_y$ for photons.

It is easy to understand that the smallest uncertainty of the position in $\hat{y}$ is determined by the available wave vectors of the plane wave components at the image plane. Since the evanescent waves decay in a RHM, only propagating plane waves contribute to the focusing at the image plane. Therefore the sub-wavelength resolution is only achievable in the near-field.

From Fig. 4-5 we see that the evanescent waves with $k_y < k_y^{max}$ can be amplified and transmitted to the far field image plane. The smallest uncertainty in $\hat{y}$ is then
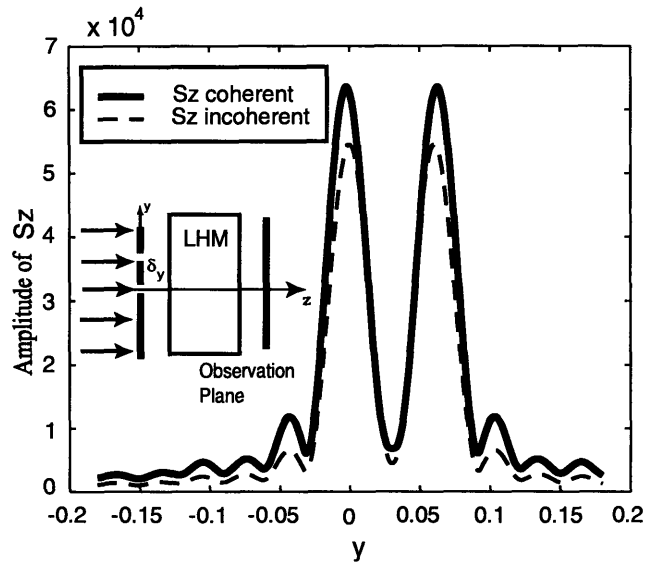
(a) Two sources are separated by $\delta_y = 0.2\,\lambda$.
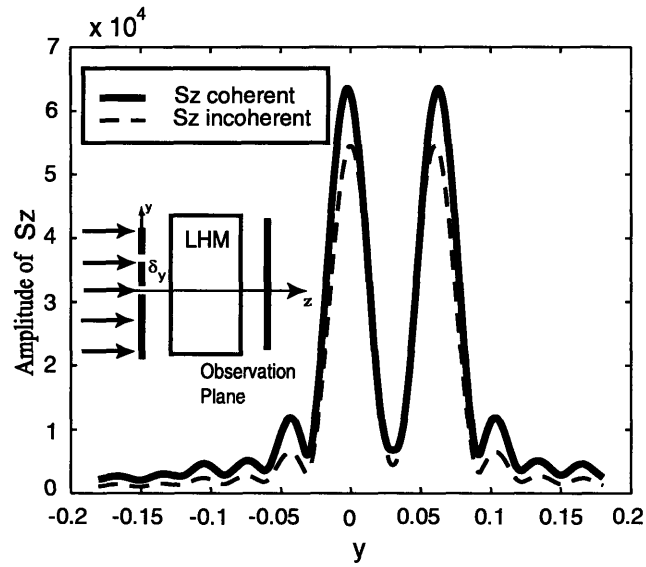
(b) Two sources are separated by $\delta_y = 0.15\,\lambda$.

Figure 4-6: Amplitude of S_z for coherent and incoherent superposition of the electromagnetic waves from the two sources, with $\delta = 1 \times 10^{-13}$ and $\lambda_y = 0.2\,\lambda$, for two separations between sources.

given by

$$\Delta y \leq \frac{2\pi}{\Delta k_y^{max}} = \lambda_y^{min} \ .$$

(4.15)

It can therefore be directly understood why the pole sets a limit on the resolution ability of the LHM slab. When $\delta \to 0$, the pole moves to infinity, and $\Delta k_y^{max} \to \infty$. This approaches the requirement of the "Perfect Lens", which requires that all evanescent waves be amplified and transmitted to the image plane. This is consistent with our analysis of the role of the pole on the transmission of the evanescent waves.

4.1.6 Conclusion

We can conclude that the pole lying on the integration path of the electric and magnetic fields in a LHM slab determines a special guided mode, which is an evanescent wave. In addition, this pole determines an upper limit below which the evanescent waves can be transmitted to realize sub-wavelength focusing at the far field image plane, thereby determining the resolution ability of the LHM slab. The special features of a LHM compared to a RHM are due to this pole, since its contribution has to be included into the field integrals of the LHM but not into those of the RHM.

4.2 Guided modes with a linearly varying transverse field inside a Left-Handed dielectric slab

4.2.1 Introduction

Guided waves are normally supported by a dielectric slab surrounded by a less dense media, where the fields decay at the infinities in the transverse directions. The fields inside the dielectric slab are normally described with exponential functions. Depending upon their transverse wave number k_x, the fields profiles can be described with trigonometric functions such as sines or cosines when k_x is real, or hyperbolic functions such as hyperbolic sine (sinh) or hyperbolic cosine (cosh) when k_x is imaginary. The trigonometric modes exist in normal materials where the real parts of both the

permittivity and permeability are positive [12, 23], while the hyperbolic modes can be supported by plasma media where the permittivity has a negative real part for TM waves [24, 25, 26, 27, 28, 29, 30, 31]. It is known that trigonometric and hyperbolic modes cannot coexist in either configuration. However they can coexist in left-handed materials (LHM) [1], where both the permittivity and permeability have negative real parts. Both types of guided modes were shown in [16, 22, 32] for symmetric configurations (where the regions on the two sides of the slab are identical), and in [33] for asymmetric configurations. The possible coexistence of these two types of modes is due to the fact that the poles corresponding to the hyperbolic modes lie in different Riemann sheets for a RHM (normal material in contrast with a LHM) and an LHM [34, 7]. In this section, a guided mode with a different profile, a linear function, is shown to exist when the transverse wave number $k_x = 0$ for a LHM slab with certain thickness [8]. From now on, we call this mode the linear mode. Physically, the trigonometric or hyperbolic modes can be understood as a superposition of two propagating, or two evanescent waves inside a slab. The coordinates $\bar{r}$ and time t of each of these waves appear in the form of $\bar{k} \cdot \bar{r} - \omega t$ through wave vector $\bar{k}$ and angular frequency ω, which is a direct extension of the solution for one-dimensional wave equation presented by Landau [35]. However, as will be shown in this section, this form does not hold in the transverse coordinate x for the linear mode.

4.2.2 Linear mode for asymmetric guided modes

The configuration is shown in Fig. 4-7. The permittivity ϵ_j and permeability μ_j of the three regions ($j \in \{1, 2, 3\}$) represent relative values and are taken to be real. Without loss of generality, regions 1 and 3 are assumed to be a RHM, but not necessarily identical; region 2 is assumed to be an LHM, where μ_2 and ϵ_2 may have negative real parts. In the case of TE modes (TM modes can be studied similarly), the non-zero fields are E_{jy}, H_{jx}, and H_{jz}. We assume a time dependence of $e^{-i\omega t}$
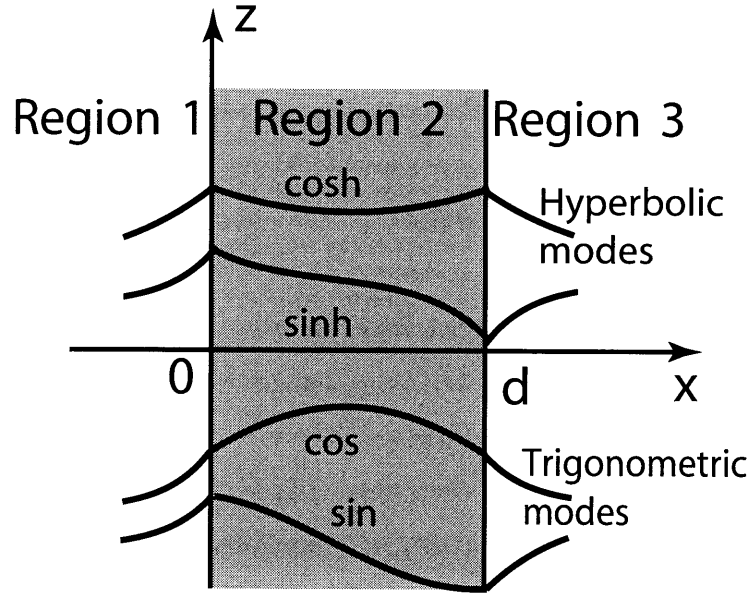
Figure 4-7: A dielectric slab is located between $x = 0$ and $x = d$. The shaded region represents a dielectric slab which extends to infinity in the $\hat{y}$ and $\hat{z}$ directions. The sketched curves show the known profiles of hyperbolic and trigonometric modes.

throughout this paper, and the electric fields in the three regions can be written as:

$$E_{1y} = e^{\alpha_1 x} e^{ik_z z} \qquad\qquad \text{for } x < 0 \,, \qquad\qquad (4.16a)$$

$$E_{2y} = (A e^{ik_{2x} x} + B e^{-ik_{2x} x}) e^{ik_z z} \qquad \text{for } 0 < x < d \,, \qquad (4.16b)$$

$$E_{3y} = T e^{-\alpha_3 x} e^{ik_z z} \qquad\qquad \text{for } x > d \,, \qquad\qquad (4.16c)$$

where $k_{2x} = \sqrt{k_0^2 \epsilon_2 \mu_2 - k_z^2}$, k_0 is the wave number in free space, and $\alpha_{1,3} = \sqrt{k_z^2 - k_0^2 \epsilon_{1,3} \mu_{1,3}}$ are positive to ensure a decay of the electric field as $x \to \pm\infty$. The electric fields in regions 2 and 3 are normalized to that in region 1, and the magnetic fields are obtained from Faraday's law accordingly. By matching the boundary conditions at $x = 0$ and $x = d$ for the tangential components of the electric and magnetic fields, the coefficients A, B, and T are obtained as follows:

85

$$A = \frac{1}{2} - \frac{i}{2} \frac{\mu_2 \alpha_1}{\mu_1 k_{2x}} , \quad B = \frac{1}{2} + \frac{i}{2} \frac{\mu_2 \alpha_1}{\mu_1 k_{2x}} , \tag{4.17a}$$

$$T_1 = e^{-\alpha_3 d} [\frac{1}{2} (e^{ik_{2x}d} + e^{-ik_{2x}d})$$
$$- \frac{i}{2} \frac{\mu_2 \alpha_1}{\mu_1 k_{2x}} (e^{ik_{2x}d} - e^{-ik_{2x}d})] , \tag{4.17b}$$

$$T_2 = e^{-\alpha_3 d} [\frac{1}{2} \frac{\mu_3 k_{2x}}{i \mu_2 \alpha_3} (e^{ik_{2x}d} - e^{-ik_{2x}d})$$
$$- \frac{1}{2} \frac{\mu_3 \alpha_1}{\mu_1 \alpha_3} (e^{ik_{2x}d} + e^{-ik_{2x}d})] . \tag{4.17c}$$

The coefficients T_1 and T_2 represent the transmission coefficient T but are obtained from matching the tangential electric and magnetic fields at $x = d$, respectively. The guidance condition for $k_{2x} \neq 0$ can be obtained by letting $T_1 = T_2$ and yields

$$e^{2ik_{2x}d} = \frac{(i\alpha_1 \mu_2 + k_{2x} \mu_1)(i\alpha_3 \mu_2 + k_{2x} \mu_3)}{(i\alpha_1 \mu_2 - k_{2x} \mu_1)(i\alpha_3 \mu_2 - k_{2x} \mu_3)} . \tag{4.18}$$

The guided modes can be found numerically by sweeping k_z and finding the values which satisfy Eq. (4.18).

Because of the singularity in the second term of Eq. (4.17b) when $k_{2x} = 0$, the guidance condition for this mode has to be obtained by taking the limit of Eqs. (4.17b) and (4.17c) as $k_{2x} \rightarrow 0$:

$$1 + \frac{\mu_2 \alpha_1 d}{\mu_1} = -\frac{\mu_3 \alpha_1}{\mu_1 \alpha_3} . \tag{4.19}$$

The thickness d for this linear mode is

$$d = -\frac{\mu_1 \alpha_3 + \mu_3 \alpha_1}{\mu_2 \alpha_1 \alpha_3} = -\frac{\mu_1 \sqrt{n_2^2 - n_1^2} + \mu_3 \sqrt{n_2^2 - n_3^2}}{2\pi \mu_2 \sqrt{n_2^2 - n_1^2} \sqrt{n_2^2 - n_3^2}} \lambda_0 , \tag{4.20}$$

where $n_j^2 = \epsilon_j \mu_j$. Contrary to the normal process of determining the tangential wave number for a given thickness d, the process is reversed here so that we have to find the thickness d knowing the tangential wave number $k_z = k_2$ (for $k_{2x} = 0$). The thickness d must be real and positive, which determines the existence of the guided mode at $k_{2x} = 0$. It immediately follows from Eq. (4.20) that a physical guided linear mode

can be supported in LHM slabs, while a slab of RHM leads to a non-physical guided mode where the field grows outside the slab (α_1 and/or α_3 are negative in this case). This is due to the fact that the poles corresponding to the hyperbolic modes of the RHM lie in the lower Riemann sheet, which correspond to non-physical modes, while those of LHM lie in the upper Riemann sheet, which correspond to physically guided modes [34, 7].

From the thickness of the slab d in Eq. (4.20), we can find the fields in region 2. Coefficients A and B are singular when $k_{2x} = 0$, which suggests that expressing the field profile as exponential functions is not ideal for this mode. The new basis functions are obtained by reorganizing the terms to cancel the singularity, and yields trigonometric functions for k_{2x} real ($k_z < k_2$) and hyperbolic functions for k_{2x} imaginary ($k_z > k_2$). Taking the limit as $k_{2x} \to 0$, the field expressions in region 2 can be written as follows,

$$E_{2y} = \left(1 + \frac{\mu_2}{\mu_1} \alpha_1 x \right) e^{ik_2 z} e^{-i\omega t} , \tag{4.21a}$$

$$H_{2z} = -\frac{i\alpha_1}{\omega\mu_1} e^{ik_2 z} e^{-i\omega t} , \tag{4.21b}$$

$$H_{2x} = -\frac{k_2}{\omega\mu_2} \left(1 + \frac{\mu_2}{\mu_1} \alpha_1 x \right) e^{ik_2 z} e^{-i\omega t} . \tag{4.21c}$$

Note that the above expressions can also be obtained by writing the fields in the slab directly as linear functions based on the approximation $e^{\pm ik_{2x}x} \approx 1 \pm ik_{2x}x$ when $k_{2x} \approx 0$. The transmission coefficient T for the field in region 3 is $1 + \frac{\mu_2\alpha_1 d}{\mu_1}$, with which the field in region 3 can be written accordingly.

Observing the solution in Eq. (4.21a), the space and time coordinates do not obey a form of $\overline{k} \cdot \overline{r} - \omega t$ like other trigonometric or hyperbolic modes. The profile function along $\hat{x}$ is therefore not a harmonic function. Instead, the electric field in the transverse direction is a linear function of x as shown in Eq. (4.21a), and the longitudinal magnetic field is a constant as shown in Eq. (4.21b). However, both fields satisfy the Maxwell equations.

Also,the linear solution of the wave function can only exist in a bounded region, for example inside a slab, since the electric field grows linearly to infinity as the coordinate $x \rightarrow \infty$.

A numerical example is used to demonstrate the existence of the linear mode. The constitutive parameters are chosen as (ϵ_1,μ_1)=(1,1), (ϵ_2,μ_2)=(-1,-4), and (ϵ_3,μ_3)=(1,2), the frequency is set at 10 GHz, and the thickness of the slab calculated from Eq. (4.20) is $0.792\lambda_0$. The corresponding tangential electric and magnetic fields distributions at $k_{2x} = 0$ are shown in Fig. 4-8, where both plots show the existence of a surface wave. A better match between media 2 and 3 causes the field at the second boundary to have a larger amplitude than that of the fields at the first boundary. The one-dimensional plots of the fields at $z = 0$ shown in Fig. 4-9 illustrate the linearity of the electric field, and the constant longitudinal magnetic field H_{2z} across the slab.

Upon using the same example, the values of the longitudinal wave vector k_z for the guided mode are plotted against the thickness of the slab in Fig. 4-10. The dashed line indicates the position $k_z = k_2$, which corresponds to $k_{2x} = 0$. By observing the evolution of the modes, we can find that this linear mode is a transitional mode between the sine and the sinh modes in terms of the transverse electric field E_y for TE modes. For this configuration, there is only one anti-symmetric mode since the slab is very thin. As the thickness of the slab increases, the higher order symmetric and anti-symmetric trigonometric modes appear. The modes with $k_z > k_2$ are hyperbolic with sinh functions as profiles as illustrated in the insets of Fig. 4-10, while the modes with $k_z < k_2$ are trigonometric with sine functions as profiles. It was mentioned in [16] that $k_z = k_2$ is the turning point between trigonometric and hyperbolic modes, but the existence of the mode was not shown. The linear mode shown here confirms that it serves as a transitional mode between the sinh and sine profiles. The modes presented in Fig. 4-10 are all anti-symmetric. The sine function and sinh function have opposite signs of convexities in the same side of the null point. As k_z approaches k_2, the slope of the profile approaches that of the linear mode, at which the convexity is 0. Then, the convexity changes as k_z deviates from k_2. In terms of the transverse wave number, $k_{2x} = 0$ at $k_z = k_2$ is the only possible transition point between real and
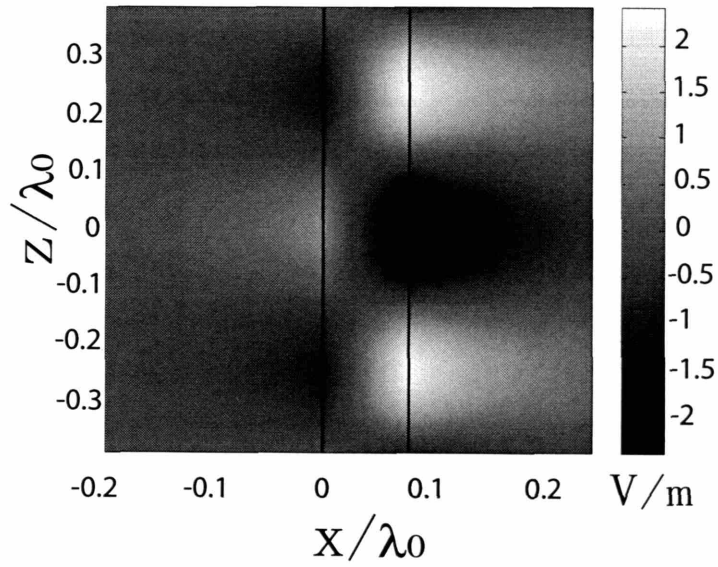
(a) E_y
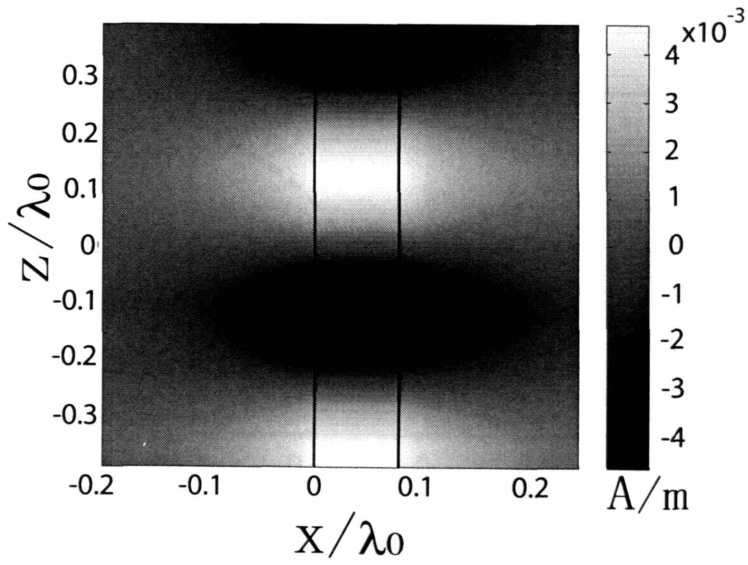
(b) H_z

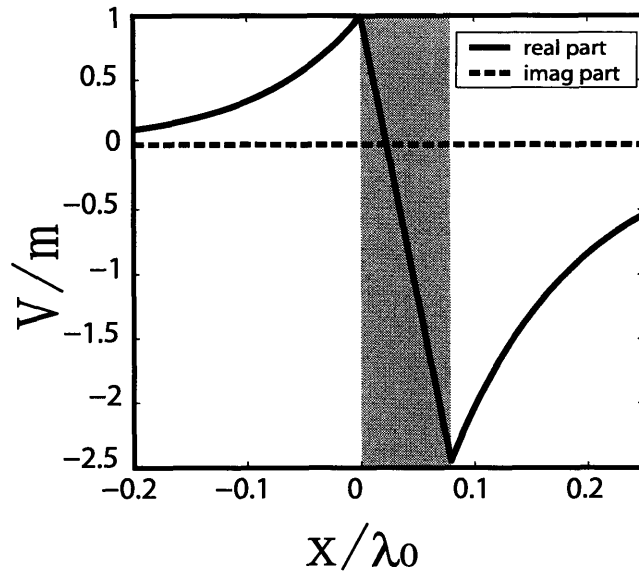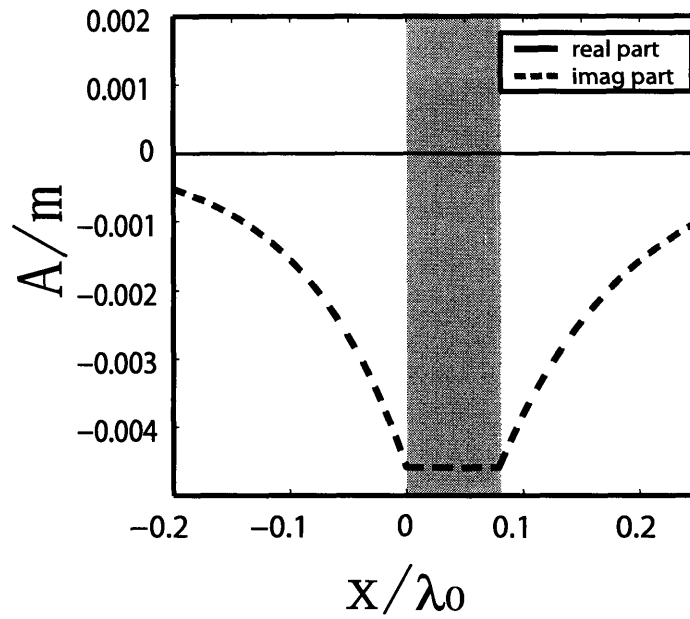Figure 4-8: Distribution of the real parts of the electric (a) and magnetic (b) fields for the mode $k_z = k_2$, $(\epsilon_1, \mu_1) = (1,1)$, $(\epsilon_2, \mu_2) = (-1, -4)$, and $(\epsilon_3, \mu_3) = (1,2)$.

(a) E_y

(b) H_z

Figure 4-9: Distribution of the electric (a) and magnetic (b) fields for the mode $k_z = k_2$ at $z = 0$. It can be noted that E_y and H_z have a $\pi/2$ phase difference.
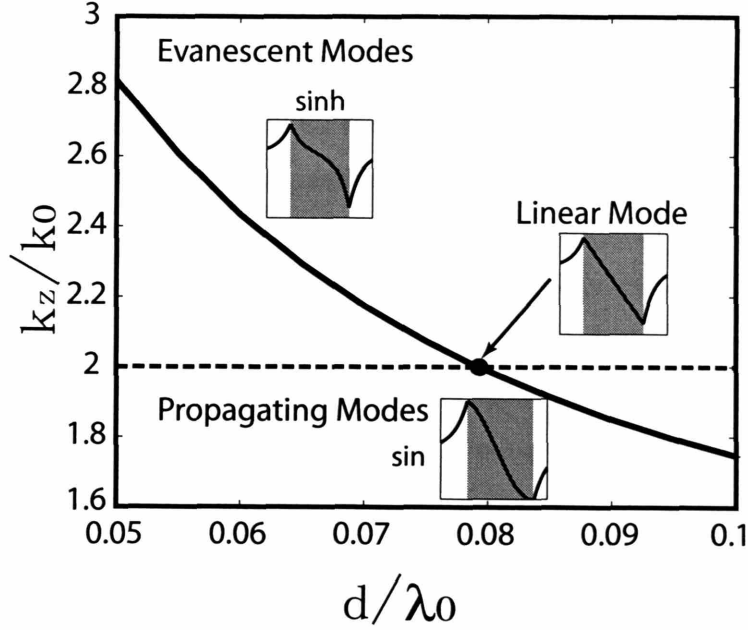
Figure 4-10: Evolution of the guided modes according to the thickness of the slab for the configuration $(\epsilon_1,\mu_1)=(1,1)$, $(\epsilon_2,\mu_2)=(-1,-4)$, $(\epsilon_3,\mu_3)=(1,2)$.

imaginary values of k_{2x}, which corresponds to trigonometric and hyperbolic modes, respectively.

4.2.3   Linear mode for symmetric guided modes

It is equally important to examine whether the transitional mode also exists for symmetric modes between cosh and cosine functions. In general, this mode does not exist in both a RHM and a LHM. Mathematically it can be seen directly from the field solution of Eqs. (4.21): the only possible transitional function between cosh and cosine modes is a constant, which corresponds to a constant electric field and $\alpha_1 = 0$. Therefore, the transitional mode for symmetric modes cannot exist for arbitrary configurations but only for the special case where $k_1^2 = k_2^2 = k_3^2$. The electric fields $E_y = e^{ik_2z}$ are identical in the three regions, and have no variation along the transverse $\hat{x}$ direction, which yield magnetic fields with zero $\hat{z}$ component, and constant $\hat{x}$ component. Consequently this corresponds to a TEM mode.

91

The absence of the symmetric transitional mode for general cases can be understood by noting the two lowest propagating modes which have a cutoff: TE1 is the lowest anti-symmetric mode, and TE2 is the lowest symmetric mode. Since the profile for the TE2 mode is a cosine function but with more than one period variation inside the slab, it cannot be a transition between the cosh and the cosine functions. In addition, the transition between the cosh and the sine functions is also not possible because of their different symmetries. In order to break the symmetry, the only possible solution is for the field at one boundary to be zero, which is not a physical nontrivial solution. Hence, the only possible transitional mode for symmetric modes is the TEM mode studied in this section.

4.2.4 Conclusion

In conclusion, a unique linear physical guided mode is presented for $k_{2x} = 0$ in a LHM slab with very special properties. The linear profile in the transverse direction of the mode serves as a smooth transition between the sine modes and sinh modes. The properties of this unique linear mode are discussed and illustrated by the numerical examples. The constant longitudinal magnetic field for TE modes, and electric field for TM modes can offer more degrees of freedom in designing planar wave guides for various applications.

Chapter 5

Novel LH meta-material design for Traveling Line Current Source

5.1 Introduction

In previous chapters, we have assumed an ideal homogeneous isotropic Left-Handed material whose permeability and permittivity were modeled by Lorentz and Drude models. In order for the possible experimental demonstration of the previous theoretical conclusions, we need to have a design which can realize backward Čerenkov radiation.

As already known by the researchers, that there is no natural material simultaneously exhibiting negative permittivity and permeability. However, we know that small resonators, such as split ring resonators (SRR) can have a strong response to the incident magnetic field, which can result in a negative permeability in a narrow band higher than the resonant frequency [3]. The negative permittivity is actually more popular since many metals, for example bulk silver, behave as a plasma in the optical frequency range, whose permittivity is negative in the range below the plasma frequency. Pendry [4] have proposed that when an electric field acts along the arrays of thin metal wires, the effective electron mass can be increased by several orders, which lowers the plasma frequency to GHz. Therefore, the effective negative permittivity can be realized in the microwave frequency band. It is further demonstrated by

the experiment [2] that the effective negative permittivity and permeability can be simultaneously realized in the GHz frequency range. The concepts of split ring resonators and thin metal wire were widely adopted, and various structures [36, 37, 38] were proposed and verified by both simulations and experiments.

However, the basic feature of Čerenkov radiation, TM wave, prevents us to use these existing designs. The reason can be explained by reviewing each of the available 4 designs.

To realize backward Čerenkov radiation, the minimum requirement of the dielectric constants are

$$\epsilon_r = \begin{pmatrix} - & 0 & 0 \\ 0 & - & 0 \\ 0 & 0 & + \end{pmatrix} \tag{5.1a}$$

$$\mu_r = \begin{pmatrix} + & 0 & 0 \\ 0 & + & 0 \\ 0 & 0 & - \end{pmatrix} \tag{5.1b}$$

where we assumed that the charged particles move along $\hat{x}$ direction. The dielectric constant matrices indicate that we need the split ring with its normal in the $\hat{z}$ direction, and thin metal wires in the $\hat{x}$ and $\hat{y}$ directions. However, all of the previously realized structures are for TE incidence waves, which satisfy

$$\epsilon_r = \begin{pmatrix} + & 0 & 0 \\ 0 & + & 0 \\ 0 & 0 & - \end{pmatrix} \tag{5.2a}$$

$$\mu_r = \begin{pmatrix} - & 0 & 0 \\ 0 & - & 0 \\ 0 & 0 & + \end{pmatrix} \tag{5.2b}$$

where the two negative elements of μ_r were realized by arranging the rings in two

directions.

The first LHM design is the split ring resonators as proposed in [3] in combination with the thin metal wire [4], as shown in Fig. 5-1. It was reported in [39] that this structure has bianisotropy, which means the electric and magnetic responses can affect each other as the incidence polarization changes, and a non-zero off-diagonal element appears. This will complicate the calculations, and is not suitable for experiment.
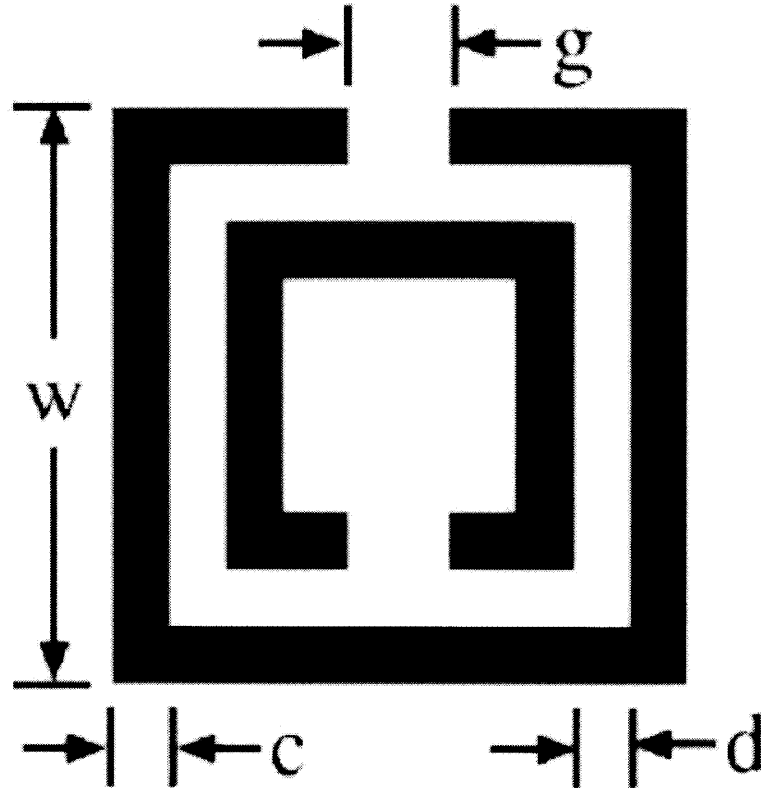
Figure 5-1: The split ring resonators as realized in [2]. The parameters are taken as the same in [2], where c=0.25mm, d=0.30mm, w=2.62mm, g=0.46mm, and a=5mm.

Another ring was first proposed for the near infra red frequency range in [36], and was scaled to GHz frequency range [40] as shown in Fig. 5-2. This ring lacks the symmetry of the plane in which the ring is located.

These split ring resonators can be modeled by a lumped capacitance and induc-
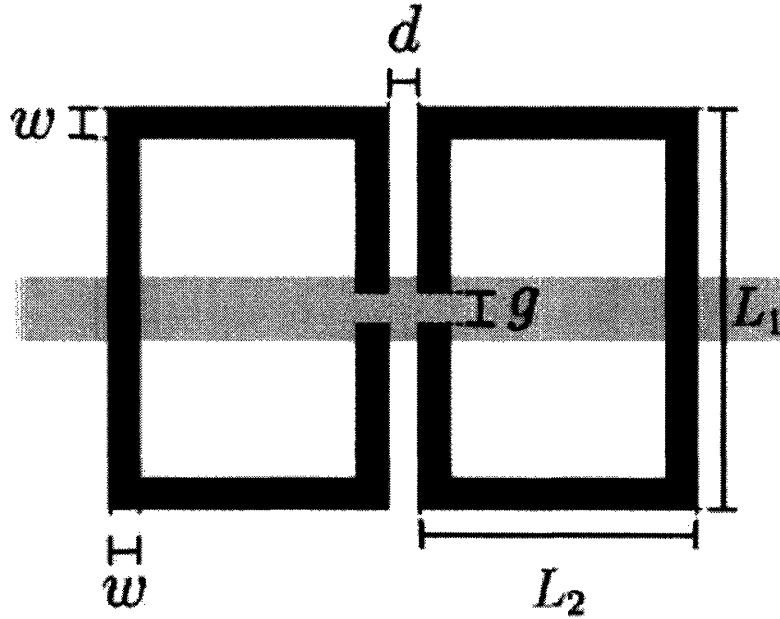
Figure 5-2: The second split ring resonator in [40]. The parameters are taken as the same in the paper, where w = g = d = 0.24 mm, L = 3.12 mm, and L = 2.16 mm. The lattice constant is 5.04mm in the propagation direction, and (6mm × 6mm) in the lateral directions. The rod (light gray) has a width of 0.5 mm and is 1 mm away from the ring.

tance. The capacitance of these two rings is due to the electric displacement field vector between the edges of the inner and outer rings for the first ring, and between the edges of the two single rings for the second ring. Therefore, these rings are also called edge coupled rings [39].

Another type of ring is called side coupled ring, which is represented by Ω-ring and S-ring as in Figs. 5-3 and 5-4, respectively. The metallic strips are printed on both sides. The capacitance of the resonator is due to the sides of the front and back rings. One feature of these two types of LH metamaterials is that metallic rods and the rings are together, not like the first two designs, in which the rings and rods are separated.

Although all of these four designs have been verified by experiments using TE wave incidence, they cannot easily be modified for use in TM wave incidence. The
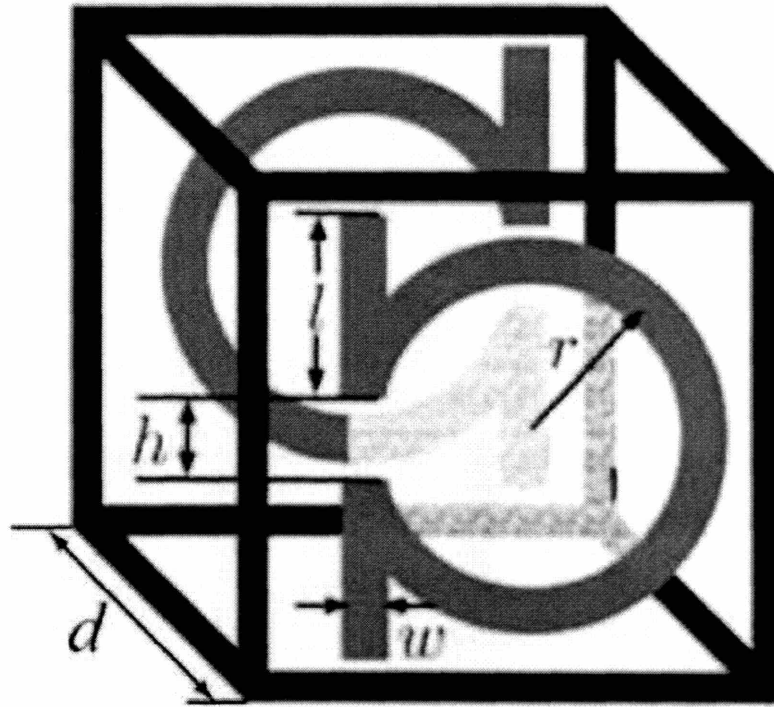
Figure 5-3: The Ω-ring resonator in [37]. The parameters are taken as the same in the paper, where r=1.5mm, w=0.4mm, h=0.2mm, l=2mm, and d=4mm. The permittivity for the dielectric board is 1.5.

first two designs have a rod-touching problem in the experiments, which requires the metallic rods touch the top and bottom sides of the waveguide to make the rods effectively infinitely long. If not, the rods will be finite, and will not behave as a plasma, instead the permittivity will have a resonance shape. But due to the limitations of the dimensions, the resonant frequency of the permittivity is normally much higher than that of the permeability due to the resonance of the rings. The resonant frequency of the permittivity will go down as the length of the rods increase, and therefore the unit cells for the rings are different from that of the rods, which is not good for isotropy. The other two rings overcame this problem by making the rings and rods together, such that the total lengths of the metallic strips are much longer than the unit cell size. However, the Ω-ring and S-ring are too complicated
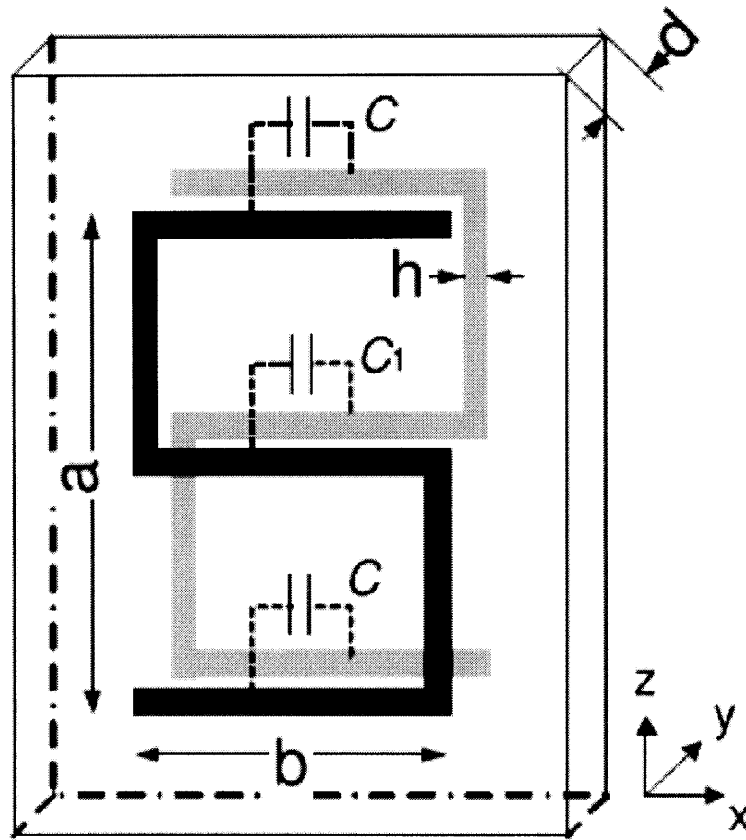
Figure 5-4: The S-ring resonator in [38]. The parameters are taken as the same in the paper, where a=5.2mm, b=2.8mm, h=0.4mm, and d=0.5mm. The permittivity for the dielectric board is 4.6.

to be directly extended to two dimensions. Each unit cell can only have rods in one direction; therefore each cell can only supply one direction for negative permittivity and one direction for negative permeability. A new LH metamaterial design for TM is essential and required for the realization of backward Čerenkov radiation.

5.2 A new LHM design for TM incident wave

Our aim is to have a design which can have the dielectric constants in form of Eqs. (5.1a) and (5.1b). Therefore, we need to have rods in two dimensions.

5.2.1 The dimensions

We adopted the side-couple principle for the new design. The rings and rods lie in x-y plane. The top view of a unit cell is shown in Fig. 5-5, and the bottom shape is the top one rotated by 90 degree around the normal of the board as shown in Fig. 5-6(a). Fig. 5-6(b) shows the side view of a unit cell, and the dimensions in the $\hat{z}$ direction are also marked. The periodicity in $\hat{z}$ is a in order to make the unit cell cubic.
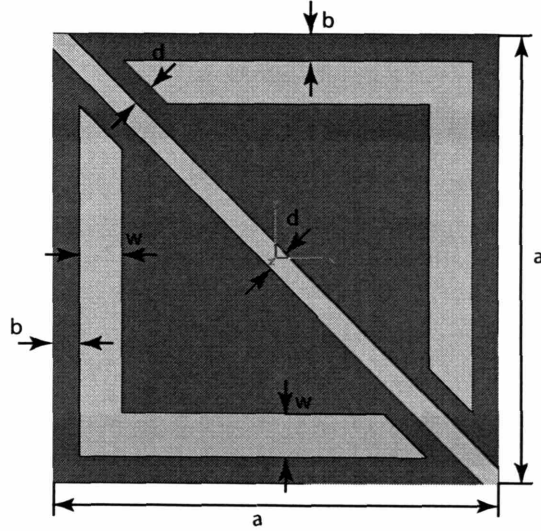
Figure 5-5: This is the top view of the design. The purple color means the dielectric board, whose permittivity is $\epsilon_r = 4$. The metal (green color) is in L-shape and the diagonal strip. a=5mm is the periodicity, d=0.24mm is the gap between the diagonal metal strip and the L-shaped metals, as well as the width of the diagonal metal strip, b=0.3mm is the distance between the L-shaped metals and the boundary of the unit cell, and w=0.48mm is the width of the L-shape metals.

The two diagonal metal strips on the top and bottom will serve as rods for two orthogonal directions, which can realize isotropic negative permittivity in the $\hat{x}$ and $\hat{y}$ directions.
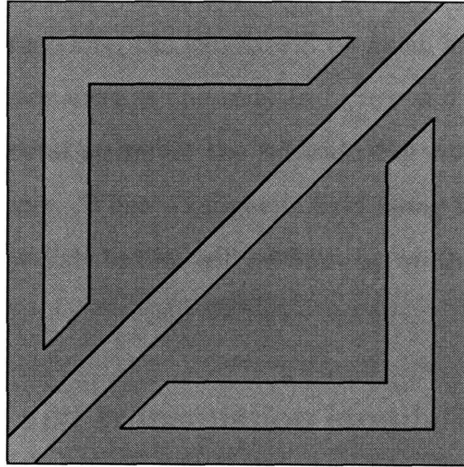
(a) Bottom View.
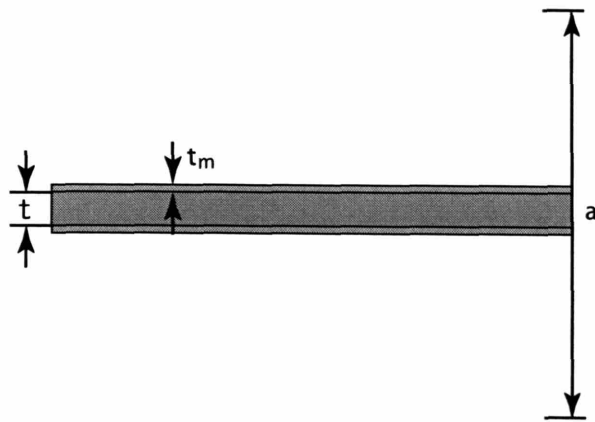
(b) Side View.

Figure 5-6: The periodicity in the normal direction of the board is also a=5mm, which make the unit cell a cube. t_m=0.05mm is the thickness of the metal, and t=0.2mm is the thickness of the dielectric board.

In order to lower the resonant frequency of the rods, we need to make the rods longer. Therefore, the diagonal strips are made to touch the boundary of a unit cell. The adjacent cells will be the center one rotated by 90 degree along the normal of the plane, the $\hat{z}$ direction. Through this transformation, the rods of the adjacent cells will be connected together; therefore, the length will be much larger than the dimensions of a unit cell, and the resonances of the rods and rings will be better matched.

The two L shaped metal strips on the top side can couple with the two on the bottom to form a resonator. When a magnetic field along the $\hat{z}$ direction is incident upon the ring, the charge distribution will be built up on the rings since they are not closed.

5.2.2   Reflection and transmission simulations

Starting from this section, we will work on identifying LH behavior using numerical simulations. The simulations here are all performed using CST Microwave Studio 5.0, in which the essential simulation method is Finite Difference Time Domain (FDTD).

Two numerical experiments are most commonly used. The first one is the reflection and transmission simulations, and the other is prism simulations which will be introduced in the next section.

For the reflection and transmission simulations, the purpose is to have a TEM incident wave, and to observe a transmission peak when both rings and rods coexist. The setup of our simulations is shown in Fig. 5-7.

One unit cell of the structure is located at the origin with the normal of the rings in the $\hat{z}$ direction. The two waveguide ports are placed at both sides of the unit cell in the $\hat{y}$ direction. Port 1 will be the source, and Port 2 is the receiver. In order to ensure a magnetic field along the $\hat{z}$ direction to excite the rings, the boundary condition in the $\hat{z}$ direction is set to be a perfect magnetic conductor (PMC). Similarly, the boundary condition in the $\hat{x}$ direction is set to be a perfect electric conductor (PEC), and an electric field in the $\hat{x}$ direction can be achieved. With these boundary conditions, a TEM wave is propagating along the $\hat{y}$ direction from Port 1 to Port 2.

The reflection and transmission are measured through S-parameters, and are rep-
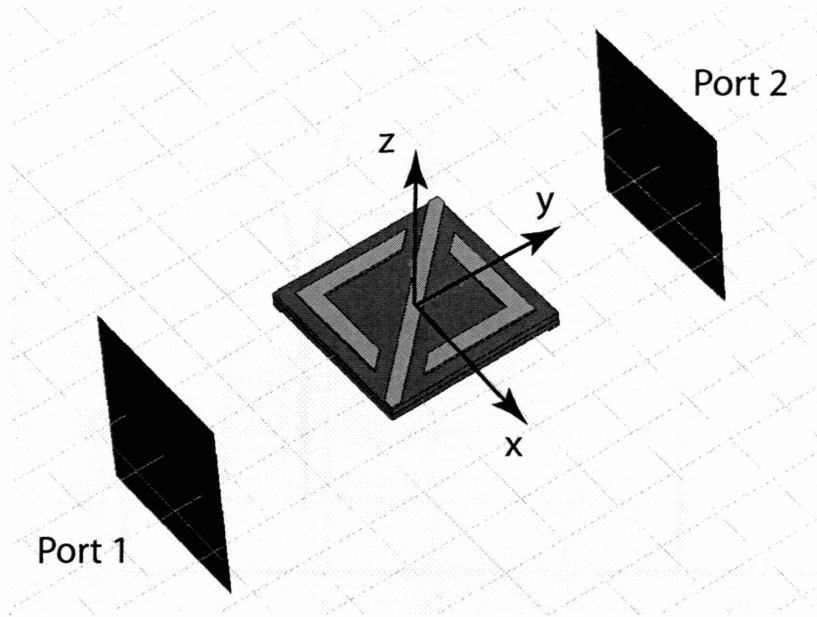
Figure 5-7: The setup of the reflection and transmission simulations for one cell. The red color region indicates the waveguide ports. The distance between each waveguide port to the nearest edge of the unit cell is 5mm, and the port size is 5mm × 5mm in the x-z plane.

resented as S_{11} and S_{12} respectively. The results are shown in Fig. 5-8. A peak of S_{12} can be clearly observed around 5.8GHz

We are expecting that the effective permittivity and permeability can be simultaneously negative at this frequency. However, a transmission peak does not necessarily indicate LH behavior in this frequency range. Therefore, the main purpose for the reflection and transmission simulation is to find the frequency range, where we will perform prism simulations.

Figure 5-8: S_{11} and S_{12} for the reflection and transmission simulation.

5.2.3 Prism simulations

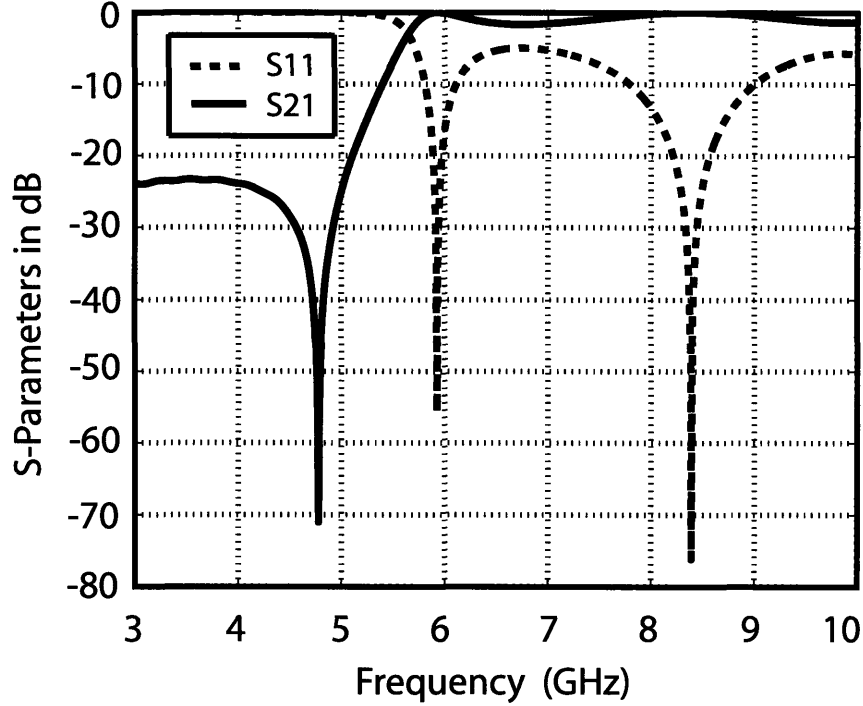The task of this section is to test whether or not the discovered pass band around 5.8GHz is due to the LH property, i.e. simultaneously negative permittivity and permeability. Known from the literature, among all experiments, the negative refraction in a prism experiment is the most convincing proof of LH properties. In the rest of the section, we will arrange the unit cells into a prism shape, and run simulations to observe the refraction angles at different frequencies. In the following two sections, both the TM and TE setups are shown for the prism simulations.

TM incidence setup

We adopt the commonly used prism angles [2] as shown in Fig. 5-9. The ratio between the number of cells in the $\hat{x}$ direction and that in the $\hat{y}$ direction is 3:1. The angle of the prism is $\theta_p = \arctan(1/3) \approx 18°$. In order to make the beam narrow enough

for a clear identification of the refraction angle, the prism is composed of 18 cells in the incident side, which is $1.8\lambda_0$ for the center frequency 6GHz. Therefore, there are 6 layers in the $\hat{y}$ direction.
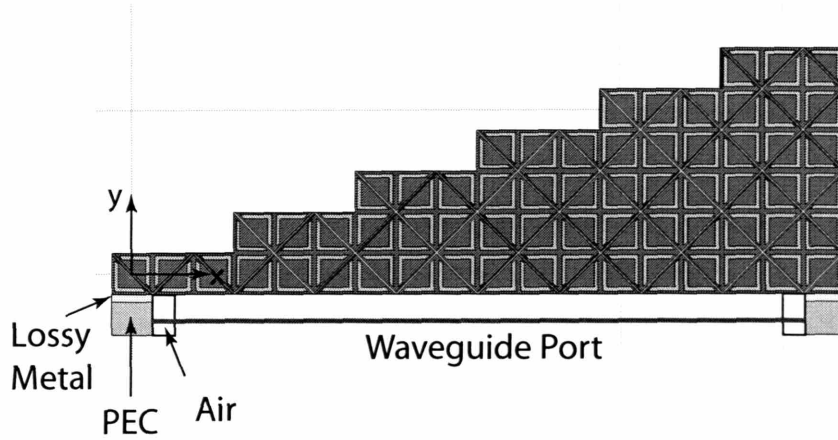

Figure 5-9: The top views of the prism setup for the TM incident wave. A waveguide port is placed at $y = -6mm$, which is 3.5mm to the horizontal boundary of the prism. Two PEC pieces (in blue color) are at the both sides of the waveguide port in the $\hat{x}$ direction. The dimension for each PEC piece is 4mm in the $\hat{y}$ direction and 5mm in the $\hat{x}$ direction. Two thin lossy metal pieces (in yellow color) are placed between the prism and the PEC, with the dimension being 1mm in the $\hat{y}$ direction and 5mm in the $\hat{x}$ direction. The two air pieces are placed on the top (bottom) of the waveguide port to prevent the waveguide port touching the top (bottom) boundary. The dimension for each air piece is 5mm in the $\hat{y}$ direction, 2.5mm in the $\hat{x}$ direction, and 0.5mm in the $\hat{z}$ direction.

The purpose for the PEC pieces is to limit the basic mode of the waveguide port which has an electric field in the $\hat{x}$ direction, and a magnetic field in the $\hat{z}$ direction; therefore a clean TEM incident wave can be formed. Two thin lossy metal pieces (in yellow color) are placed between the prism and the PEC in order to prevent the radiation from the surface waves when the wave is incident upon the prism. The air pieces on the top and bottom of the waveguide are to prevent the waveguide touching the boundary, and also force the program to add enough mesh lines to make the results accurate.

The boundary conditions in the $\hat{x}$ and $\hat{y}$ directions are set to "open", by which the program will use perfect matched layers (PML) on both sides of the directions. This

104

is a good feature of this design that the ends of the rods do not need to touch the wall of the wave guide. Since all the diagonal rods are connected, they are long enough to overlap the resonant frequency with that of the rings. The boundary condition in the $\hat{z}$ direction is periodic with the prism in the center. There are 3 layers in the $\hat{z}$ direction. The periodicity in the $\hat{z}$ direction is 5mm, which is the same as the dimension of a unit cell. The PEC and lossy metal pieces are both 15mm in $\hat{z}$ direction.

During the simulations, the incident wave is propagating along the $+\hat{y}$ direction. Both the near field and far field behaviors are monitored.

First, we observe the reflection coefficient at the waveguide port. The S-parameter S_{11} is shown in Fig. 5-10. A pass band between 5GHz to 7GHz can be observed clearly, which lies in the same frequency range as in the reflection and transmission simulations.
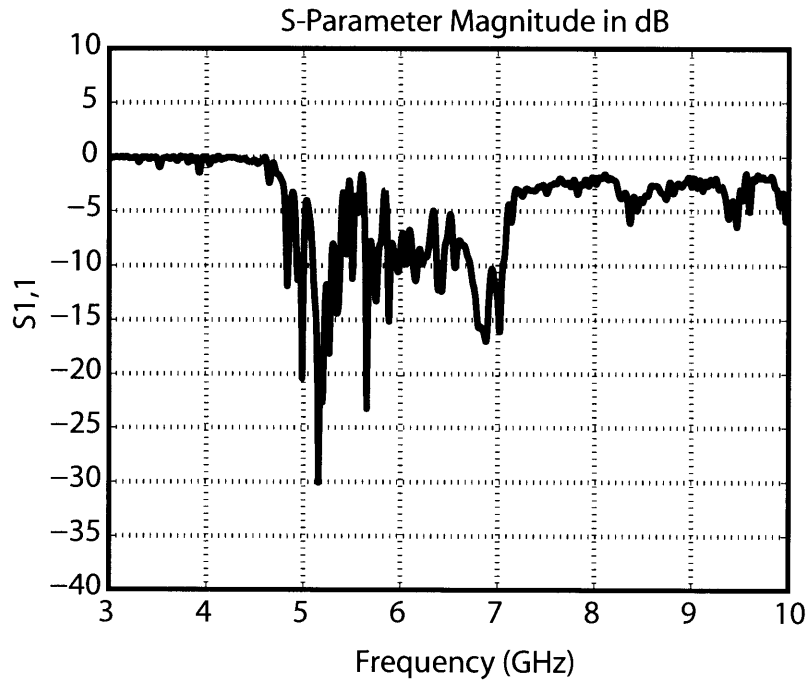

Figure 5-10: S_{11} for the TM setup prism simulation.

105

Secondly, the far field radiation patterns at different frequencies are observed. The linear plots of the far field beam are shown in Figs. 5-11. At the observed frequencies, the angle of the main beam at the far field is 138° for 6GHz, 124° for 6.3GHz, and 115° for 6.6GHz. All of these fall in the negative refraction region, since the normal to the prism is at 108°.
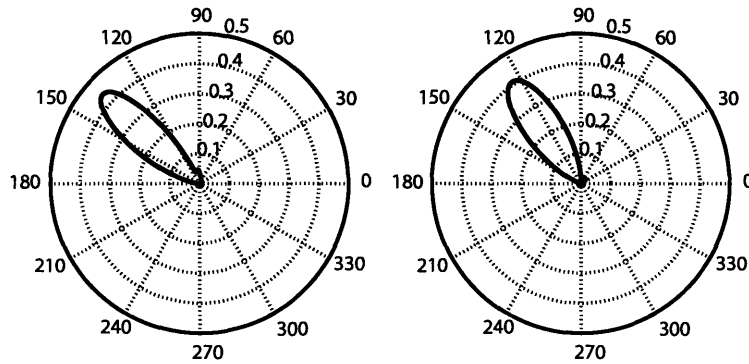
(a) At 6GHz. Main lobe magnitude 0.439VA/m², main lobe direction 137°, side lobe level -9.7dB.

(b) At 6.3GHz. Main lobe magnitude 0.409VA/m², main lobe direction 124°, side lobe level -12.5dB.
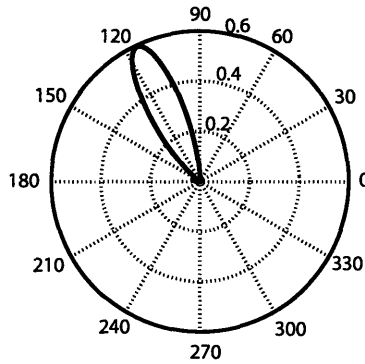
(c) At 6.6GHz. Main lobe magnitude 0.594VA/m², main lobe direction 115°, side lobe level -12.7dB.

Figure 5-11: The far field patterns of the power density in linear scale at a radius of 1m with respect to the center of the prism.

It is not necessary to show the far field pattern for all frequencies in the pass band. A summary of the refraction angles is given in Fig. 5-12. All the angles are adjusted so that the angles in Fig. 5-12 are the actual refraction angles with respect to the normal of the prism exit side. A negative refraction band can be clearly observed from 6GHz to 7GHz. The overall slope of the refraction angle is positive, which is consistent with the expectation that after the resonance, the refractive index increases from negative values to zero. Also 1GHz is wide enough for a possible experimental verification. The refraction angles for the frequencies below 6GHz do not show any consistent trend, which could be due to multiple reasons, for example the complicated behavior near the resonant frequency. However, what we are mainly emphasizing here is the behavior in the frequency band between 6GHz and 7GHz, where the structure shows a consistent and stable LH behavior.
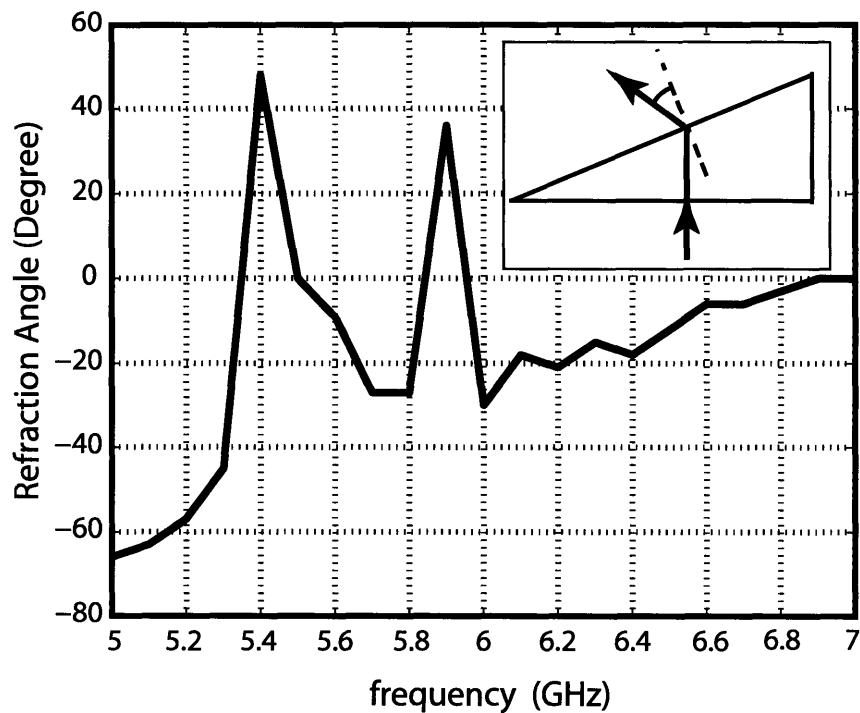

Figure 5-12: Refraction angles of the main beams for the prism simulation for the far field power density distribution. The refraction angle is defined as in the inserted ray diagram.

Besides the refraction angles, the loss is another important parameter for evalu-

ating the performance of the structure. If the loss is too high, the transmitted power could be too low to be identified in possible experimental verifications. Therefore we did the same simulations in the same frequency band by just removing the prism. The power at 1m radius is compared with that of the prism simulations. Only the absolute values at the peak of the beam were compared, and the results are shown in Fig. 5-13. It shows that roughly 80% of the power is transmitted at 6GHz, and the transmitted power is maintained above 50% for the frequency band of interest. The percentage of the transmitted power is higher than 100% at 6.8GHz and 6.9GHz, because the beam is actually narrower after the wave exits from the prism. This high transmission percentage shows that the loss of the structure is very low, which is another very good feature for experiments and applications.
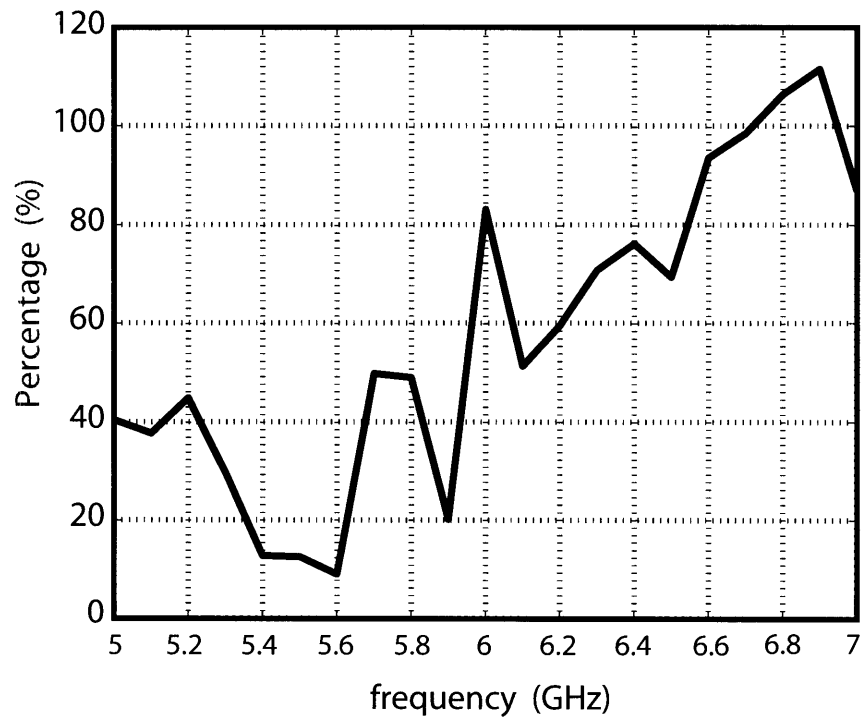

Figure 5-13: The ratio of the peak power density with the prism to that without the prism. The ratio for 6.8GHz is larger than 100%, because the beam for the prism simulation is narrower than that of the case when the prism is removed, 25.6° with the prism versus 26.9° without the prism. The same reason also applies for the value at 6.9GHz.

It is also worth noting that the transmission for the frequencies below 6GHz is much lower, which could again be due to the effect of the resonance and can serve as a confirmation of the inconsistent behavior of the refraction angles in this frequency band.
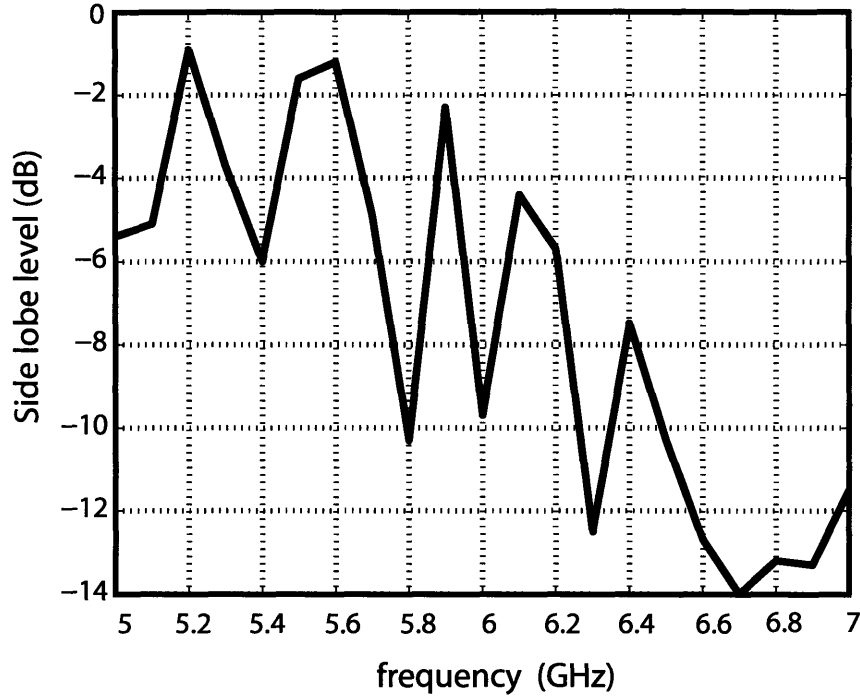

Figure 5-14: The relative side lobe level in dB for the TM prism simulations, where the side lobe level is defined the relative magnitude of the second maximum of the far field pattern with respect to the peak magnitude of the main lobe.

The level of the side lobe is another important factor which should be considered carefully for the prism experiment. If the side lobe is very strong and comparable to the main lobe, it may be very difficult to identify the real refraction angle due to the LH property of the structure, and therefore may lead to wrong results. We present the relative side lobe level with respect to the main beam in Fig. 5-14. It is seen that the relative side lobe levels are below -7dB for most frequencies between 6GHz and 7GHz, except between -5dB to -4dB for 6.1GHz and 6.2GHz. In general these side lobe levels are low enough for them to be distinguished from the main lobe. The low side lobe level provides a strong evidence that the observed main beam angles do

represent the refraction angle of through the prism.

Again, the side lobe levels below 6GHz are mostly high, above -3dB, which shows the behavior of the structure at the resonant frequency are less predictable.

Fig. 5-15 is a two dimensional plot of the H_z field in the near field at 6GHz. The pattern shows that the wave is propagating toward the negative direction (thinner side of the prism) after it exits from the prism. This is consistent with the far field observation, and is a clear demonstration of the negative refraction.
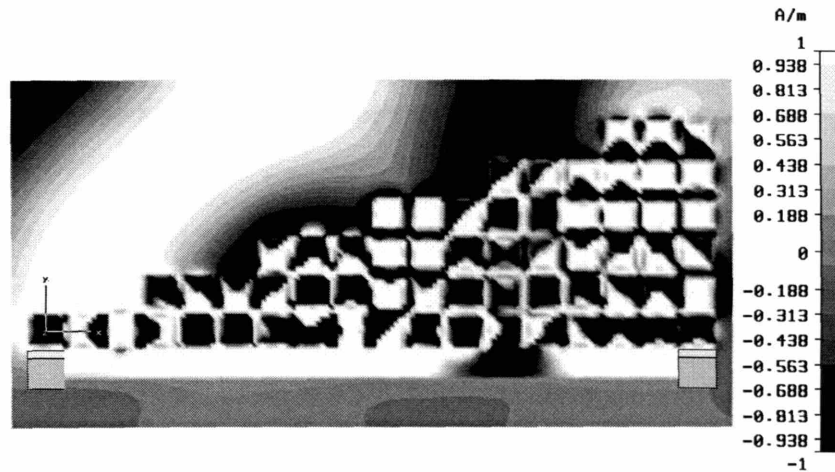
Figure 5-15: The near field plot of H_z at $z = 0$ at 6GHz.

We have thus shown the complete evaluation of the structure in Fig. 5-5 through the refraction angle, loss, and the relative side lobe level for a TM prism simulation. All of these results confirm that the structure behaves as a LHM in the frequency range between 6GHz and 7GHz for the TM wave incidence. As to the best of our knowledge, this structure is the first design which is isotropic for TM wave incidence.

TE incidence setup

This section shows that the same structure in Fig. 5-5 can also work for the TE incident wave also. Since our unit cell is a cubic, we can just erect the unit cells and align them as in Fig. 5-16.

The top and bottom boundary conditions along the z axis are set to PEC. Besides

Figure 5-16: The setup for the TE incident prism simulation.

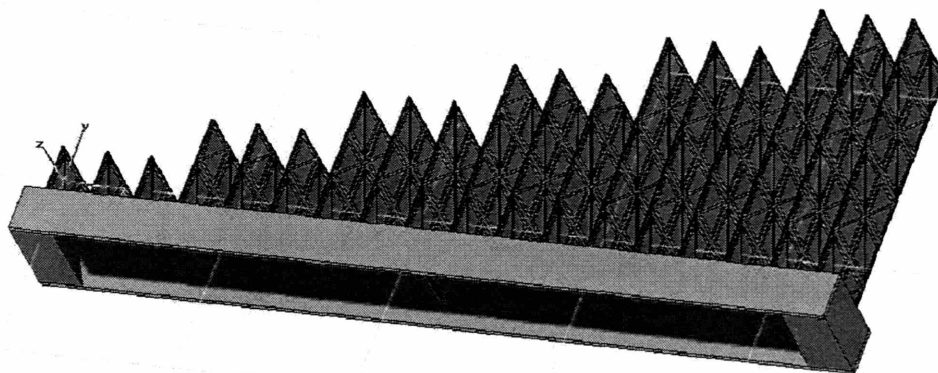the ability to force an electric field along the $\hat{z}$ direction for the basic mode, this boundary condition can also effectively extend the rods to infinity due to the mirror effect of PEC.

Two cells are erected along the z direction to form the minimum repeatable cell by translation operations. Similar to the TM prism, there are 18 cells in the incident side of the prism; therefore the incident port size is kept the same as for the TM prism simulations. At the top and bottom sides of the wave guide port, PEC strips (Green) are placed to ensure that the electric field is along the $\hat{z}$ direction, and to make the wave guide port not touching the simulation domain boundaries. At both sides in the x direction, two quadrangles (color) are placed. Their tilted faces form a horn to make the wave propagating out smoothly. The material is a lossy metal, which can also absorb the wave propagating in the x direction and reduce the side lobes due to the finite size of the prism.

The refraction angles at the far field are summarized in Fig. 5-17.

A negative refraction band is observed between 5.7 GHz to 7.2GHz. Note that the bandwidth is a little wider than for the TM case. The reason is that the rods are effectively extended to infinity due to the PEC boundary conditions. The behavior of the rods will be very close to that of a plasma; therefore a wider overlapping negative band can be expected.

111
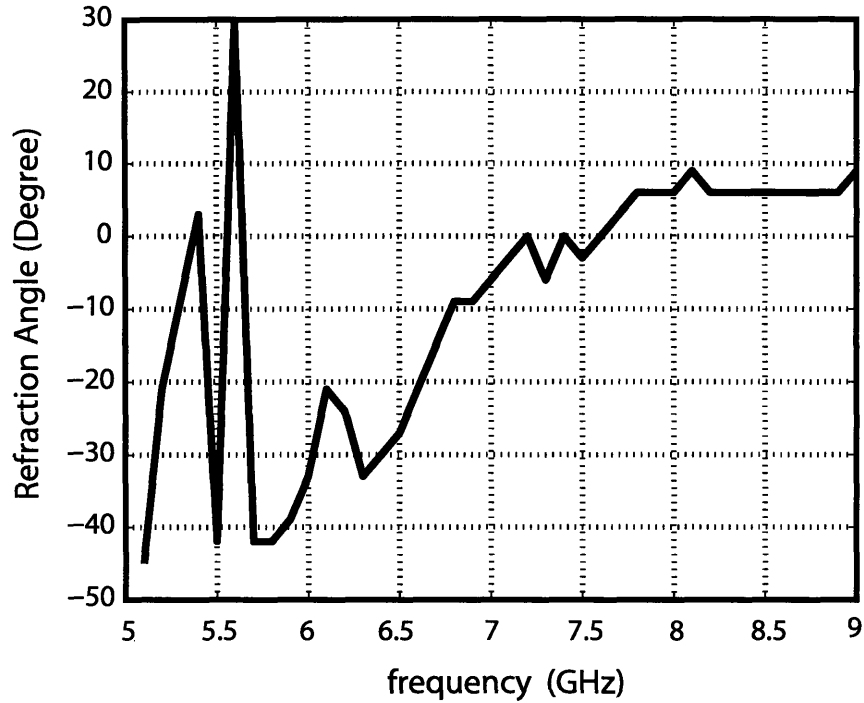
Figure 5-17: The refraction angles of the TE prism simulation at the far field. The angles are observed from the power density (VA/m^2) at a distance of 1m. The angles are the actual angle in the $x - y$ plane and are subtracted by 108° to reflect the real refraction angle. The refraction is defined the same way as in the insert of Fig. 5-12.

Similarly, we also present the percentage of the transmitted power and the relative side lobe level in Fig. 5-18(a) and Fig. 5-18(b), respectively. In the negative refraction band, the transmitted power is mostly higher than 60% which indicates that the structure has low loss and good transmission. The side lobe levels are less than -6dB, and the observed negative transmission peaks are reliable.
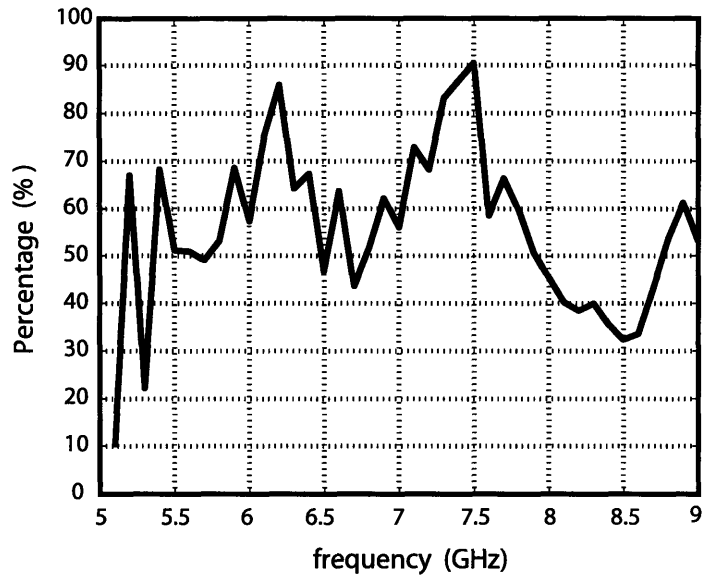
(a) The percentage of the transmitted power density at the peak value with respect to the values of air.
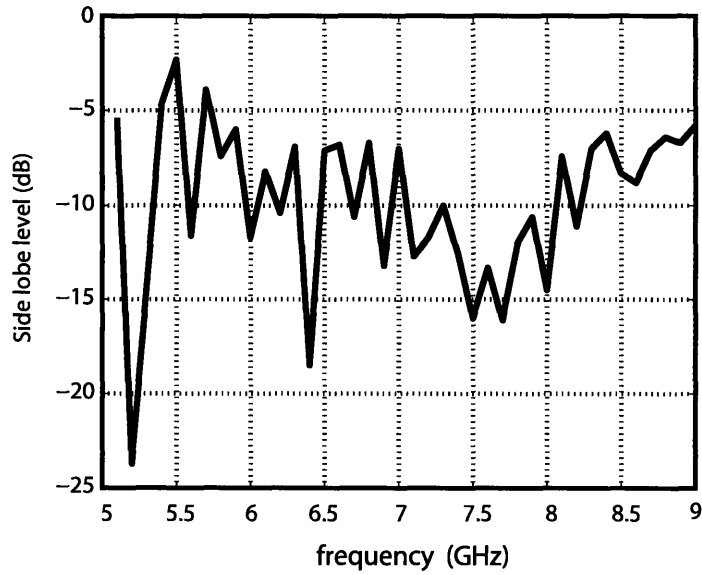
(b) The relative side lobe level in dB for the TE prism simulations.

Figure 5-18: Plots of the percentage of the transmitted power and the side lobe levels.

In order to directly compare the performance of the design for the TM and TE set-ups, we plotted the refractive index in Fig. 5-19. The refractive indices are obtained directly using Snell's law. This is already enough to give us an estimate of the refractive indices at different frequencies. The overlapping negative refraction frequency band shows that the design is robust for both the TM and TE simulations. It is also possible to make a 3D isotropic LHM by combining the TM and TE arrangements in the overlapped frequency for the LH behavior.
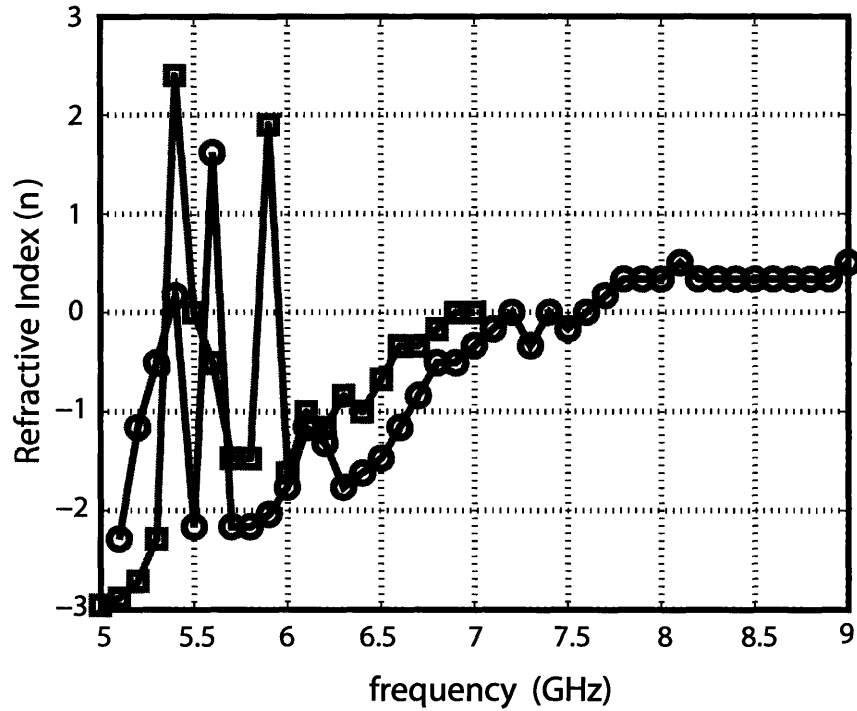
Figure 5-19: The inverted refractive index for both the TM and TE prism simulations.

5.3 Modeling of traveling line current

When a charged particle passes through the LH structure, all the frequencies will shwo radiation, forward or backward, propagating or evanescent. Therefore we may not get clear backward radiation results if we shoot the charged particle directly into the structure given its high dispersive properties.

114

We therefore propose to use a traveling line current source to investigate the properties of Čerenkov radiation in LH structures. This is easily understandable from theory.

When a charged particle travels along the $\hat{x}$ direction, the current can be written as

$$\overline{J}(\overline{r},t) = \hat{x}qv\frac{\delta(\rho)}{2\pi\rho}\delta(x-vt) \tag{5.3}$$

where ρ represents the radial dimension in the $y-z$ plane. This may be different from common sense, because here we just want to keep the setup of the prism, and to have the particle travel along the $\hat{x}$ direction. The current can then be expressed as a superposition of the full spectrum through use of the Fourier transform, where each spectral component is expressed as

$$\overline{J}(\overline{r},\omega) = \hat{x}\frac{q}{4\pi^2\rho}\delta(\rho)e^{ik_x x} \ , \tag{5.4}$$

where $k_x = \omega/v$. The radiation of each frequency component in a LH structure can be investigated, and the radiated power will be pure backward if we choose the frequency in the negative refraction band of the TM case.

However, this is just a theoretic model for the traveling current, and it is not realizable in real experiments. Therefore, we further developed an antenna array to model the traveling current, as shown in Fig. 5-20. We used 20 electric dipoles for a whole length of 10cm. At 6GHz, the length is $2\lambda_0$. The distance of two adjacent dipoles is $\Delta = 5mm = \lambda_0/10$. A fixed phase difference $\alpha = k_x\Delta$ is set between two adjacent dipoles, which accounts for the phase change as the current travels in the continuous model.
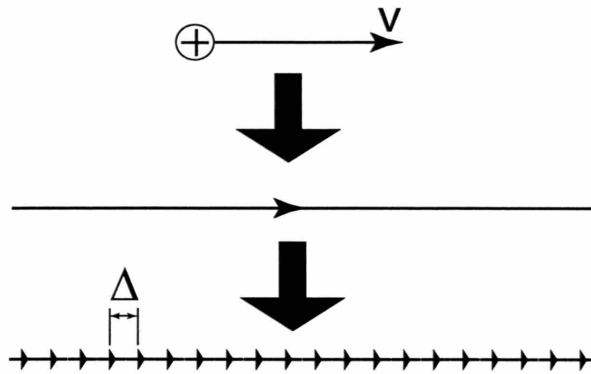
Figure 5-20: Modeling process of traveling current. Δ is the distance between the two adjacent dipole, which is 5mm in our simulation here, and the center frequency is 6GHz. The big arrows indicate the modeling processes from the charged particle motion to a ideal traveling current, and to an array of dipoles.
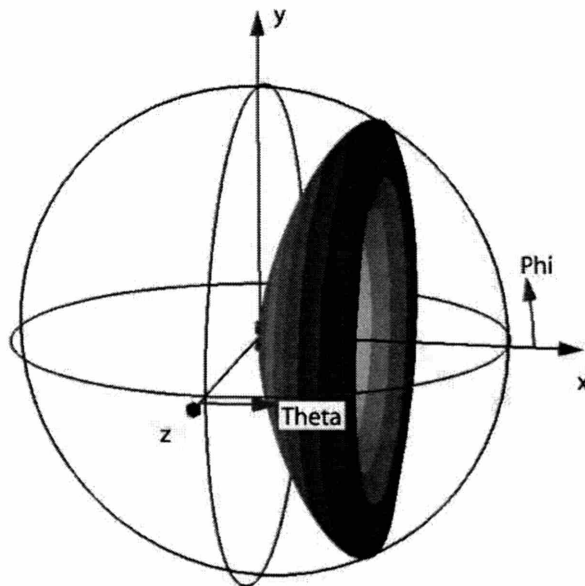
Figure 5-21: 3D far field radiation pattern for dipole arrays. The distance between the adjacent dipoles is $\Delta = 5mm$. In order to have the radiation angle in 60°, the effective wave vector k_x along the direction of the antenna array should be $k_0/2$, therefore the phase difference α is 18° for this simulation.

By adjusting the phase α, we can effectively change k_x. The radiation angle can be set to any angle, $\theta = \arccos(k_x/k_0)$. For simplicity, we set $k_x = k_0/2$, and therefore $\alpha = k_x\Delta = 18°$ with the radiation angle being 60°. Fig. 5-21 shows the 3D radiation pattern. A cone pointing 60° is formed as shown in Fig. 5-22. The formed cone is identical to the radiation of a charged particle in non-dispersive normal media, which is what we want to achieve with our antenna array model.
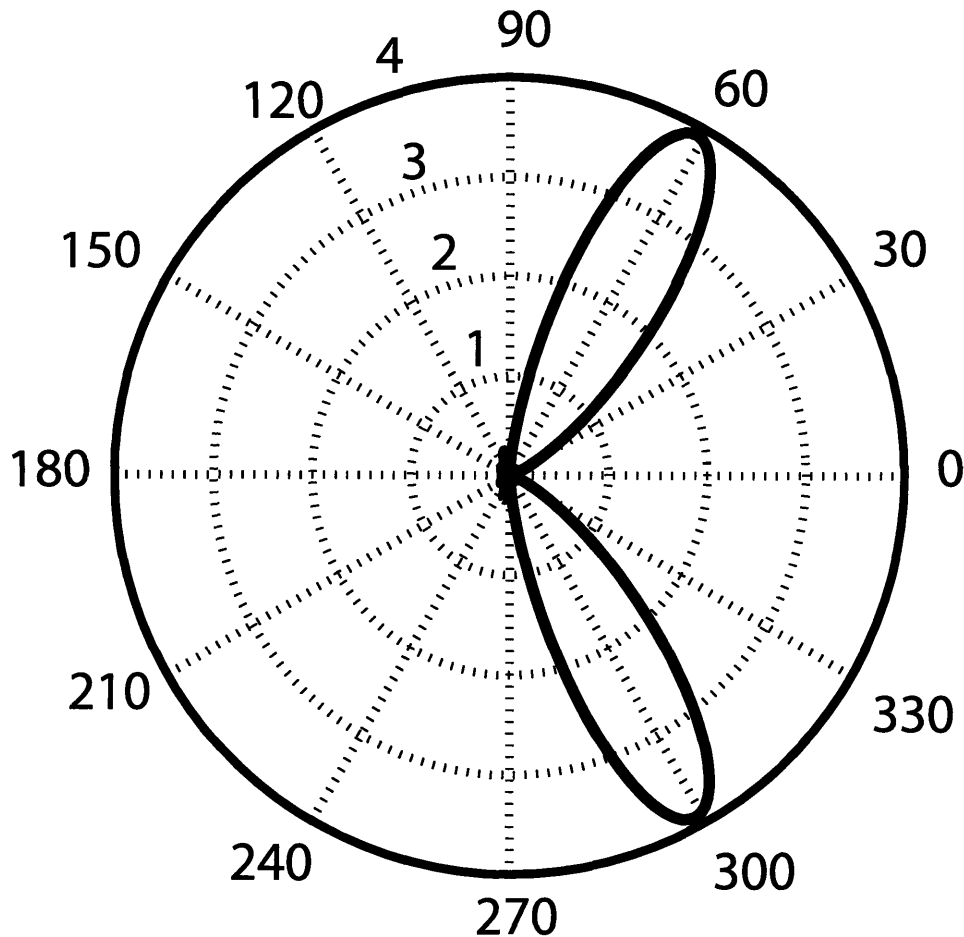
Figure 5-22: 2D far field radiation pattern at 6GHz for an array of 20 dipoles as shown in Fig. 5-20, with $\Delta = 5mm$, and $\alpha = 18°$. The angular width is 29.5° and is defined as the width of the angles at which the power density is 3dB lower than the peak value. The side lobe level is -12.0dB, by which we can clearly identify the direction of the main beam.
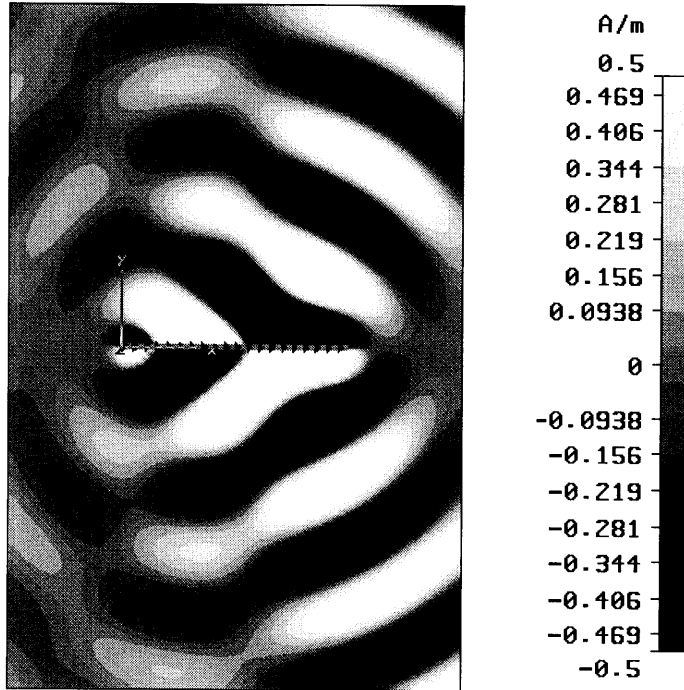
Figure 5-23: H_z field at 6GHz for the antenna array of 20 dipoles, with $\Delta = 5mm$, and $\alpha = 18°$. A clear phase front can be defined.

Both Figs. 5-22 and 5-23 confirm the quality of the beam. In Fig. 5-22, the angular with of the beam is 29.5°, which is narrow enough for a flat phase front as shown in Fig. 5-23. With this flat phase front, we can ensure the radiated wave is approximately plane wave when it incident upon the LHM.

5.4 Radiation of traveling line current in LH structures

It is of great interest to study the phenomenon when we put the antenna array into LH structures.

5.4.1 Traveling line current in homogeneous isotropic RH and LH materials

In order to make some theoretical predictions, we first put two effective LHMs on the two sides of the antenna array. The effective material is assumed to have a permittivity and permeability that is described by the Drude model. Also for simplicity, we adjust the model, such that both the permittivity and permeability are -1 at 6.4GHz in order to match the results for our prism simulations, in which the effective refractive index is approximately -1 for TM wave incidence as shown in Fig. 5-19.
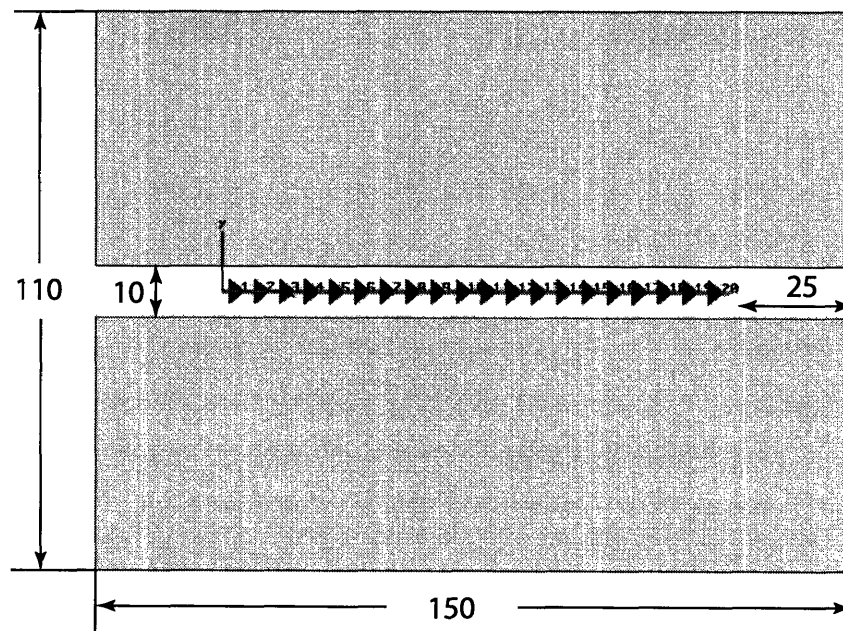
Figure 5-24: The setup for the simulation by putting the antenna array shown in Fig. 5-20 in between two effective LHM slabs. The length unit is mm for the dimensions marked in the figure.

119

We are expecting the phase to be titled in the opposite direction in the LHM in comparison with that of air. The simulation results are the same as expectation, as shown in Fig. 5-25. Here H_z is plotted, and this result can be used as a benchmark for the following simulations for the real structure.
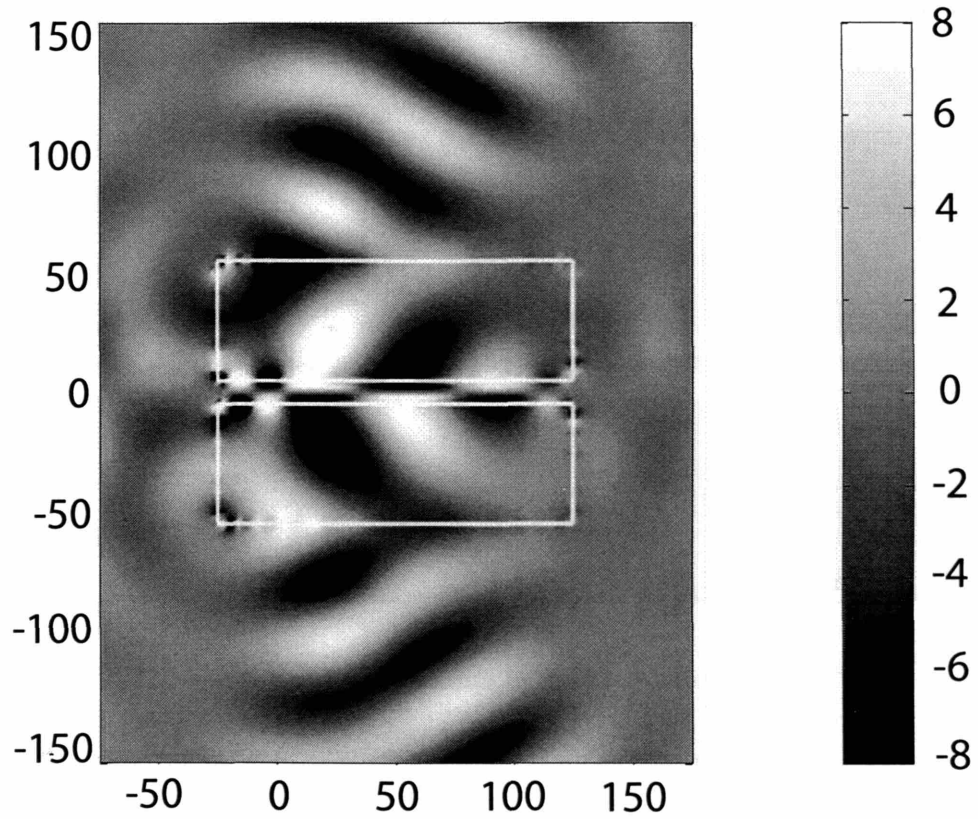
Figure 5-25: Simulated H_z field pattern at 6.4GHz when the antenna array is put in between the two effective LHM slabs (see Fig. 5-24).

5.4.2 Traveling line current in the new LH meta-material design

Meta-material as a slab shape

Immediately following the previous section, we put the antenna array into the LH structure, as shown in Fig. 5-26.
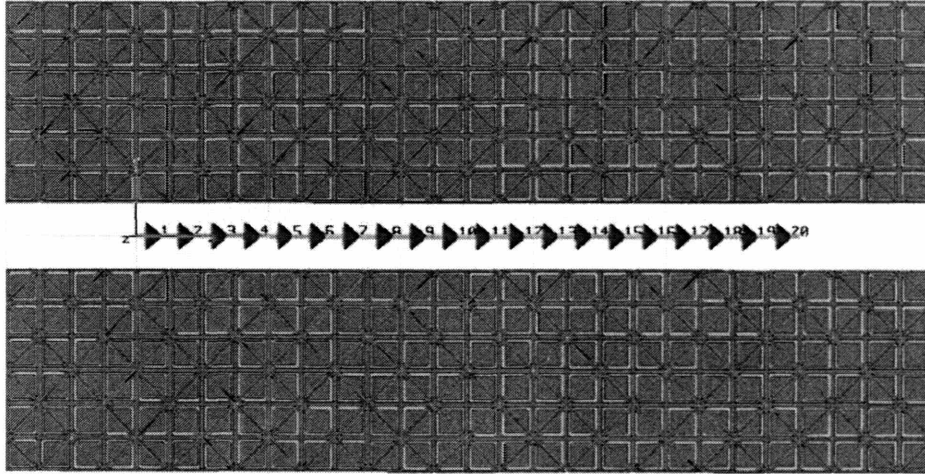
Figure 5-26: The setup for the simulation by putting antenna array in between the LH stucture slabs.

The LH structure is made such that it covers the length of the antenna array. There are 28 cells in the $\hat{x}$ direction. The extra 4 cells are at the both ends of the antenna array in $\hat{x}$ direction are to catch the radiation out of the two ends of the antenna array, and therefore the magnitudes of the side lobes are reduced.

Figs. 5-27(a), 5-27(b), and 5-28(a) show the simulated magnetic field at 6GHz at 3 different planes for $z = 0$mm, 1.25mm, and 2.5mm.
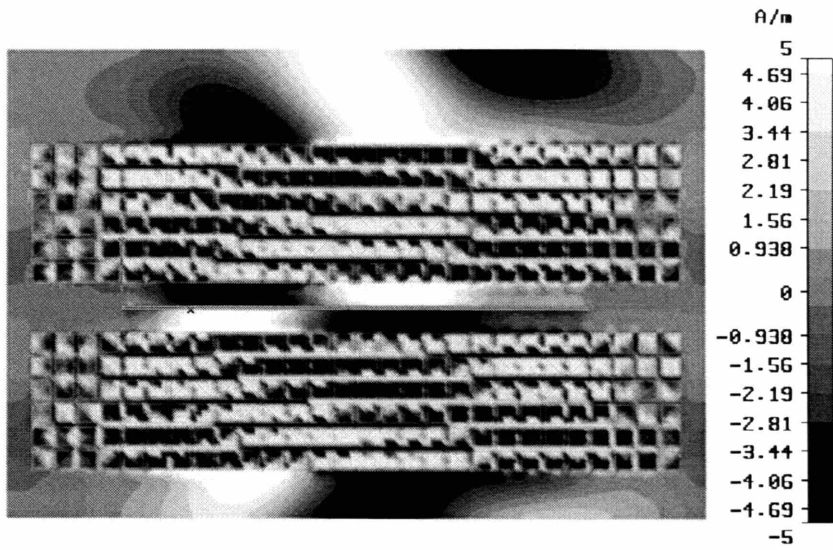
(a) $z = 0$mm.
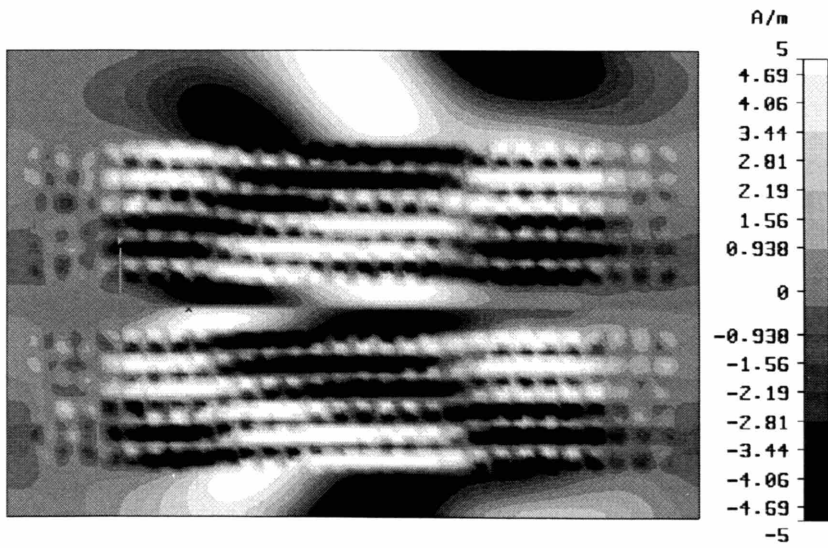
(b) $z = 1.25$mm.

Figure 5-27: Distribution of H_z field in the $x - y$ plane at 6GHz.
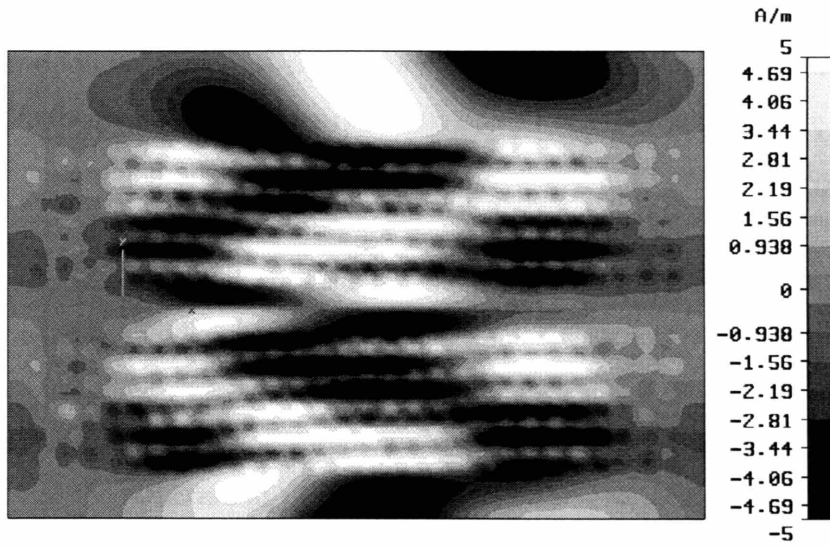
(a) 6GHz.
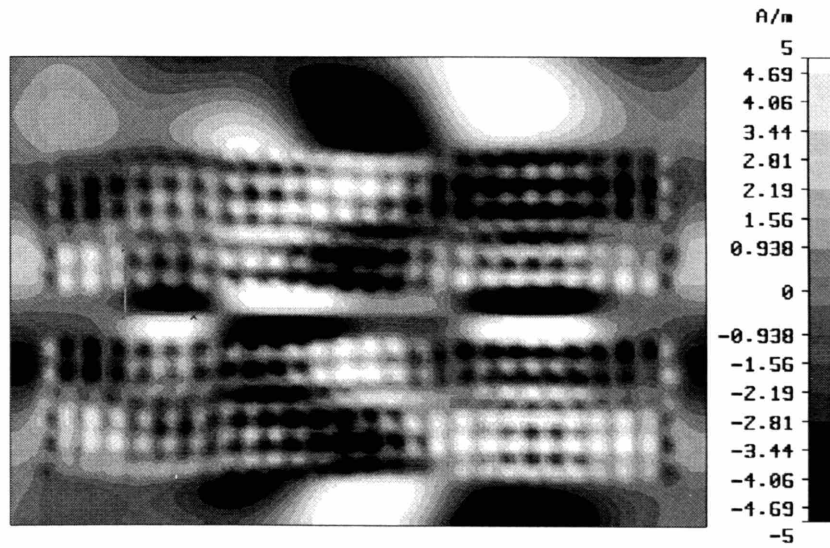
(b) 6.4GHz.

Figure 5-28: Distribution of H_z field in the $x - y$ plane for $z = 2.5$mm.

Observing the H_z field at $z = 0$mm, as shown in Fig. 5-27(a), the field inside the LHM slab is much stronger than outside. The backward phase pattern is not clear here. This is because the structure is resonating, and a high field is generated.

When we observe outside the structure on the plane at $z = 1.25$mm, the field strength in the region above the structure is much lower now. It is easy to notice that the normal direction of the phase front is pointing into the center in the interested region.

Fig. 5-28(a) shows the H_z field on the plane for $z = 2.5$mm at 6GHz. This position is in the middle of two adjacent layers of the structure. So the field is more homogeneous. The phase is propagating toward the x axis.

From the prism simulations results in Fig. 5-19, we know that the effective refractive index of the structure at 6GHz is about -1.6 for TM incident waves. Therefore the refraction angle in the structure should be smaller than the incident angle. As we can see in Fig. 5-28(a), the more flat phase inside the structure indicates that the propagating direction is closer to the normal of the boundary, which is consistent with expectation.

In order to further verify the LH behavior at a different frequency, we observed the H_z field distribution at another frequency 6.4GHz, at which the structure has an effective refractive index close to -1. As shown in Fig. 5-28(b), the refraction angle inside the structure is actually larger, because the absolute value of the refractive index inside the structure becomes smaller.

The x component of the electric field is also observed at the plane $z = 2.5$mm for the frequencies at both 6GHz and 6.4GHz in Figs. 5-29. The electric field is more homogeneous than the magnetic field, because the observed frequency is close to the magnetic resonant frequency of the rings, and the H_z field is dominant. The different refraction angles inside the structure region clearly demonstrate the different effective refractive index at these two frequencies. In Fig. 5-29(a), the phase inside and outside the structure region has almost the same slope but with a different sign, which is consistent with the effective -1 refractive index at 6.4GHz.
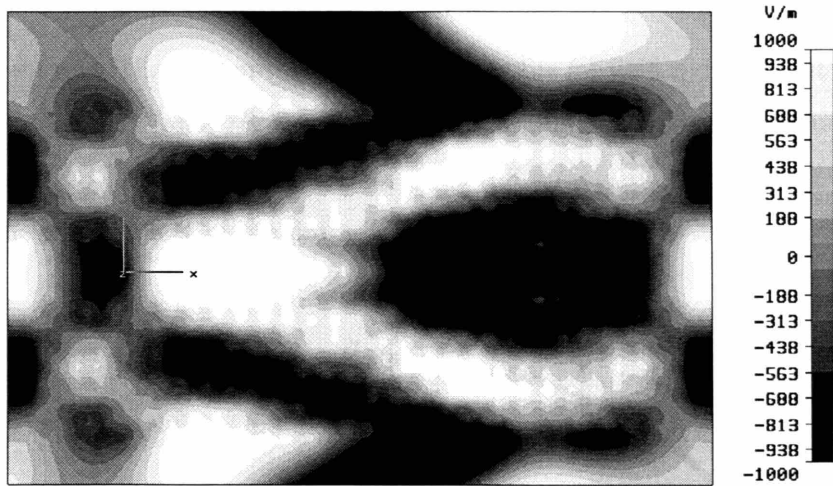
(a) 6GHz.
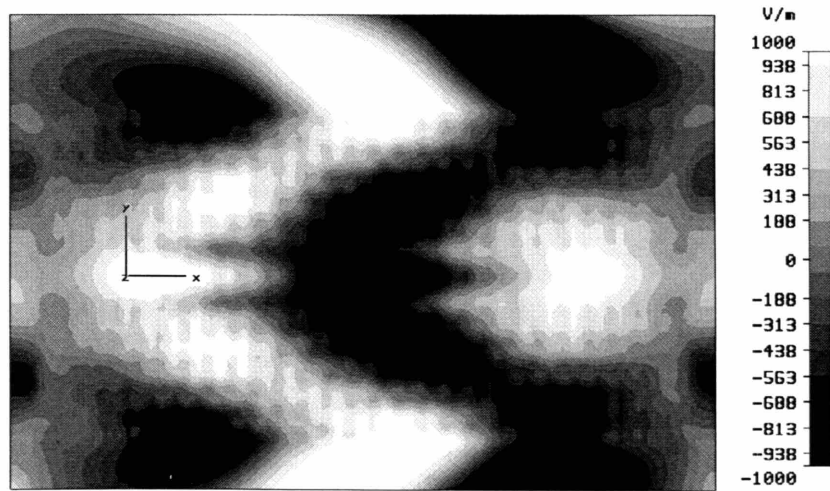
(b) 6.4GHz.

Figure 5-29: Distribution of the E_x field in the $x - y$ plane for $z = 2.5$mm.

Since the structures are arranged as a slab, the far field radiation pattern should not be affected. The angle of the main lobe should still be 60°. The far field pattern is shown in Fig. 5-30. The bottom structure slab was removed in order to compare the amplitude and estimate the loss of the slab.

We confirmed that the upward smaller lobe is the far field radiation after the wave exits from the LHM slab. Both the reflection and inherit loss of the structure make this lobe 3.6dB lower than the lobe without the structure. The 4° off from 300° is due to the corner effect of the finite LHM slab.
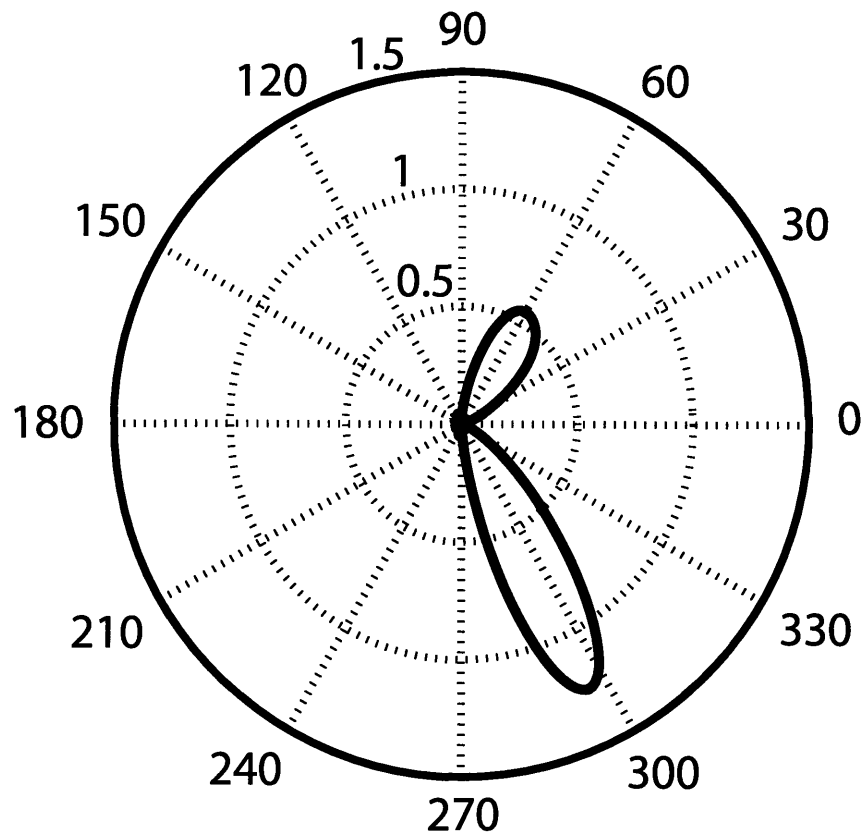
Figure 5-30: The far field power density of the radiation for the antenna array inside the LH structure. The bottom piece is removed in order to compare the relative magnitude of the free space radiation and the radiation after passing through the slab. The lobe at 60° for LH structure is 3.6dB lower than the lobe at 296° for free space.

Meta-material as a prism shape

We have demonstrated in the previous section that the backward wave can be formed inside the LH structure slab when we use the antenna array as the traveling line source. However, as shown in Fig. 5-30, the far field radiation direction will not be changed, which makes it difficult to verify the presence of the backward wave through experiments. Although the researchers can insert some sensor into the space between the two layers of the structure, a far field clear signal which can show the backward wave effect is still desirable.

Therefore, we propose to change the shape of the LH structure around the antenna array to be a prism. The prism angle is the same as in Fig. 5-9, with the prism angle being approximately 18°. The setup of the simulations is shown in Fig. 5-31.
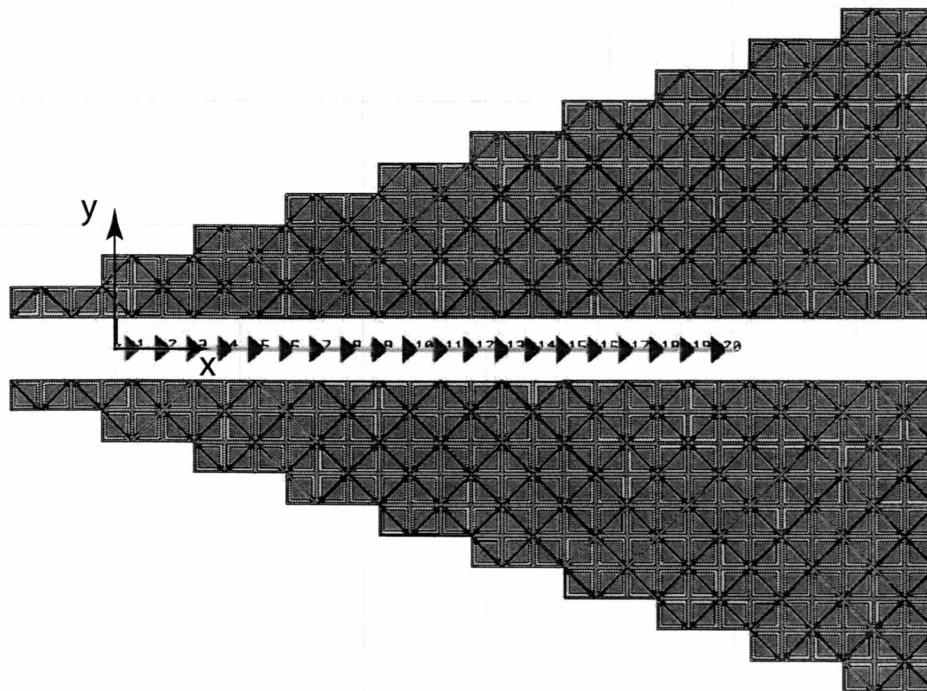
Figure 5-31: The antenna array is surrounded by two LH structures in prism shape. In comparison with Fig. 5-26, the LH slabs are replaced with the LH prism.

According to this angle, we adjust the phase difference α to 11.1° in order to make

the wave radiate to 72° with respect to the $\hat{x}$ direction in air, other parameters the same. The rationale behind this adjustment is that we select the incident angle to the prism as 18° at which the backward wave inside the prism will have its phase front aligned with the prism exit boundary, which forms a normal incidence from the prism to the air. A ray diagram shown in Fig. 5-32 illustrates the directions of the exit beam when the structure behaves as a LHM and as a RHM. Through this design, the separation of the beams of the LHM and the RHM frequency bands can be amplified, which can make the experimental signal clearer.
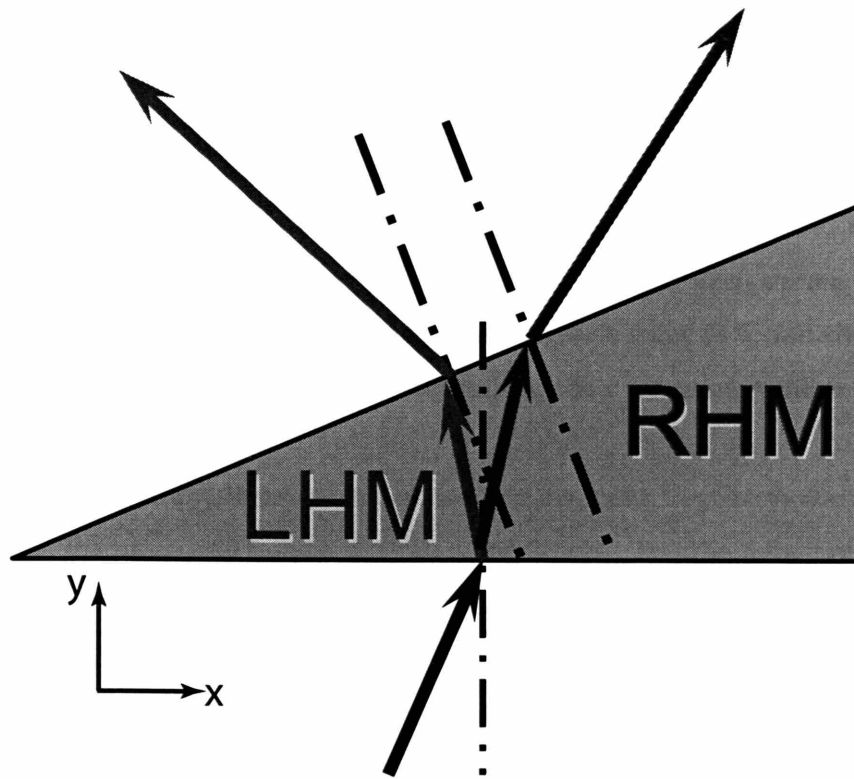
Figure 5-32: The Ray diagram shows the different exit directions for the prism's behavior as a LHM and as a RHM. The far field direction will be amplified through this design. The black arrow line indicates the incident wave from the antenna array. The yellow dash-doted lines are the normal of the two boundaries of the prism. The direction of the beam in the LHM (RHM) frequency band is indicated as red (blue) arrow.

With this design, the refraction angles inside the prism will be widely separated when the effective refractive index of the LHM changes from small negative to small positive as the frequency increases. For the small negative refractive index, the refracted wave inside the prism will hit the tilted side of the prism, and the final refraction angles in the free space, after the wave exits from the prism, will be close to the normal direction of the tilted side of the prism. This is because the effective refractive index is close to 0, and all the refracted beam into the free space will be along the normal, which is 108° in the x-y plane. Interestingly, for very small positive refractive index, the refraction angle inside the prism could very large, such that the refracted the wave will hit the right side of the prism first, and the main beam will exit from the right side of the prism, and form a main lobe along the $\hat{x}$ direction. There still will be a lobe in the normal direction of the tilted side of the prism which is due to the multiple reflection inside the prism. As a whole picture, we should expect the far field main beam angle (with respect to the $\hat{x}$ axis) decrease to 108° when the effective refractive index changes from negative value to 0, and then a main lobe should be expected at 0° which corresponds to the $\hat{x}$ direction, while a decreased lobe in 108° should still exist.

When the frequency decreases and passes the resonant frequency, the refraction angle inside the prism will not be separated very widely, but the refraction angle in the free space will be widely separated. The reason is that the effective refractive index will change very quickly from large negative to large positive.

The far field patterns of the radiated wave for several frequencies in the LH band are shown in Figs. 5-33. For the observed frequencies, 6.1GHz to 6.6GHz, backward radiated main lobes are obtained. As the frequency increases, a general trend of reducing the angle can be concluded, which is consistent with the previous prism simulations. The LH frequency band lies higher than the resonant frequency, by causality, so that the refractive index should increase from negative value to 0. The multi-lobes at 6GHz could be due to the fact that this frequency is close to the resonant frequency, at which the behavior of the structure is not stable.
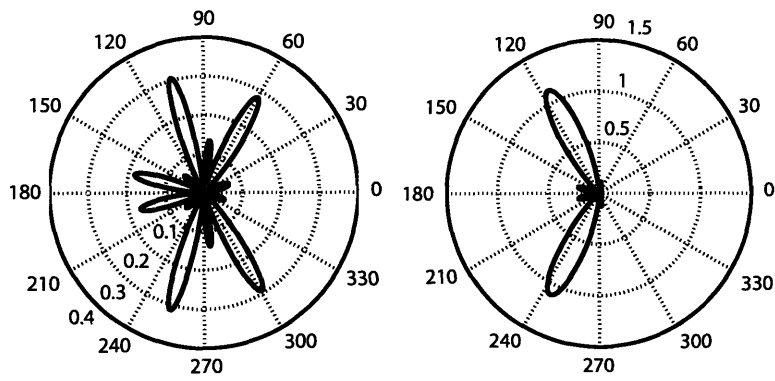
(a) Frequency 6GHz. Main lobe direction 106°.

(b) Frequency 6.1GHz. Main lobe direction 116°.
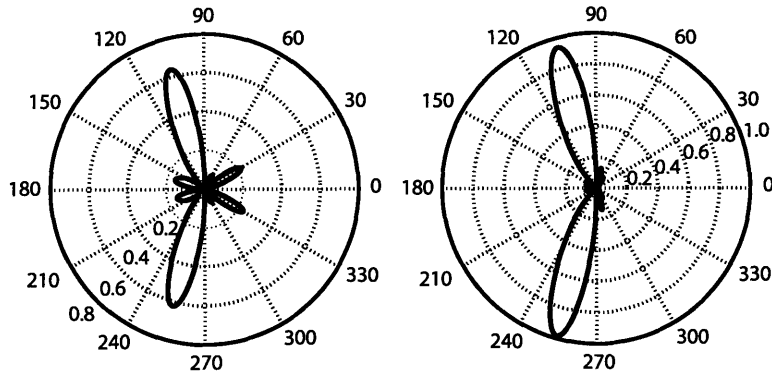
(c) Frequency 6.2GHz. Main lobe direction 106°.

(d) Frequency 6.3GHz. Main lobe direction 105°.
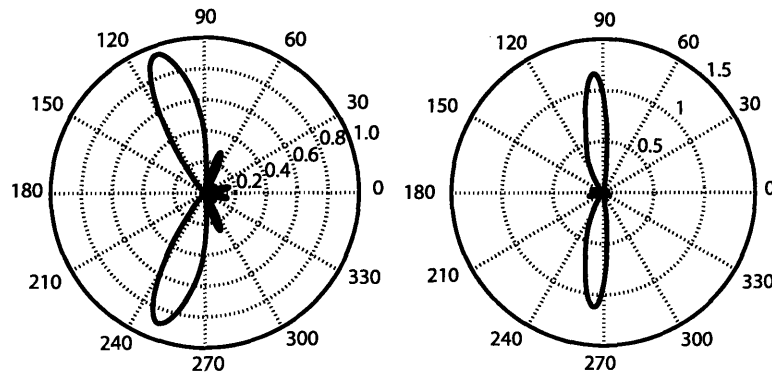
(e) Frequency 6.4GHz. Main lobe direction 109°.

(f) Frequency 6.6GHz. Main lobe direction 95°.

Figure 5-33: Far field radiation pattern for LH frequency band for the antenna array inside the LH prism.

130

For all these simulations, the input power was normalized to 1W, where each antenna has a feeding current of 1A. And the far field pattern is the plot of the power density at a distance of 1m away from the prism. In this setup, the peak power density for the main lobe is $1.12W/m^2$.

For completeness, we also show the near field plot of E_x field at 6.4GHz in Fig. 5-34. The small triangle shape along the $\hat{x}$ direction for y close to 0 shows the cone of the radiation from the antenna array in air. After the wave enters the prism, the normal of the phase points to inward. We can see that the phase inside the prism align with the exit boundary of the prism, which indicate that the effective refractive index is close to -1. This result is the same as what we have observed in the initial prism simulation, "the effective refractive index at 6.4GHz is close to -1".
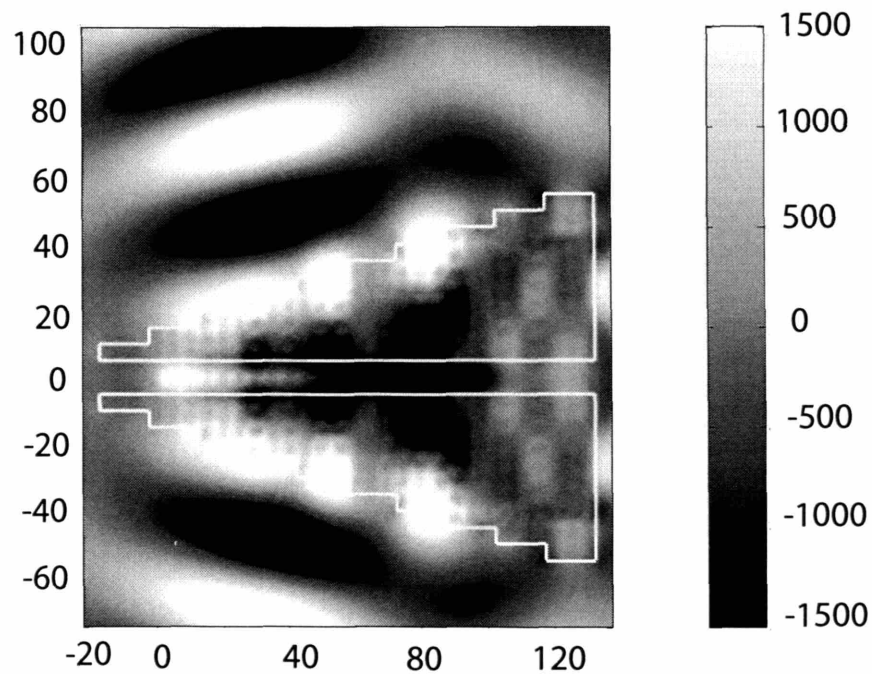
Figure 5-34: Near field plot of E_x at 6.4GHz.

5.5 Conclusions

We have shown our new LHM design for TM wave incidence in this chapter. The properties of the design were fully explored through numerical simulations. This new design can be scaled to the THz frequency band to realize the LHM prism experiment in the THz frequency band, which cannot be achieved by previous available designs.

We also designed an antenna array to model the traveling current, a decomposed component of charged particle motion. The various simulations confirm that this new design can generate the backward wave when the antenna array is put in between.

In a typical LHM prism experiment, the input power for a single antenna is 10mW, and the detector was placed 15cm away from the prism, with the resolution being $0.03nW/mm^2$. If we scale our input power to the typical experiment input, 10mW, the power density for the main lobe at 30cm (6 times the wavelength) is $124nW/mm^2$. This value is more than 4,000 times higher than the resolution of the detector. Therefore the far field signal should be detectable.

Chapter 6

Conclusions

In Chapter 2, we have theoretically studied Čerenkov radiation in an unbounded homogeneous effective LHM. The second kind of Hankel function is shown to be the proper Green's function, which can describe the forward and incoming phase, while the calculated Poynting vector is outgoing and backward. With this choice of Green's functions, both the energy and momentum conservation can be satisfied. And we also learned, the momentum and the energy flow are in the opposite directions in a LHM. When the dispersion is considered, the medium will behave as a RHM in the frequency band for both positive permittivity and permeability, and as a LHM in the frequency band for both negative permittivity and permeability. Therefore the corresponding Green's functions should be chosen at different frequency bands. As a result, when a relativistic charged particle passes, both forward and backward radiations will be generated. The total radiation depends on the dispersion of the permittivity and permeability. When loss is induced, the backward radiation will be reduced, since the LH band always falls in the close region, higher than the resonant frequency, in which the loss is high. Therefore the radiation will be dominated by the low frequency region far from the resonance, where the dielectric constants are positive and the loss is very low. As the loss decreases, the radiation near the resonance becomes dominate, since the refractive index is much higher in this range. The backward radiation lobe is then observable.

In Chapter 3, the LHM is filled into a cylindrical wave guide. When a charged

133

particle passes through the axis of the cylinder, a surface plasmon can be excited, which enables a LHM to have one more mechanism for particles to lose energy that a RHM. Also with the ability to support a backward propagating wave in it, a LHM has the best mechanism for the particle to lose energy. If the LHM core is coated with metal, peaks can appear at certain frequencies when the guidance condition is satisfied. The radiation will be enhanced at these frequencies, and therefore the total radiated energy can be higher than in the unbounded LHM. It is possible to shoot a focused electron beam into the LHM waveguide, and to generate the backward radiation. However the possible noises induced by the electromagnetic fields used for control the electron beam, and the drifting effect of the electrons should be considered in reality. The existence of the surface wave can also be applied to compensate for the radiation decay due to the vacuum channel. At those frequencies, the surface plasmon can be excited at certain frequency and the field can be amplified in the LHM layer. At this frequency, the radiation will have a much higher amplitude than other frequencies when the wave enters into the third layer, in which the Čerenkov radiation condition is satisfied. These properties could be used to improve a Čerenkov detector or be used as a frequency selector.

In Chapter 5, a special new design is introduced specifically for Čerenkov radiation, for essentially TM wave incidence. The new design has a two dimensional isotropic negative permittivity, and a negative permeability in the normal direction. This design has one more negative dimension than other designs. Through the numerical simulations, we showed that the new design has a LH band between 6GHz to 7GHz. It has low loss which is an important advantage for applications. This design is the first generic design for TM wave incidence, and therefore it opens the possibility to realize a prism experiment for a LHM in the THz frequency range. Because it is a layered structure, there is no need to erect any rods or rings as required by other previous designs. The researchers can simply use the currently available techniques to build this design layer by layer. A lot more interesting properties and applications of a LHM can be explored with this new design. In order to verify that the new design can support a backward wave from the radiation, we designed an antenna array to

134

model the traveling line current, which is a single frequency component when the particle motion is decomposed into the frequency domain. With this antenna, we can easily select the frequency and adjust the radiation angle, which is actually realizable in the microwave frequency band. We then put the antenna array in between the two LHM slabs. The simulation results show that the phase front inside the LHM slab tilts toward to the x axis, which is consistent with our expectation. Furthermore, the LHM slabs are then replaced with LHM prisms. The purpose is to make the far field radiation point in the backward direction in the LH frequency band, and to point in the forward direction in the RH frequency band. Therefore, the effect of backward radiation can be detected at the far field. The simulation results confirm our design. These results can be a basis for future experiments.

Besides the topics of Čerenkov radiation, this thesis also investigated two phenomena related to the surface wave difference between RHM and LHM systems. In the application of the perfect lens, the pole of the transmission coefficient indicates the existence of a surface plasmon. This pole will actually limit the resolution of the LHM slab lens. As the mismatch decreases, the pole becomes larger, and therefore more evanescent components are amplified, and the resolution is increased. When the LHM is used as a planar waveguide, a unique guided mode can exist when the transverse wave vector is equal to 0. Normally, this is just a redundant solution and never corresponds to any guided mode. Only when the slab is an LHM, this mode can exist as a transition mode between anti-symmetric hyperbolic and anti-symmetric trigonometric modes.

In conclusion, this thesis has built the theoretical basis for Čerenkov radiation in LHM systems. More importantly, a new design is proposed and simulated, which can be used to verify the theory, and for many other practical applications.

Bibliography

[1] V. G. Vesalago. The electrodynamics of substances with simultaneously negative values of ϵ and μ. *Soviet Physics USPEKHI*, 10:509–514, January 1968.

[2] R. A. Shelby, D. R. Smith, and S. Schultz. Experimental verification of a negative index of refraction. *Science*, 292:77–79, April 2001.

[3] J.B. Pendry, A.J. Holden, D.J. Robbins, and W.J. Stewart. Magnetism from conductors and enhanced nonlinear phenomena. *IEEE Trans. on Microwave Theory and Tech.*, 47(11):2075–2084, November 1999.

[4] J. B. Pendry, A. J. Holden, W. J. Stewart, and I. Youngs. Extremely low frequency plasmons in metallic mesostructures. *Phys. Rev. Lett.*, 76(25):4773–4776, June 1996.

[5] C. Luo, M. Ibanescu, S. G. Johnson, and J. D. Joannopoulos. Cerenkov radiation in photonic crystals. *Science*, 299:368–371, 2003.

[6] J. Lu, T. M. Grzegorczyk, Y. Zhang, J. Pacheco, B.-I. Wu, J. A. Kong, and M. Chen. Cerenkov radiation in materials with negative permittivity and permeability. *Opt. Express.*, 11(7):723–735, 2003.

[7] J. Lu, T. M. Grzegorczyk, B.-I. Wu, J. Pacheco, M. Chen, and J. A. Kong. Effect of poles on subwavelength focusing by an lhm slab. *Microw. Opt. Technol. Lett.*, 45(1):49–53, 2005.

[8] J. Lu, B.-I. Wu, J. A. Kong, and M. Chen. Guided modes with a linearly varying transverse field inside a Left-Handed dielectric slab. *J. of Electromagn. Waves and Appl.*, 20(5):689–697, 2006.

[9] P. A. Čerenkov. Visible radiation produced by electrons moving in a medium with velocities exceeding that of light. *Phys. Rev.*, 52:378–379, 1937.

[10] I. M. Frank and I. G. Tamm. Coherent visible radiation of fast electrons passing through matter. *Compt. Rend. (Dokl.)*, 14(3):109–114, 1937.

[11] Jie Lu, T. M. Grzegorczyk, Y. Zhang, J. Pacheco Jr, B. I. Wu, and J. A. Kong. Čerenkov radiation in left handed material. In *Proceedings for Progress in Electromagnetics Research Symposium*, page 917, Cambridge, MA, July 2002.

[12] J. A. Kong. *Electromagnetic Wave Theory*. EMW, Cambridge, Massachusetts, 2000.

[13] J. V. Jelley. *Čerenkov Radiation and its Applications*. Pergamon Press, Inc., New York, 1958.

[14] M. H. Saffouri. Treatment of Čerenkov radiation from electric and magnetic charges in dispersive and dissipative media. *Nuovo Cimento*, 3D:589–622, 1984.

[15] B. M. Bolotovskii. Theory of cherenkov radiation. iii. *Sov. Phys. Usp.*, 4:781–811, 1962.

[16] I. V. Shadrivov, A. A. Sukhorukov, and Y. S. Kivshar. Guided modes in negative-refractive-index waveguides. *Phys. Rev. E*, 67:057602, 2003.

[17] W. Gai, P. Schoessow, B. Cole, R. Konecny, J. Norem, J. Rosenzweig, and J. Simpson. Experimental demonstration of wake-field effects in dielectric structures. *Phys. Rev. Lett.*, 61:2756–2758, 1988.

[18] J.B. Pendry. Negative refraction makes a perfect lens. *Phys. Rev. Lett.*, 85:3966–3969, 2000.

[19] D.R. Smith, D. Schurig, M. Rosenbluth, and S. Schultz. Limitations on sub-diffraction imaging with a negative refractive index slab. *Appl. Phys. Lett.*, 82:1506–1508, 2003.

[20] L. Shen and S. He. Studies of imaging characteristics for a slab of a lossy left-handed material. *Phys. Lett. A*, 309:298–305, 2003.

[21] J.A. Kong. Electromagnetic wave interaction with stratified negative isotropic media. *Progress in Electromagn. Res.*, 35:1–52, 2002.

[22] B.I. Wu, T.M. Grzegorczyk, Y. Zhang, and J.A. Kong. Guided modes with imaginary transverse wave number in a slab waveguide with negative permittivity and permeability. *J. Appl. Phys.*, 93:9386–9388, 2003.

[23] R. E. Collin. *Field Theory of Guided Waves*. John Wiley & Sons, Inc., New York, 1991.

[24] A. A. Oliner and T. Tamir. Backward waves on isotropic plasma slabs. *J. Appl. Phys.*, 33(1):231–233, 1962.

[25] E. N. Economou. Surface plasmons in thin films. *Phys. Rev.*, 182(2):539–554, 1969.

[26] K. L. Kliewer and R. Fuchs. Collective electronic motion in a metallic slab. *Phys. Rev.*, 153(2):498–512, 1967.

[27] R. H. Ritchie. Surface plasmons in solids. *Surf. Sci.*, 34(1):1–19, 1973.

[28] W. H. Weber and S. L. McCarthy. Anomalies in the surface plasmon resonance excitation at both surfaces of evaporated metal films. *Appl. Phys. Lett.*, 25(7):396–398, 1975.

[29] A. B. Buckman and C. Kuo. Coupled surface plasmons in structures with thin metallic layers. *J. Opt. Soc. Am.*, 69(2):343-7, 1979.

[30] H. Kitajima, K. Hieda, and Y. Suematsu. Use of a total absorption atr method to measure complex refractive indices of metal-foils. *J. Opt. Soc. Am.*, 70(12):1507–1513, 1980.

[31] J. J. Burke, G. I. Stegeman, and T. Tamir. Surface-polariton-like waves guided by thin, lossy metal films. *Phys. Rev. B*, 33(8):5186–5201, 1986.

[32] I. V. Lindell and S. Ilvonen. Waves in a slab of uniaxial bw medium. *J. Electromagn. Waves Appl.*, 16(3):303–318, 2002.

[33] Y. He, Z. Cao, , and Q. Shen. Guided optical modes in asymmetric left-handed waveguides. *Opt. Commun.*, 245:125–135, 2005.

[34] W. C. Chew. Sommerfeld integrals for left-handed materials. *Microw. Opt. Technol. Lett.*, 42(5):369–373, 2004.

[35] L. D. Landau and E. M. Lifshitz. *The Classical Theory of Fields*. JPergamon Press, Inc., New York, 1989.

[36] S. OBrien and J. B. Pendry. Magnetic activity at infrared frequencies in structured metallic photonic crystals. *J. Phys.: Condens. Matter*, 14(25):6383–6394, June 2002.

[37] C. R. Simovski and S. He. Frequency range and explicit expressions for negative permittivity and permeability for an isotropic medium formed by a lattice of perfectly conducting ω particles. *Phys. Lett. A*, 311:254–263, 2003.

[38] H. S. Chen, L. X. Ran, J. T. Huangfu, X. M. Zhang, K. S. Chen, T. M. Grzegorczyk, and J. A. Kong. Magnetic properties of s-shaped split-ring resonators. *Progress Electromag. Res.*, 51:231–247, 2005.

[39] R. Marques, F. Medina, and R. Rafii-El-Idrissi. Role of bianisotropy in negative permeability and left-handed metamaterials. *Phys. Rev. B*, 65:144440, 2002.

[40] T. M. Grzegorczyk, C. D. Moss, J. Lu, X. Chen, J. Pacheco Jr., and J. A. Kong. Properties of left-handed metamaterials: Transmission, backward phase, negative refraction, and focusing. *IEEE Trans. Microw. Theory Tech.*, 53(9):2956–2967, September 2005.